JOURNAL OF SYNCHROTRON RADIATION

ISSN 1600-5775

Quantitative characterization of the X-ray beam at the Australian Synchrotron Imaging and Medical Beamline (IMBL)

Andrew W. Stevenson,[a,b]* Jeffrey C. Crosbie,[c,d] Christopher J. Hall,[a] Daniel Häusermann,[a] Jayde Livingstone[a] and Jessica E. Lye[c,e]

[a]Australian Synchrotron, 800 Blackburn Road, Clayton, Victoria 3168, Australia, [b]CSIRO Manufacturing, Private Bag 10, Clayton South, Victoria 3169, Australia, [c]School of Science, RMIT University, GPO Box 2476, Melbourne, Victoria 3001, Australia, [d]William Buckland Radiotherapy Centre, Alfred Hospital, Melbourne, Victoria 3004, Australia, and [e]ARPANSA, 619 Lower Plenty Road, Yallambie, Victoria 3085, Australia. *Correspondence e-mail: andrew.stevenson@synchrotron.org.au

Received 18 May 2016
Accepted 4 October 2016

Edited by P. A. Pianetta, SLAC National Accelerator Laboratory, USA

We dedicate this paper to the memory of Adjunct Professor S. W. Wilkins, BSc (Melbourne), PhD (Melbourne), FAIP: an inspirational colleague, internationally respected research scientist, highly valued mentor and true friend, sadly missed. Steve passed away suddenly in Melbourne on Monday 25 March 2013 at age 67 years; he was just about to deliver the first in a series of eagerly awaited lectures on X-ray science to Physics Honours students at Monash University. It is of some comfort to know that, at the end, Steve was doing something which he was so passionate about; imparting some of his knowledge to the next generation of researchers. Steve was a great contributor to the International Union of Crystallography (IUCr) in so many ways, through his involvement with both the international crystallography and synchrotron communities. Too numerous to list here, we just mention one such contribution for each: Steve was a major organizer of and the driving force behind the extremely successful 2012 Bragg Centennial Symposium in Adelaide, celebrating 100 years of the Braggs' pioneering work in X-ray crystallography; the multi-purpose powder diffractometer (affectionately known as 'BigDiff'), conceived by Steve and constructed at CSIRO in Melbourne under his leadership, was installed in 1992 and operated at the Photon Factory synchrotron in Japan for approximately 20 years, as the centrepiece of the Australian National Beamline Facility (ANBF).

Keywords: ionization chambers; dosimetry; X-ray beam quality.

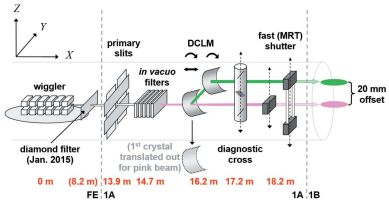

A critical early phase for any synchrotron beamline involves detailed testing, characterization and commissioning; this is especially true of a beamline as ambitious and complex as the Imaging & Medical Beamline (IMBL) at the Australian Synchrotron. IMBL staff and expert users have been performing precise experiments aimed at quantitative characterization of the primary polychromatic and monochromatic X-ray beams, with particular emphasis placed on the wiggler insertion devices (IDs), the primary-slit system and any *in vacuo* and *ex vacuo* filters. The findings from these studies will be described herein. These results will benefit IMBL and other users in the future, especially those for whom detailed knowledge of the X-ray beam spectrum (or 'quality') and flux density is important. This information is critical for radiotherapy and radiobiology users, who ultimately need to know (to better than 5%) what X-ray dose or dose rate is being delivered to their samples. Various correction factors associated with ionization-chamber (IC) dosimetry have been accounted for, *e.g.* ion recombination, electron-loss effects. A new and innovative approach has been developed in this regard, which can provide confirmation of key parameter values such as the magnetic field in the wiggler and the effective thickness of key filters. IMBL commenced operation in December 2008 with an Advanced Photon Source (APS) wiggler as the (interim) ID. A superconducting multi-pole wiggler was installed and operational in January 2013. Results are obtained for both of these IDs and useful comparisons are made. A comprehensive model of the IMBL has been developed, embodied in a new computer program named *spec.exe*, which has been validated against a variety of experimental measurements. Having demonstrated the reliability and robustness of the model, it is then possible to use it in a practical and predictive manner. It is hoped that *spec.exe* will prove to be a useful resource for synchrotron science in general, and for hard X-ray beamlines, whether they are based on bending magnets or insertion devices, in particular. In due course, it is planned to make *spec.exe* freely available to other synchrotron scientists.

1. Introduction

The Australian Synchrotron achieved 'first light' on 14 July 2006, with full ring current (200 mA) achieved in December 2006, and the first phase of operations commencing in April 2007. The Imaging and Medical beamline (IMBL) achieved first light on 1 December, 2008, with the first experiments commencing on 11 December 2008 (in hutch 1B). These were reported by Stevenson *et al.* (2010) and related to both qualitative and quantitative X-ray imaging/tomography studies with a (filtered) white (or 'pink') beam. A subsequent paper (Stevenson *et al.*, 2012) reported the first results of

quantitative tomography experiments conducted on the IMBL with monochromatic X-rays. This study included a comprehensive characterization of the point-spread function and detailed considerations of harmonic contamination and phase-contrast effects in X-ray imaging.

The experimental program at IMBL covers a wide range of applications (including industrial) in both materials and life sciences. Medical and biomedical areas are a particular strength, the beamline having been designed with a range of pre-clinical and clinical research programs envisaged. IMBL is well supported by adjacent animal-holding facilities (including PC2 certification), and has equipment including surgical microscopes, an anaesthesia delivery system and a ventilator for small animals, biohazard cabinet, incubators for cell-culture work, and a cell analyser with a variety of assays available.

Given the broad capabilities of IMBL in X-ray imaging, tomography and radiotherapy, including microbeam radiation therapy [MRT; *e.g.* Slatkin *et al.* (1992), Laissue *et al.* (1998, 2001), Bouchet *et al.* (2016)], key X-ray beam-related quantities to be considered include:

(i) Ring energy (GeV), ring current (mA), offset current (mA), ID field (T).

(ii) Spectral brightness (or brilliance) at the source [photons s^{-1} mm^{-2} $mrad^{-2}$ (0.1% bandwidth)$^{-1}$], flux density at the source [photons s^{-1} mm^{-2} (0.1% bandwidth)$^{-1}$], angular flux density [photons s^{-1} $mrad^{-2}$ (0.1% bandwidth)$^{-1}$], flux [photons s^{-1} (0.1% bandwidth)$^{-1}$], photon (or energy) fluence rate at the sample or detector (photons s^{-1} mm^{-2} or keV s^{-1} mm^{-2}), intensity (photons s^{-1} $mrad^{-2}$), integrated flux (photons s^{-1}).

(iii) (Spectrally) weighted-average X-ray energy (keV), X-ray energy for maximum flux (keV), FWHM of flux distribution (keV), power (W).

(iv) Half-value layers (HVLs) (mm), homogeneity factor (HF).

(v) (Absorbed-) dose rate (Gy s^{-1}), (absorbed) dose (Gy), peak-to-valley dose ratio (PVDR) and output factor[1] in the case of MRT, ionization-chamber (IC) current (μA), percentage depth dose (PDD).

(vi) Imaging signal, *e.g.* for a charge-coupled device (CCD) detector.

We focus on the polychromatic (white/pink) X-ray beam in this paper, but discussion of various aspects of monochromatic X-ray beams will also be included, because they arise quite naturally, *e.g.* considerations of harmonic contamination, and the effect of the pink beam incident on the first Si crystal of the double-crystal Laue monochromator (DCLM), including the inevitable 'heat bump'. Design considerations for such monochromators are provided by, for example, Suortti *et al.* (2000).

IMBL has six hutches, with 1A, 2A and 3A being the 'optics' or beam-conditioning hutches, and 1B, 2B and 3B being the experimental hutches. Hutch 1B has been used primarily for radiotherapy experiments, hutch 2B for rapid imaging/tomography and (increasingly) radiotherapy, and hutch 3B for imaging/tomography of large samples and where high resolution and an ability to utilize phase contrast are important. Hutches 1A to 2B are within the main experimental hall and hutches 3A and 3B are in a dedicated satellite building. Recent examples of applications which have benefitted from access to IMBL include tomography on ∼400 million-year-old fossils of Placoderms (prehistoric armoured fish, the first-known jawed vertebrates) (Trinajstic *et al.*, 2015) and the identification of genes and molecular pathways differentially regulated by synchrotron-based MRT compared with conventional broad-beam radiotherapy for cultured EMT6.5 mouse mammary tumour cells (Yang *et al.*, 2014).

2. Experimental set-up

Table 1 provides the disposition and details of the main beamline components. The white or pink beam is at a nominal height of 1.40 m (the monochromatic beam is usually at 1.42 m). The Australian Synchrotron is a third-generation source with a circumference of 216 m and is typically operated at the nominal 3 GeV and 200 mA, in 'top-up' mode[2], with 360 bunches of approximate length 25 ps (7 mm) [Dowd *et al.*, 2008; *cf.* SPring-8 bunch length of 13 ps (4 mm)][3], separated by 2 ns (0.6 m). Details of the physics design of the electron storage ring, which is based on a modified Chasman–Green-type (double-bend achromat; Chasman *et al.*, 1975) lattice with a periodicity of 14, are provided by Boldeman & Einfeld (2004). We will include the true ring (electron) energy in our considerations below. Panopoulos *et al.* (2011) and subsequent experimental studies (*e.g.* Wootton *et al.*, 2013) have used the technique of resonant spin depolarization to accurately determine the ring energy at the Australian Synchrotron. Variations of approximately 30 keV over an 8 h shift, and longer-term (several months) variations an order of magnitude larger were reported. Such variations are not significant in the context of the current study.

In 'top-up' mode the ring current, which is measured by a DC current transformer (DCCT) located in the diagnostic straight section of the storage ring, will typically vary between 200.0 and 200.6 mA. This 0.3% variation will be allowed for as necessary in the current study. The offset current, which is essentially a zero error, is insignificant in most cases; however, in the case of special low-current studies, this offset needs to be taken into account. The offset current can be measured at the beamline (see §4.4.2) but is not constant. Monitoring the offset current at 60 s intervals over the final 8 days of 2014,

[1] The output factor is defined as the ratio of the MRT peak dose and the corresponding broad-beam dose, and will in general be less than unity. Monte Carlo simulations are often used to provide output-factor values as a function of beam size and (water) depth.

[2] 'Top-up' mode operations commenced in May 2012 (van Garderen *et al.*, 2013).

[3] This bunch length is based on the Australian Synchrotron operating, as originally designed, with four single-cell, normal-conducting radio-frequency (RF) cavities. In fact, the facility has been operating successfully with just three of the RF cavities for a considerable time and, in this case, the bunch length is approximately 30 ps.

Table 1
Details of key IMBL components as of December 2014. FE = front-end, STL = short transfer line.

Component	Hutch	Distance (m)	Comments
Front-end mask	FE	7.5	6.6 mrad (H) × 0.98 mrad (V)
Front-end photon shutter	FE	8.2	6.0 mrad (H) × 0.83 mrad (V)
Mask	FE	10.3	5.1 mrad (H) × 0.33 mrad (V)
Main gate valve	FE	13.2	End of FE
In vacuo horizontal primary slits	1A	13.7	Water cooled; define horizontal dimension of primary beam
In vacuo vertical primary slits	1A	14.0	Water cooled; define vertical dimension of primary beam
In vacuo filter vessel	1A	14.7	Five paddles (at 14.39, 14.53, 14.67, 14.81 and 14.95 m); water cooled
1A (centre)	1A	15.9	1A is 6.6 m long (refers to beam direction as hutch is not rectangular)
DCLM	1A	16.2	Middle of vacuum tank; 1.00 mm thick bendable Si, 111, ∼17 to 120 keV
Diagnostic cross	1A	17.2	Diode can monitor scattering from wires/foils inserted in beam path
Beamline photon shutter	1A	17.6	Used in conjunction with safety shutter (also in 1A post-MRT shutter)
MRT shutter	1A	18.2	*In vacuo* two-blade shutter for ≥30 ms exposures
Be window (polished)†‡	1B	20.4	0.35 mm-thick; He-flushed (74 mm path); 38 µm-thick Al foil
1B (centre)	1B	22.3	1B is 6 m long (refers to beam direction as hutch is not rectangular)
2A (centre)	2A	28.6	2A is 6.3 m long
Be window (polished)§	2A	30.7	0.35 mm-thick; He-flushed (81 mm path); 38 µm-thick Al foil
Experimental table§	2A	31.1	Slits, fast shutter, high-voltage IC; 0.6 m air path between Be windows
Be window (polished)§	2A	31.5	0.35 mm-thick; He-flushed (81 mm path); 38 µm-thick Al foil
Be window (polished)‡¶	2B	32.8	0.35 mm-thick; He-flushed (74 mm path); 38 µm-thick Al foil
2B (centre)	2B	35.9	2B is 8.1 m long
Mask	STL	40.3	3.8 mrad × 1.4 mrad
3A (centre)	3A	129.5	3A is 10 m long
Be window(polished)††	3B	135.8	2.0 mm-thick; He-flushed (43 mm path); 38 µm-thick Al foil
3B (centre)	3B	140.3	3B is 10 m long

† Only relevant for 1B operation. ‡ This window is shared between 1B and 2B. § Only relevant for 2B or 3B operation. ¶ Only relevant for 2B operation. †† Only relevant for 3B operation.

when the synchrotron was in a shutdown period, yielded an average current reading of 32 (7) µA (the minimum reading being 10.9 µA and the maximum reading 55.4 µA). Repeating this determination for another 8-day shutdown period in May 2014 yielded corresponding values of 11 (7) µA, −9.2 µA and 45.6 µA, respectively. Such values are negligible when compared with 200 mA, but not if compared with, say, 1 mA.

The original (interim) ID was an Advanced Photon Source (APS) type-A permanent-magnet wiggler (No. 24), with 28 × 8.5 cm periods (total length 2.38 m). The gap was typically selected within the range from 25 to 15 mm, corresponding to fields between 0.838 and 1.40 T, deflection parameter K between 6.65 and 11.1, critical energy E_c between 5.0 and 8.4 keV, and power between 1.9 and 5.3 kW (see Lai *et al.*, 1993). In January 2013 the APS wiggler was replaced by a superconducting multi-pole wiggler (SCMPW), supplied by Budker Institute of Nuclear Physics (Novosibirsk, Russia). The SCMPW has (effectively) 30 × 5.2 cm periods (total length 1.56 m), there actually being 59 pole pairs at full-field, plus single pole pairs at 3/4-field and 1/4-field at each end. The maximum possible field is 4.20 T (K = 20.4, E_c = 25.1 keV and power 31.3 kW) but 3.00 T (K = 14.6, E_c = 18.0 keV and power 16.0 kW) is currently both the standard and maximum field. A conservative estimate of the error in the wiggler field is ±0.05 T. The RMS electron beam size in the straight sections at the Australian Synchrotron is 320 µm horizontally and 16 µm vertically[4] (1% coupling); with 0.1 m distributed dispersion.[5] These values correspond to Gaussian FWHM of 754 µm and 38 µm, respectively. The electron-beam deviation caused by the field of the ID is small in comparison with the electron-beam size and so it is the latter which dictates the X-ray source size (see also Stevenson *et al.*, 2010).

Fig. 1 provides a schematic diagram of key IMBL components. In the case of the DCLM[6] in hutch 1A (Fig. 1*a*), the most critical adjustments are indicated: the Bragg-rotation angle for each crystal (about Y) and the translation along the beam direction (X) of the first crystal relative to the (fixed) second crystal. Each crystal also has a tilt (roll), a vertical translation (along Z), and in-board and out-board bending (about Y, when the tilt is zero) adjustments [crystals are shown as being convex as viewed from the source in Fig. 1(*a*), but can also be flat or concave]. The vertical translations, in particular for the first crystal, are used to remove these optical elements from the path of the incident beam when using a pink/polychromatic X-ray beam.

The fast (MRT) shutter shown in Fig. 1(*a*) comprises two independent blades which can be translated along Z (see also Renier *et al.*, 2002); the beamline photon shutter (immediately upstream) and safety shutter (immediately downstream) are not shown in Fig. 1. These two blades are shown in their 'rest' positions, ready to deliver a radiotherapy exposure (where the first or upstream blade is raised in order to allow the pink

[4] *cf.* SPring-8: 316 µm horizontally/5 µm vertically for a standard straight section, 333 µm horizontally/7 µm vertically for a long straight section (both for 0.2% coupling); 0.146 m and 0.153 m horizontal dispersion, respectively.

[5] Experimental results (obtained during a 'machine-studies' period) and corresponding theoretical calculations, for 0.1 and 1% coupling, and 0.1, 0.2 and 0.24 m distributed dispersion, showed that the results obtained in this paper are not, in general, sensitive to such changes in accelerator configuration.

[6] Supplied by Instrument Design Technology (IDT) (Widnes, UK).

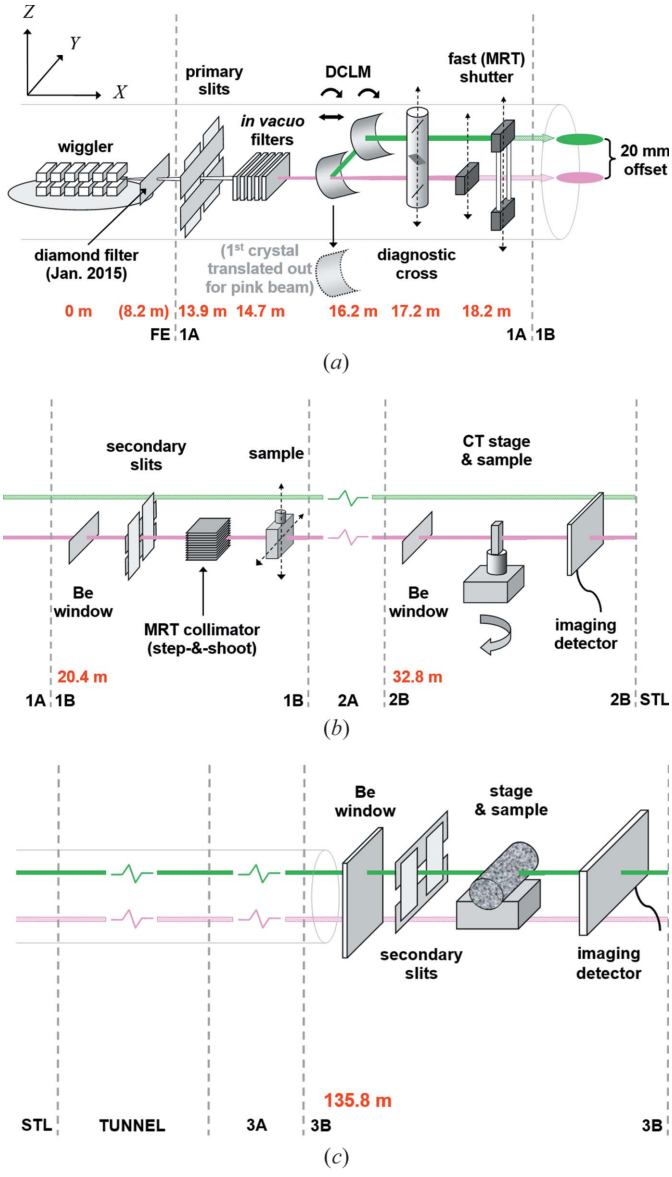

Figure 1
Schematic diagram with some of the key IMBL components: (*a*) the front-end (FE) to hutch 1B; (*b*) hutch 1B to hutch 2B; (*c*) the short transfer line (STL) to hutch 3B. Both pink-beam and monochromatic-beam (coloured green) scenarios are displayed. There are different (typical) experimental set-ups in hutches 1B, 2B and 3B: 'step-and-shoot' mode radiotherapy, (pink-beam) tomography, and fast (monochromatic beam) imaging of large samples, respectively. The large horizontal cylinders indicate where the X-ray beam is always *in vacuo*. The beamline photon and safety shutters, located immediately upstream and downstream of the fast (MRT) shutter in hutch 1A, respectively, have not been shown here. The distances of key components from the source are shown near the bottom in red. Further details are provided in the text.

beam through, followed by the second or downstream blade being raised in order to block the pink beam again). The beamline photon and safety shutters also move in a coordinated manner so as to avoid hindering the radiotherapy exposure and yet block the beam as needed, ensuring also that the fast shutter blades are not subjected to the beam for extended periods. This procedure also ensures that any vertical gradient introduced across the exposure field by the traverse of the first blade is compensated for by the corresponding traverse of the second blade. The inclusion of the upper component of the second blade means that, in principle, similar shuttering of the monochromatic beam (coloured green) could be achieved (but this has not been implemented at IMBL). In cases where a pink beam is being used without operating the fast shutter, the first blade is simply raised and pinned in place. Conversely, use of the monochromatic beam necessitates that the second blade is raised and pinned instead. The roles and operation of the beamline photon and safety shutters is also changed in both of these instances. If the FE shutter (not shown in Fig. 1) is opened and the beamline shutters are closed, the upstream X-ray optical components [primary slits, *in vacuo* filters, and (in monochromatic mode) the DCLM] will remain in the beam and so are better able to equilibrate/stabilize. Any changes to the *in vacuo* filter configuration do, however, require the FE shutter to be closed first. The diamond filter introduced more recently during an upgrade of the FE (see §4.4.2) is at 8.2 m from the source, with the FE shutter having been moved downstream to 9.8 m (compared with 8.2 m in Table 1); thus the diamond filter is not subjected to any 'thermal cycling'.

Figs. 1(*b*) and 1(*c*) show typical examples of equipment configurations which are used in the experimental hutches 1B, 2B and 3B: 'step-and-shoot' mode radiotherapy, pink-beam tomography and (fast) monochromatic beam imaging of large samples, respectively. In hutch 1B the sample, such as a flask containing tumour cells, is irradiated by a set of horizontal microbeams formed by the MRT collimator. In order to be able to irradiate a large cross-sectional field with this spatially fractionated beam, the sample is mounted on a *Y*–*Z* stage and a two-dimensional raster scan performed in coordination with the operation of the fast (MRT) shutter in hutch 1A. Precise steps in *Y* need to be chosen so that neighbouring columns of horizontal microbeams intercept seamlessly; and in *Z* so that the (inter-) spacing for neighbouring rows of microbeam sets matches the (intra-) spacing of individual microbeams within a set. In hutch 2B the sample can be rotated about *Z* with a suitable imaging detector, in order to collect tomography data. The distance, along *X*, between sample and detector can be varied to provide, if appropriate, contributions due to X-ray phase-contrast effects. Finally, in hutch 3B, the much larger X-ray beam affords us with the opportunity to image quite large samples and/or to better utilize phase-contrast effects, given the improved spatial-coherence properties of the X-ray beam (this is particularly the case in the horizontal direction, where the relatively large source size can be an issue nearer to the source). The flux in hutch 3B, even for the monochromatic beam case, is also quite sufficient to enable fast imaging of certain dynamic processes occurring in some samples.

3. Calculations

The calculations in this paper were performed using software independently developed in-house. The program is named *spec.exe*[7] and was coded in Fortran. The capabilities of

[7] *spec.exe* has been written by one of us (AWS) and includes the option of being able to read in *SPECTRA*-generated data files.

spec.exe will be detailed throughout the paper. Various results have been compared with those from the well known programs *SPECTRA* (Tanaka & Kitamura, 2001, 2007; currently version 9.0; see also Tanaka, 2014) and *XOP* (Sánchez del Río & Dejus, 2011; currently version 2.4), and another in-house program *Dose4IMBL* (Crosbie *et al.*, 2013), with excellent agreement obtained. Whilst *spec.exe* has been written in accordance with the specific requirements of IMBL, it has also been applied very successfully to, for example, an Australian Synchrotron bending-magnet beamline and ID beamlines at other facilities [such as ID17 at the European Synchrotron Radiation Facility (ESRF); see Crosbie *et al.*, 2015]. An ability to reliably calculate synchrotron spectra, and derived quantities, is very important because the enormous fluxes involved at beamlines such as IMBL make direct and accurate measurements extremely difficult (see, for example, Honkimäki & Suortti, 1992).

3.1. Angular flux density at a point

Fig. 2 shows the results of calculations of angular flux density as a function of X-ray energy for a standard Australian Synchrotron bending magnet (1.30 T)[8] and both IMBL IDs, each at two fields. The calculations were performed for a single point in space; in this case, on the optic axis. The formulae used are those given in §2.1 of the *X-Ray Data Booklet* (Kim, 2001; see also Kim, 1989), for a bending magnet (BM) or wiggler source. The fundamental formulae involve modified Bessel functions of the second kind ($K_{1/3}$ and $K_{2/3}$; we have developed accurate tabulations of these functions for values of the argument from 0.01 to 100 in steps of 0.01; interpolated values of the Bessel functions are then derived as required and the well established limit-behaviour formulae are used for argument values less than 0.01 and greater than 100). There is also an option in *spec.exe* to incorporate (vertical) emittance effects (associated with the angular divergence of the electron beam). In this case it is necessary to evaluate an integral of the Bessel function $K_{5/3}$ from a variable (positive) lower limit to ∞. We have developed an accurate tabulation of this integral for values of the lower limit from 0.01 to 50 in steps of 0.01. Given that this variable (lower limit for integration) is the ratio of the X-ray energy E and E_c in this case, we do not need to consider values less than 0.01; values greater than 50 are, however, possible and the integral of the associated limit-behaviour formula for $K_{5/3}$ yields a complementary error function, which is easily evaluated by using the first two terms of a series expansion. Fundamental parameter values needed for Australian Synchrotron IDs and BMs are taken from LeBlanc *et al.* (2004). A direct comparison with results obtained using *SPECTRA*, which we are using as the 'gold standard', is given below. The curve for the SCMPW at 1.40 T (not shown in Fig. 2) is quite similar to that for the APS wiggler at the same field.

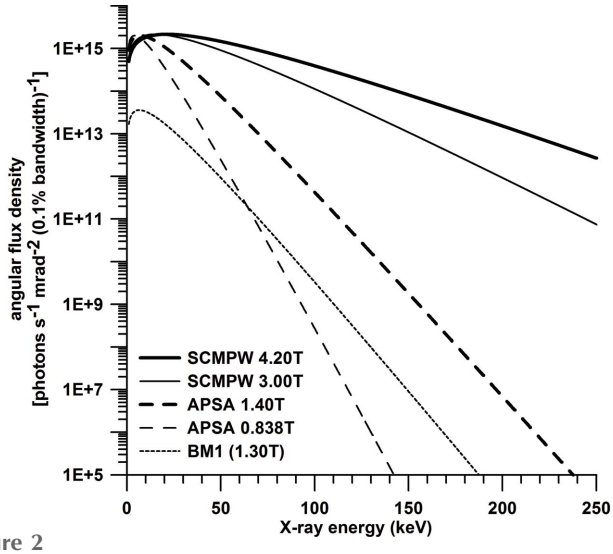

Figure 2
Calculations (*spec.exe*) of angular flux density (on-axis) as a function of X-ray energy for a standard Australian Synchrotron bending magnet (BM1), the APS type-A wiggler at two fields, and the SCMPW at two fields. The ring energy was 3.032 GeV, the ring current 200 mA, and the distance from the source 22.3 m (however, this last value is essentially irrelevant for these *on-axis* calculations). Normal operating conditions of 0.1 m dispersion in straight sections and 1% emittance coupling are assumed. The calculations were performed from 1 to 1000 keV in steps of 0.1 keV; the results are only presented up to 250 keV for convenience.

It is also possible to calculate values of spectral brightness (or brilliance) using *spec.exe*. This is achieved by first calculating the angular-flux-density values, and then dividing these by the corresponding calculated (energy-dependent) X-ray source areas. The latter are calculated as described by Tanaka & Kitamura (2004), based on Gaussian distribution functions. A more rigorous treatment, using the Wigner function (Wigner, 1932), is detailed by Tanaka (2014).

The benefits of operating the SCMPW at higher fields for X-ray imaging/tomography of dense/thick samples and for radiotherapy are quite apparent, given the greatly increased angular flux density at higher X-ray energies. In the case of radiotherapy, having higher dose rates at large distances from the source (hutch 2B and even 3B, rather than 1B) is attractive due to the increased beam size attainable. We will return to this point later as beam size and uniformity (in the presence of energy-dependent 'roll-off' effects) are important for both imaging/tomography and radiotherapy.

The ability to operate the SCMPW at lower fields is also important because it provides greater flexibility for imaging/tomography with the DCLM at lower energies in cases where harmonic contamination might otherwise be an issue. 'Detuning' the DCLM to reduce harmonic contamination is not as straightforward as for the case of monochromators operating, over smaller energy ranges, with thick crystals and Bragg geometry. Whilst the first Si crystal of the DCLM is specially cooled (both water and InGa) so as to withstand the high power and power density associated with the incident

[8] These calculations were performed for the first dipole in a cell (BM1) rather than the second (BM2); the angles of the source point into the magnet are 7.00 and 6.00°, respectively, and some of the fundamental parameters involved have different values in the two cases. For example, the Twiss parameter α_{vert}, associated with the phase-space ellipse describing emittance, has values of −3.0924 and 3.1658 rad for BM1 and BM2, respectively, *i.e.* there is a change from a diverging to a converging electron beam between the two dipoles. In a practical sense, however, there is essentially no difference between results of angular-flux-density calculations for BM1 and BM2.

Table 2
The average value of the percentage-error (Δ) when comparing, point by point, angular-flux-density data calculated using *spec.exe versus SPECTRA*.

The two cases of using *spec.exe* with and without inclusion of emittance effects are considered, and results for three X-ray energy ranges are given. The *SPECTRA* (version 9.0) calculations were performed with an 'accuracy level' of 5 (but certain calculations were also done at higher levels and no significant differences were found). This accuracy level relates to the numerical accuracy used for operations such as numerical integration, summations of infinite series, Fourier transforms, and so on. In the case of the BM1 *SPECTRA* calculations, values (based on measurements performed by accelerator physicists and operators) of 1.65 and 0.21 m were specified for the nominal and fringe field lengths, respectively (alternative values were also tested and, again, no significant differences were found). The last column contains Δ_{ave} values with allowance made for certain filters and a threshold for the angular flux density (see text for further details).

	Δ_{ave} (%)						
	spec.exe (no emittance) − *SPECTRA*			*spec.exe* (+ emittance) − *SPECTRA*			
	≤100 keV	≤250 keV	≤500 keV	≤100 keV	≤250 keV	≤500 keV	Filters and >0.001%
BM1 (1.30 T)	2.0	5.1	9.7	0.98	2.5	4.7	1.5
APSA 0.838 T	2.5	6.2	12	0.49	1.3	2.5	0.52
APSA 1.40 T	1.3	3.3	6.4	0.087	0.30	0.58	0.16
SCMPW 3.00 T	0.53	1.4	2.9	0.013	0.068	0.18	0.082
SCMPW 4.20 T	0.38	0.98	2.0	0.019	0.023	0.073	0.043

pink X-ray beam, this crystal does exhibit distortions and these can be reduced by going to lower ID fields. In the case of radiotherapy, lowering the wiggler field provides another option when performing certain low-dose studies, for example certain investigations of bystander and abscopal effects (see, for example, Lobachevsky *et al.*, 2015). This approach, and/or the use of added filtration, does of course result in a concomitant change in beam 'quality' (unfortunately, practical neutral-density filters do not exist for this part of the electromagnetic spectrum).[9] Operating at lower wiggler field can, for example, facilitate low-dose irradiations without excessive 'hardening' of the X-ray beam (see §3.3), which is important in some cases.

Table 2 provides average values of the percentage-error obtained when comparing, point by point, angular-flux-density data calculated using *spec.exe versus SPECTRA*. If we take the absolute value of the percentage-errors prior to averaging, the results are essentially unchanged since the *spec.exe* values are almost always greater than the *SPECTRA* values. All of the *SPECTRA* calculations include a rigorous treatment of emittance effects, and the values calculated with *spec.exe* are clearly in better agreement when these effects are also incorporated, albeit approximately. A number of trends can be seen in the results presented in Table 2. For example, the agreement is generally worse with increasing X-ray energy, and the (relative) improvement attributable to the allowance for emittance effects in *spec.exe* is greater as we go down the table (increase the magnetic field of the ID for instance). In order to provide Δ_{ave} values of more practical significance, the last column of Table 2 contains values where allowance has been made for certain filters [0.45 mm graphene, 14 mm of high-density (1.74 g cm^{-3}) graphite, 1.4 mm Al, and 0.35 mm Be] and a lower threshold of 0.001% has been applied to the resulting angular-flux-density values. Filtration of the X-ray beam will be discussed at length in §3.3.

3.2. Angular flux density in two dimensions

Angular flux density can also be calculated in (one or) two dimensions using *spec.exe*. We are, of course, dealing with the situation where the plane of the orbit of the relativistic electron beam is horizontal and the applied magnetic field direction is vertical. Along the horizontal direction through the centre of the X-ray beam (and perpendicular to the propagation direction) there will be no π polarization (electric vector vertical) component, only a σ (electric vector horizontal) component. The contributions associated with the different polarization components can be calculated separately if desired. The intensity values (photons s^{-1} mrad^{-2}) are obtained by integrating over a specified X-ray energy range, and can easily be plotted as, for example, a contour map or grey-scale plot. Further integration over the spatial dimensions will yield the integrated flux (photons s^{-1}). Component distributions of angular flux density for particular X-ray energies can also be saved. In Fig. 3, a particular contour level, 25 and 75% of the maximum values for (*a*) and (*b*), respectively, is shown for a number of such component distributions, 5, 10, 15, 20, 30, 50, 100, 200 and 500 keV. The case considered is that of the SCMPW operating at 3.00 T from Fig. 2. The step sizes used for the calculations were 0.1 and 0.01 mm in the horizontal and vertical directions, respectively, and it is important to note that the horizontal and vertical scales are quite different. A new front-end (FE) mask, 3.8 mrad (H) × 0.3 mrad (V), has recently (January 2015) been installed at IMBL and is represented by the grey rectangle when projected to 22.3 m from the source. The angular-flux-density value at the centre of each two-dimensional map, at each X-ray energy, can be obtained from Fig. 2.

In general the contours enclose smaller and smaller areas as the X-ray energy increases, *i.e.* energy-dependent 'roll-off' effects are visible both horizontally and vertically. This means that the spectrum or beam quality has a spatial dependence.

[9] We refer here to cases where the desired dose to the sample is so low that, at normal IMBL dose rates, the necessary shutter speed for conventional 'step-and-shoot' radiotherapy (or, in the case of 'dynamic' radiotherapy, the motor scan speed) is unachievably fast. Lowering the ring current is of course a most attractive option under these circumstances since the dose rate can be significantly reduced with no associated change in beam quality. However, routine operation at low ring currents is clearly not practicable. Increasing the distance from the source might be a viable alternative for the future, given the advent of hutch 3B.

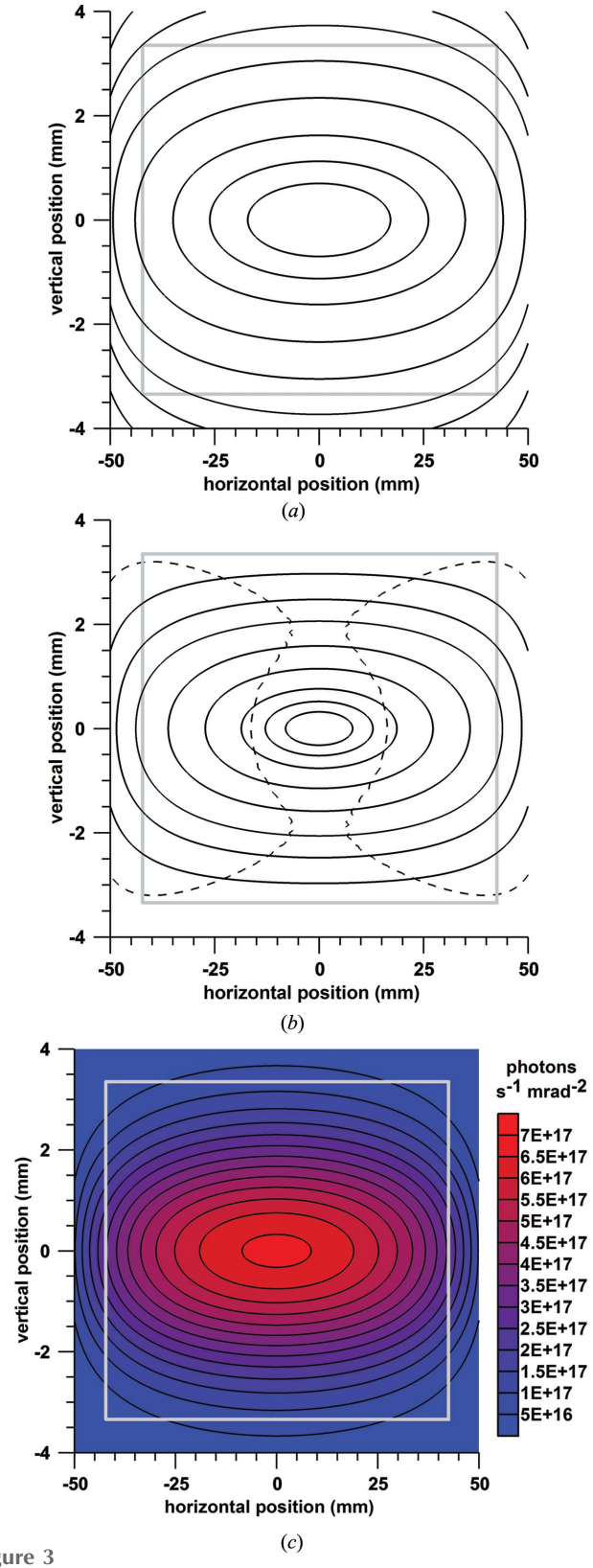

Figure 3
(*a*) 25% and (*b*) 75% contour levels for 5, 10, 15, 20, 30, 50, 100, 200 and 500 keV component distributions of angular flux density for the SCMPW 3.00 T case from Fig. 2. (*c*) Intensity distribution for the SCMPW 3.00 T case from Fig. 2. The filters referred to regarding the last column of Table 2 have also been included here. Note that the horizontal and vertical scales are quite different. The grey rectangles represent 3.8 mrad (H) × 0.3 mrad (V) at 22.3 m from the source. See text for further details.

The 25% contour for the 5 keV component is outside the plotted region in Fig. 3(*a*). In Fig. 3(*b*) the 75% contour for the 5 keV component is unusual and is shown as a dashed line, the central (on-axis) value being (see Fig. 2) 1.55×10^{15} photons s^{-1} $mrad^{-2}$ (0.1% bandwidth)$^{-1}$ whereas the lobes to the left and right encompass the maximum value of 2.12×10^{15} photons s^{-1} $mrad^{-2}$ (0.1% bandwidth)$^{-1}$. In the case of quite low X-ray energies, a higher angular flux density can be expected when the magnetic field is relatively weaker. The side lobes for 5 keV correspond to photons emitted by electrons passing through a position where the magnetic field is weaker.

Fig. 3(*c*) shows the two-dimensional intensity distribution for the SCMPW 3.00 T case from Fig. 2. The filters referred to in respect of the last column of Table 2 have also been included here (see §3.1). The grey rectangle again represents 3.8 mrad (H) × 0.3 mrad (V) at 22.3 m from the source. The component distributions were calculated for X-ray energies from 1 to 999 keV in steps of 2 keV and then combined. Integration of this intensity distribution over the spatial dimensions yields an integrated-flux value of 3.90×10^{17} photons s^{-1}.

3.3. Filtration

Filtration of the synchrotron X-ray beam is a key consideration and can occur as a result of the presence of vacuum windows, gas paths (including air), *in vacuo* and *ex vacuo* filters, optical elements (such as the first Si crystal of the DCLM) and any samples. The beamline vacuum is typically 5×10^{-6} Pa (5×10^{-8} mbar) or better (and better than 3×10^{-6} Pa in the, almost 100 m-long, transfer line between hutches 2B and 3B). Our main focus in this paper is on white/pink X-ray beams; however, understanding the role of filtration is important when using monochromatic X-ray beams too.

Two simple examples may help to illustrate this point. The DCLM was aligned and optimized to deliver a 30 keV X-ray beam and the downstream flux, as inferred from IC current measurements, was deemed to be too large for a particular experiment. The simplistic approach of adding an additional *in vacuo* Al filter (upstream of the DCLM) resulted in an *increase* of the IC current. Since the conditions were such that the IC was operating reliably and well within its capabilities, this result might at first seem incongruous. However, further investigation revealed that the DCLM first crystal had been operating with a very significant heat bump as a result of the excessive power loading from the incident X-ray beam. The inclusion of the extra Al filter reduced the heat bump, improved the operation and efficiency of the DCLM, and thereby increased the IC current. In a similar experimental set-up an iodine sample was being used to calibrate the X-ray energy from the DCLM. The X-ray energy was being changed in small steps through the iodine *K*-absorption-edge energy (33.17 keV). However, the ratio of IC currents measured before and after the sample showed only a monotonic increase with X-ray energy, casting doubt on the accuracy of the DCLM energy calibration. It transpired that the use of

excessive *in vacuo* filtration, in the form of both Cu and Mo foils, resulted in an X-ray beam downstream of the DCLM composed almost entirely of the λ/3 harmonic (99.51 keV), rendering the iodine *K*-edge essentially invisible. This example serves as a timely reminder that using an ID, especially the SCMPW at high magnetic field, yields significant (and easily measured) flux levels at quite high X-ray energies, compared with (say) a standard BM (see Fig. 2). Indeed, the relatively small fundamental (λ) component in the beam just described was rivalled in terms of flux by even higher-order harmonics like λ/4 (132.68 keV). We will return to the subject of harmonics in §4.

The program *spec.exe* is able to include the effect of a variety of filter materials, both elemental, such as He, Be, C, Al, Si, Cu, Mo, W, Au, Pb, and compound, such as air, water, Kapton® (polyimide), Perspex (PMMA), SiC. In certain cases, the density of the material can be specified or selected, *e.g.* for C there is 'flexible' graphite (1.0 g cm^{-3}), glassy carbon (Sigradur-K®) (1.54 g cm^{-3}), high-density (HD) graphite (1.74 g cm^{-3}), graphene (2.0 g cm^{-3}), highly oriented pyrolitic graphite (HOPG) (2.26 g cm^{-3}) and diamond (3.513 g cm^{-3}). The composition and density of air at standard conditions was taken from ICRU (1989) and allowance has been included for specifying the ambient temperature and pressure. Some of the IMBL *in vacuo* filter paddles are arranged so that filters are at an angle (*e.g.* 45°) to the beam and so it is necessary to calculate the 'effective' thickness of the material. Other filter materials can be incorporated into *spec.exe* in a straightforward manner, *e.g.* allowance for the effect of a Kr gas filter, with variable pressure, was recently included for calculations relating to the ESRF ID17 beamline; see Crosbie *et al.* (2015).

In the context of the comprehensive IMBL dosimetry research program, water is an important filtration material to be considered. Clinical reference-dosimetry protocols for kilovoltage X-ray beams invariably involve absorbed dose to water (see, for example, Ma *et al.*, 2001). Such work preferably utilizes liquid water but 'Solid Water™', such as Gammex 457, also has a role to play. This material is able to mimic the scattering and attenuation characteristics of liquid water over a wide range of X-ray energies. We have studied Solid Water™ with both pink and monochromatic X-ray beams. For example, with the latter we have collected transmission data (to be published elsewhere) for Solid-Water™ thicknesses from 2 to 140 mm, for X-ray energies of 33.17, 67.42 and 88.00 keV (*K*-edges of I, Ta and Pb, respectively), confirming its good liquid-water equivalence (see also Hill *et al.*, 2005).

The preferred tabulations for values of linear attenuation coefficient[10] used by *spec.exe* extend from 1 to 1000 keV in steps of 0.1 keV and have been derived by logarithmic interpolation of mass-attenuation-coefficient values from the NIST database; see Hubbell & Seltzer (1995)[11]. However, it is also possible to use tabulations based on data from McMaster *et al.* (1970) or from Zschornack (2007), but over a reduced X-ray energy range. Comprehensive reviews of the field have been provided by Hubbell (1999, 2006).

Table 3
Details of *in vacuo* filter sets considered in the present case and used at IMBL.

Note that F6 also involves *ex vacuo* Cu.

In vacuo filter set	Details
F0	No filters
F1	0.45 mm graphene + $15\sqrt{2}$ mm HD graphite
F2	0.45 mm graphene + $15\sqrt{2}$ mm HD graphite + $2\sqrt{2}$ mm Al
F3	0.45 mm graphene + $15\sqrt{2}$ mm HD graphite + $\sqrt{2}$ mm Cu + $2\sqrt{2}$ mm Al
F4	0.45 mm graphene + $15\sqrt{2}$ mm HD graphite + $2\sqrt{2}$ mm Cu
F5	0.45 mm graphene + $15\sqrt{2}$ mm HD graphite + $2\sqrt{2}$ mm Al + $2\sqrt{2}$ mm Mo
F6	0.45 mm graphene + $15\sqrt{2}$ mm HD graphite + $2\sqrt{2}$ mm Al + $2\sqrt{2}$ mm Mo + 4.65 mm Cu *ex vacuo*

Table 3 provides details of different filter combinations of interest in the present case and actually used at IMBL, a caveat being that 'F0' is only used in special cases when operating at very low ring currents. Also, there can be some restrictions based on the size of the desired X-ray beam. Occurrences of '$\sqrt{2}$' in the (effective) *in vacuo* filter thicknesses arise from certain filter paddles being at 45° to the X-ray beam (see above). Fig. 4 and Table 4 contain calculated results for such combinations of filters. We have considered the SCMPW 3.00 T case from Fig. 2, with a 1 mm × 1 mm X-ray beam at 22.3 m from the source, and at three locations (in some instances); on-axis, 1 mrad off-axis horizontally and 0.1 mrad off-axis vertically. Fig. 4 shows the results for flux as a function of X-ray energy and Table 4 provides values of various key parameters. The X-ray energy at which the maximum flux occurs and the weighted-average energy clearly show the variation of beam quality ('hardening' of the beam) with increasing levels of filtration. The softening of the beam for off-axis positions is also apparent from the extra results presented for F0 and F6, *i.e.* the roll-off is more pronounced for higher X-ray energies.

A more conventional means of describing and quantifying X-ray beam quality, especially in the medical context, is in terms of HVL, usually for either Al or Cu (see, for example, Trout *et al.*, 1960; Klevenhagen *et al.*, 1996; Ma *et al.*, 2001; Crosbie *et al.*, 2008, 2013). It is important to note that we are specifying HVLs in terms of integrated flux here since they are also specified in terms of absorbed dose or even IC current and the results will be different in general. Table 5 provides such HVL data, as modelled by *spec.exe*, for the cases being considered here. The homogeneity factor (HF) is the ratio of the first and second HVLs, where we adopt the definition of second HVL as being the filter thickness required to reduce the integrated flux from 50% to 25%. HF provides a convenient measure of the degree of polychromaticity of the X-ray beam (HF is always ≤ 1, with HF = 1 in the monochromatic case; HF < 1 in the polychromatic case is a manifestation of

[10] We will follow the terminology/nomenclature provided by ICRU (1980) for absorption/attenuation-related quantities.
[11] This also applies to values of mass (/linear) energy-absorption coefficients, introduced in §3.4. In this case it is also possible to use values (for 10 to 1000 keV) derived by logarithmic interpolation from data given by Cember (1983).

Table 4
Values of key parameters describing the flux curves in Fig. 4.

Since the flux values have been calculated for a 1 mm × 1 mm X-ray beam, the last column could also be termed photon fluence rate at the detector (photons s^{-1} mm^{-2}). *In vacuo* filter sets F1 and F3 are not considered until later in the paper but their results are included here for completeness. F6 also involves *ex vacuo* filtration.

In vacuo filter set	Beam position (mrad)	Maximum flux [photons s^{-1} (0.1% bandwidth)$^{-1}$]	Energy for maximum flux (keV)	FWHM (keV)	Weighted-average energy (keV)	Integrated flux (photons s^{-1})
F0	(0, 0)	3.39×10^{12}	22.1	38.3	29.7	5.01×10^{15}
F0	(1.5, 0)	3.07×10^{12}	20.0	30.3	25.9	4.12×10^{15}
F0	(0, 0.1)	2.38×10^{12}	18.5	25.3	23.4	2.96×10^{15}
F1	*(0, 0)*	*1.18×10^{12}*	*30.9*	*40.8*	*40.2*	*1.35×10^{15}*
F2	(0, 0)	7.04×10^{11}	40.0	42.2	49.0	6.88×10^{14}
F3	*(0, 0)*	*9.18×10^{10}*	*75.7*	*51.3*	*82.4*	*6.34×10^{13}*
F4	(0, 0)	4.19×10^{10}	86.8	53.5	94.4	2.64×10^{13}
F5	(0, 0)	5.50×10^{9}	117	62.7	124	3.03×10^{12}
F6	(0, 0)	1.49×10^{9}	131	66.2	137	7.85×10^{11}
F6	(1.5, 0)	3.02×10^{8}	121	57.2	126	1.46×10^{11}
F6	(0, 0.1)	6.91×10^{7}	115	52.2	121	3.20×10^{10}

'beam hardening'). These results clearly reinforce the trends observed in Table 4 and Fig. 4.

We have already made mention of the fact that the filtration of the X-ray beam at IMBL is also extremely important from the point of view of preventing damage to beamline optical components as a result of excessive heat loads. *spec.exe* can also calculate the power (W) or power density (W mm^{-2}) in the X-ray beam, the latter as a two-dimensional distribution if needed. Such calculations performed before and after a particular component (*e.g.* crystal, filter or window) can provide valuable results relating to absorbed power or power density. These results can also provide input data for finite-element calculations for example. By way of example, the calculated absorbed power density at the centre of the 0.35 mm Be window (beam) located at 20.4 m from the source in hutch 1B (see Table 1 and Fig. 1*b*) is 2.14 W mm^{-2}, if no *in vacuo* filters are used (F0 filter set).[12] This is not actually the maximum absorbed power density, which increases somewhat to either side (horizontally); see the discussion of the 5 keV contour in Fig. 3(*b*). The absorbed power for a 3 mrad (H) × 0.2 mrad (V) X-ray beam [*i.e.* 61.2 mm (H) × 4.08 mm (V) at 20.4 m from the source] is calculated to be 529 W. Asaoka *et al.* (1992) tested the effects of high-power undulator beams (Photon Factory, KEK, Tsukuba, Japan) on 0.3 mm-thick Be windows with comparable beam size and absorbed power. They found that the Be windows could not withstand such power levels, the thermomechanical failure which occurred being in accord with theoretical expectations [see also Maezawa *et al.* (1993) for a related study with multi-pole wiggler beams]. At the other extreme and in stark contrast, when the F6 *in vacuo* filter set is used there is only 0.177 mW mm^{-2} absorbed at the centre of the hutch 1B Be window (which is the maximum value in this case) and the absorbed power for the same-size beam is a mere 13.4 mW. The calculated absorbed power for the 2 mm-thick Be window at 135.8 m from the source (see Table 1 and Fig. 1*c*) with the F0 *in vacuo* filter set and the same 3 mrad (H) × 0.2 mrad (V) X-ray beam [now 407.4 mm (H) × 27.16 mm (V) in hutch 3B] is 437 W. The fact that this value is within 20% of that for the hutch 1B Be window may at first seem surprising but the expected increase associated with the thicker window has been offset by the presence of the two Be windows (plus air, He and Al) in hutch 2A (see Table 1), which were also included in the calculation.

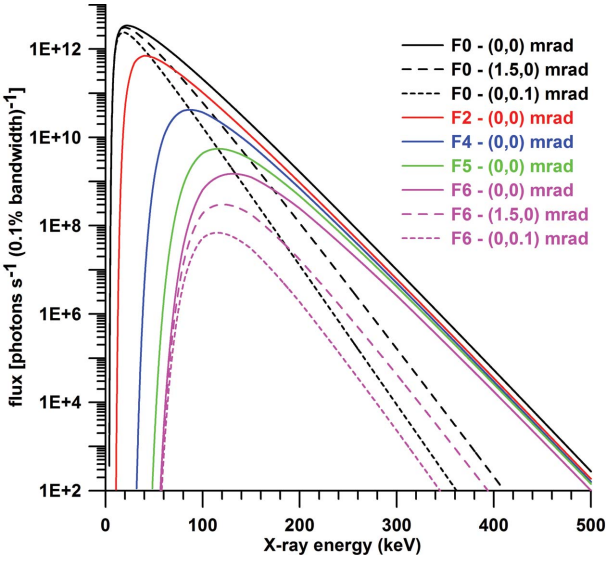

Figure 4
Calculated flux curves for a 1 mm × 1 mm X-ray beam at 22.3 m from the source. The SCMPW 3.00 T case from Fig. 2 has been considered and the calculation steps were 5 µm and 0.1 keV. Emittance effects have been included. The filtration, which is the same for all five cases considered, consisted of: 74 mm He path, 1.8 m air path, 0.35 mm Be window and 38 µm Al foil. The (*in vacuo*) filtration, which was varied, is as follows: F0, no filters; F2, 0.45 mm graphene, $15\sqrt{2}$ mm HD graphite and $2\sqrt{2}$ mm Al; F4, 0.45 mm graphene, $15\sqrt{2}$ mm HD graphite and $2\sqrt{2}$ mm Cu; F5, 0.45 mm graphene, $15\sqrt{2}$ mm HD graphite, $2\sqrt{2}$ mm Al and $2\sqrt{2}$ mm Mo; F6, 0.45 mm graphene, $15\sqrt{2}$ mm HD graphite, $2\sqrt{2}$ mm Al, $2\sqrt{2}$ mm Mo, plus 4.65 mm Cu (*ex vacuo*; Gammex 116 HVL attenuator set). See text for further details; in particular Table 3.

3.4. Detectors

Much of the foregoing discussion has implicitly assumed the use of an idealized photon-counting detector (PCD). In reality a beamline such as IMBL employs a wide range of 'detectors' including:

(i) Fluorescent screens, such as ZnS, $CdWO_4$, $Gd_2O_2S:Tb^{3+}$ (Tb-doped Gadox).

(ii) X-ray sensitive/self-developing papers, such as the ubiquitous pink, yellow or green 'burn paper'.

[12] *cf.* 44.6 W mm^{-2} for the new 0.6 mm diamond filter (*in vacuo*), with the SCMPW operating at 3.00 T; this filter is located at 8.2 m from the source (in the FE), with the new mask (3.8 mrad × 0.3 mrad) at 7.6 m. The corresponding (integrated) absorbed power is 3.06 kW.

Table 5
Values of (first) HVL and homogeneity factor (HF) for both Al and Cu (from *spec.exe*) corresponding to the flux curves in Fig. 4.

In vacuo filter sets F1 and F3 are not considered until later in the paper but their results are included here for completeness.

In vacuo filter set	Beam position (mrad)	(First) HVL Al (mm)	HF Al	(First) HVL Cu (mm)	HF Cu
F0	(0, 0)	1.13	0.401	0.0373	0.364
F0	(1.5, 0)	0.848	0.420	0.0278	0.414
F0	(0, 0.1)	0.679	0.442	0.0225	0.458
F1	*(0, 0)*	*2.92*	*0.593*	*0.103*	*0.474*
F2	(0, 0)	4.88	0.731	0.196	0.560
F3	*(0, 0)*	*11.8*	*0.953*	*0.897*	*0.773*
F4	(0, 0)	13.6	0.973	1.27	0.826
F5	(0, 0)	16.5	0.990	2.27	0.905
F6	(0, 0)	17.4	0.993	2.73	0.925
F6	(1.5, 0)	16.8	0.993	2.41	0.929
F6	(0, 0.1)	16.4	0.993	2.24	0.931

(iii) Film (*e.g.* photographic, polaroid, Gafchromic®) and imaging plates.

(iv) Ionization chambers (ICs)[13], Si diodes (with p-type and n-type semiconductor regions separated by an extended undoped or intrinsic region, 'PIN').

(v) Scintillation detectors, often based on NaI(Tl) crystals.

(vi) Bolometers/calorimeters (Krauss *et al.*, 2012; Tanaka *et al.*, 2015), especially for measurements of beam power.

(vii) Dosimeters, *e.g.* thermoluminescent dosimeters (TLDs), optically stimulated luminescence dosimeters (OSLs), thimble (Ubrich *et al.*, 2008), Roos® (Roos, 1993), PinPoint®, Markus® (Hill *et al.*, 2009), Semiflex™ (Liebmann *et al.*, 2015), Bragg-peak (Crosbie *et al.*, 2015) and Farmer (Farmer, 1955) ionization chambers, alanine, PRESAGE® [radiochromic plastic; Adamovics & Maryanski (2006) and Gagliardi *et al.* (2015)], Geiger-Müller (GM) tubes, metal-oxide semiconductor field effect transistors (MOSFETs)[14], single-crystal diamond detectors (SCDDs), Si-based detectors such as the *X-Tream* dosimetry system (Petasecca *et al.*, 2012), other radiochromic materials such as Fricke, polyacrylamide and genipen gels (see, for example, Schreiner, 2004; Gorjiara *et al.*, 2011).

(viii) Si(Li), Ge, CdTe (*e.g.* Amptek™) detectors for energy-resolved measurements.

(ix) Position-sensitive/imaging detectors (*e.g.* Hall *et al.*, 2013), such as those based on charge-coupled devices (CCDs), hydrogenated amorphous-Si (a-Si:H), amorphous-Se (a-Se), complementary metal-oxide semiconductors (CMOS).

(x) Energy-sensitive imaging detectors, such as those developed by the Medipix collaboration and operating in single-photon-counting mode (*e.g.* Llopart *et al.*, 2002); see also, for example, Ryan *et al.* (2010) regarding the Maia detector technology, with particular application to high-resolution X-ray fluorescence mapping for sensitive chemical speciation.

[13] So-called 'split' ICs, containing split ion-chamber plates oriented at 90° to one another can be used as effective beam-position monitors (BPMs).
[14] MOSFETs have been shown to have the high spatial resolution required for microbeam dosimetry (*e.g.* Siegbahn *et al.*, 2009).

The program *spec.exe* can also provide output associated with CCD-like detectors, ICs and dosimeters. The extensive research and development capability of IMBL in imaging/tomography requires a full and quantitative understanding of the response of detectors such as CCDs. The X-ray energies at IMBL are too high to enable CCDs to be used in 'direct-detection' mode and so phosphors are employed (so-called 'indirect-detection' mode). The CCD signal derives from photon energy in the X-ray beam, rather than photon number, *e.g.* a 90 keV photon will produce a signal three times that of a 30 keV photon for a 'perfect' CCD. However, the CCD quantum efficiency can be (rather simplistically[15]) estimated as $1 - \exp(\mu_m \rho_s)$, where μ_m is the energy-dependent mass attenuation coefficient and ρ_s is the 'surface density' (or 'phosphor concentration'). ρ_s is the product of three quantities: the material's bulk density ρ, thickness t and packing fraction p. The phosphor thickness needs to be selected with a number of factors in mind, especially efficiency (which will improve with increasing thickness) and detector resolution (which will improve with decreasing thickness). A thin protective window is also usually included. If we consider a Tb-doped Gadox phosphor (P43) with ρ_s typically varying from 1 to 40 mg cm^{-2}, the quantum efficiency can, correspondingly, vary from 0.34 to 13% for a 90 keV photon and from 1.2 to 39% for a 30 keV photon. A typical window of 200 µm-thick Sigradur-K® would absorb the beam by less than 1% for all X-ray energies above 3 keV. *spec.exe* is able to perform such calculations for a variety of phosphors and windows.

When performing imaging/tomography studies at IMBL it is often important to quantify and control the absorbed dose for certain samples, perhaps with an associated compromise on image quality. This may apply when collecting extensive tomographic data sets in the case of animal, human or other biological tissue, polymers, proteins, some semiconductor devices, and so on. An ability to reliably deliver X-ray beams of known dose rates can be critical for medical/biomedical applications including those involving longitudinal studies. A reliable and robust model can provide suitable data which will, in turn, inform decisions on the optimum design of experiments, *e.g.* exposure times, number of tomographic projections, X-ray energy selection, choice of filters. In the case of radiotherapy studies at IMBL, quantification and documentation of beam qualities and dose rates is vital. In the clinical context of course, such details must finally be ascertained by *in situ* measurements for each individual case. In clinical trials at overseas synchrotron facilities such as Elettra and ESRF, having beam-quality, dose-rate and dose data is mandatory, and is essential for the development of specific treatment planning systems (*e.g.* Martínez-Rovira *et al.*, 2012) and dosimetry protocols (*e.g.* Prezado *et al.*, 2011). A definitive recommendation on the accuracy required for delivering an absorbed dose of ionizing radiation to a target volume in the clinical context (*e.g.* for eradication of a tumour) is still being

[15] A more rigorous treatment can be achieved by using, for example, the linear cascade model (*e.g.* Cunningham, 1998).

debated. However, an oft-quoted accuracy is ±5%; see discussion of this subject elsewhere (ICRU, 1976; IAEA, 2000). Synchrotron beams have proven to be very useful in assessing the dose response of a variety of detectors to kilovoltage X-rays; an example being the work of Kron *et al.* (1998), where monochromatic synchrotron beams were used to study detectors including TLDs, MOSFETs and Gafchromic film. Butler *et al.* (2015) have used IMBL to measure high-resolution spatial maps of dosimetric response for a number of ionization chambers used in radiotherapy applications.

If we characterize the X-ray beam as having an energy fluence rate of $\Psi(E)$, averaged within a cross-sectional area of S, then the X-ray energy attenuation rate for a sample of (constant) thickness t will be $\Psi(E)\,S\,\{1-\exp[-\mu_{\rm m}(E)\,\rho\,t]\}$. However, $\mu_{\rm m}(E)\,\rho$ is a measure of the number of interactions per unit thickness of material, which occur as the incident X-rays of energy E traverse the sample. If the aim is to calculate the absorbed dose or dose rate, as it is here, or to obtain experimental values *via* IC current measurements, as we will later, then $\mu_{\rm m,en}(E)\,\rho$ [where $\mu_{\rm m,en}(E)$ is the energy-dependent mass energy-absorption coefficient] is the appropriate quantity; see, for example, Berger (1961), Seltzer (1993) and Hubbell (1999). $\mu_{\rm m,en}(E)$ relates to the amount of energy dissipated by the secondary electrons, released as a result of the interactions (such as ionization) between the X-rays of energy E and the material. This dissipated energy can, to a good approximation, be equated to the absorbed dose and represents the amount of energy available to create chemical and biological effects. The sample mass being irradiated is $\rho\,S\,t$ (density × volume) and so the absorbed-dose rate is $\Psi(E)\,\{1-\exp[-\mu_{\rm m,en}(E)\,\rho\,t]\}/(\rho\,t)$. If we then take the limit as $t\rightarrow 0$ we obtain the 'surface' absorbed-dose rate $\dot{D}_0(E) = \Psi(E)\,\mu_{\rm m,en}(E)$. This can be shown, for example, to be consistent with the expression for surface absorbed dose derived by Howells *et al.* (2009) [see their equation (2)]. We can then integrate over E to obtain the dose rate for the entire X-ray beam,

$$\dot{D}_0 = \int \dot{D}_0(E)\,{\rm d}E = \int \Psi({\rm E})\mu_{\rm m,en}(E)\,{\rm d}E. \qquad (1)$$

Using conversions (*e.g.* keV to J) will result in units of J kg^{-1} s^{-1}, *i.e.* Gy s^{-1}.

Fig. 5 shows the two-dimensional surface absorbed-dose rate distribution[16] for the SCMPW operating at 3.00 T, 22.3 m from the source (hutch 1B), and with the F4 *in vacuo* filter set. The range of dose rates is from 0 to 1024 Gy s^{-1}. The small grey rectangle represents 12 mm (H) × 1 mm (V) and is a typical beam size used for certain radiotherapy experiments at IMBL, such as MRT irradiation of flasks containing cultured mouse mammary tumour cells (*e.g.* Ibahim *et al.*, 2014). The minimum dose rate within this small beam is 881 Gy s^{-1} and the average is 974 Gy s^{-1} (86% and 95% of the maximum, respectively). The maximum dose rate is 155 Gy s^{-1} if the F5 *in vacuo* filter set is used instead of F4, and 45 Gy s^{-1} if F6

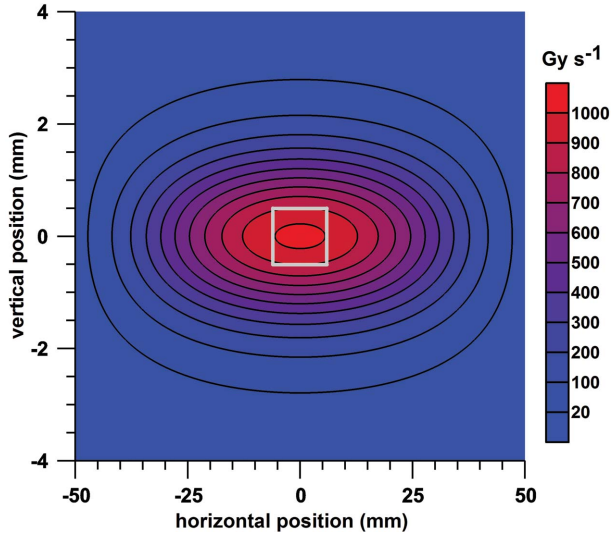

Figure 5
Dose-rate distribution for the SCMPW 3.00 T case. The *in vacuo* filters were 0.45 mm graphene, $15\sqrt{2}$ mm HD graphite and $2\sqrt{2}$ mm Cu (referred to as F4 previously), and the fixed filters consisted of 74 mm He path, 1.8 m air path, 0.35 mm Be window, and 38 µm Al foil. Note that the horizontal and vertical scales are quite different. The small grey rectangle represents 12 mm (H) × 1 mm (V). Other relevant parameter values were 3.032 GeV, 200 mA, 22.3 m from the source. Emittance effects were included. Component distributions were calculated from 1 to 999 keV in steps of 2 keV. The calculation steps were 0.1 mm horizontally and 0.01 mm vertically.

is used instead of F4. The output from *spec.exe* includes a summary file which provides the dose-rate range for each component distribution (*i.e.* X-ray energy) calculated (this is also true for angular flux density, intensity and power density). Given a dose rate of 1 kGy s^{-1}, the step-and-shoot radiotherapy mode can deliver individual absorbed doses down to 30 Gy (requiring the MRT shutter to operate reliably at 30 ms). If lower doses are required one may need to consider increasing the distance from the source, increasing filtration, decreasing ID field, or decreasing ring current (see earlier discussion). If the dynamic radiotherapy mode is used, the delivered absorbed dose is given by the (static) dose rate multiplied by the vertical size of the beam (h) and the number of passes (n) used, and divided by the vertical scan speed (s) of the motorized stage, *i.e.* $D_0 = n\dot{D}_0\,h/s$. If the beam is not uniform in the vertical direction the relevant dose rate is the average value. So in this case an absorbed dose of 30 Gy would require a scan speed of 33.3 mm s^{-1}, for a single pass ($n = 1$). This is somewhat beyond the capability of the current translation stage used at IMBL (maximum speed of 20 mm s^{-1}). However, in this delivery mode there is the additional option of decreasing the vertical size of the X-ray beam.

Whilst free-air ICs can have some quite serious limitations when used with the very intense, collimated X-ray beams which can be generated at IMBL, they are very simple, robust, convenient and still have an important role to play at the beamline. A big advantage is that they can be used *in situ* with essentially no perturbation of the X-ray beam itself. They also possess a quite uniform response over a wide range of X-ray energies. Air-filled ICs have been recommended for radiation

[16] This dose-rate distribution is for air; *spec.exe* can also calculate such distributions for water or graphite as required.

dosimetry in clinical applications; see, for example, IAEA (2000, 2007). At IMBL, fixed ICs are generally of parallel-plate geometry, in ambient air and often without windows, *i.e.* the X-ray beam travels parallel to and in-between the two plates ['free-air chambers (FACs)']. If being used as a monitor of beam variations, operation is relatively straightforward. If we wish to make absolute measurements for dosimetry for example, the limitations alluded to above need to be addressed and the range of applicability firmly established. We will assume that the X-ray beam being measured has a constant dose rate and that the radiation is continuous, not pulsed.[17] The IC current associated with a particular X-ray energy is easily shown to be given by

$$I(E) = \Psi(E)\, S \left\{1 - \exp\left[-\mu_{\rm m,en}(E)\, \rho_{\rm air}\, L\right]\right\} Q/\left[W_{\rm air}\, K_{\rm IC}(E)\right], \quad (2)$$

where $\mu_{\rm m,en}(E)$ is for ambient air in this case[18], L is the length of the IC plates (in the direction of the X-ray beam), Q is the elementary (electron) charge and $W_{\rm air}$ is the average energy required to create an ion pair. If the air density at the standard temperature and pressure (STP) used by NIST (20°C and 101325 Pa) is $\rho_{\rm air,STP}$, then the appropriate correction (based on the ideal gas law) for other temperatures (T) and pressures (P) is

$$\rho_{\rm air} = \rho_{\rm air,STP}\left(\frac{293.15}{T}\right)\left(\frac{P}{101325}\right) = \frac{\rho_{\rm air,STP}}{K_{\rm TP}}. \quad (3)$$

La Russa *et al.* (2007) report on detailed experimental and theoretical considerations of $K_{\rm TP}$.

Finally, $K_{\rm IC}(E)$ is the IC correction factor and appears in the denominator of (2) since we are correcting the calculated IC current. $K_{\rm IC}(E)$ can have several contributing factors, assuming charged-particle equilibrium (CPE) (see, for example, Greening, 1985; Attix, 1986),

$$K_{\rm IC} = K_{\rm e}K_{\rm sc}K_{\rm fl}K_{\rm s}K_{\rm tr}K_{\rm h}K_{\rm pol}K_{\rm a}K_{\rm d}\left[K_{\rm TP}K_{\rm Q}\right], \quad (4)$$

where $K_{\rm e}$ is for electron loss, $K_{\rm sc}$ photon scattering, $K_{\rm fl}$ fluorescence re-absorption, $K_{\rm s}$ recombination, $K_{\rm tr}$ aperture transmission, $K_{\rm h}$ humidity, $K_{\rm pol}$ polarity, $K_{\rm a}$ attenuation and $K_{\rm d}$ field distortion. $K_{\rm TP}$ has been included in square brackets as its appearance here assumes that $\rho_{\rm air}$ is replaced by $\rho_{\rm air,STP}$ in (2) and that $\mu_{\rm m,en}(E)\, \rho_{\rm air}\, L \ll 1$ (see discussion below). In cases where an IC has been calibrated with a particular X-ray beam, there may also be a factor $K_{\rm Q}$ to allow for beam quality. Detailed discussions of these and other correction factors have been provided by various authors, *e.g.* Burns & Büermann (2009). We have divided by $K_{\rm IC}$ in (2), so that the IC current obtained can be directly compared with a measured value. In some cases these individual correction factors (such as $K_{\rm tr}$) are not relevant here and in other cases they are extremely close to unity, for example $K_{\rm h}$ (typically ∼0.998), and so can be neglected. $K_{\rm pol}$ is conventionally defined as $(|M_+| + |M_-|)/(2M)$ for measurements with positive and negative polarities, the unsubscripted value being the 'usual' measurement (M_+ in our case). Measurements of $K_{\rm pol}$ have been undertaken and found to be unity within error (see also §4.4.2). The values of $K_{\rm sc}$ and $K_{\rm fl}$ will be included in our results in §4, but are usually ∼0.999. On these grounds we will only concern ourselves (in §4) with $K_{\rm e}$ and $K_{\rm s}$, the former being the major source of energy dependence. The effect of the linearly polarized nature of the synchrotron beam has been checked by using an X-ray beam of small cross section and comparing measurements made with the IC in the usual orientation (plates horizontal) with those when the IC is rotated by 90° about the beam direction (optic axis), *i.e.* plates vertical (see §4.4.2). The measured differences are, in certain cases, significant. Harty *et al.* (2014) have also discussed the role of polarization in ADC IC (Advanced Design Consulting USA, Inc.) current measurements, including justifying the neglect of polarization effects in modelling electron loss in the context of certain X-ray beams/energies used at IMBL. Nariyama *et al.* (2004) have also considered the role of linear polarization in respect of IC electron-loss effects.

In this paper we will not distinguish between absorbed dose and Kerma (Roesch, 1958), although they are quite distinct quantities. The latter involves the mass energy-transfer coefficient, $\mu_{\rm m,tr}(E) = \mu_{\rm m,en}(E)/[1 - g(E)]$, where $g(E)$ represents the fraction of the kinetic energy of electrons liberated by photons that is lost in radiative processes (in particular Bremsstrahlung). The value of $g(E)$ for the X-ray energies of concern here is very small (∼0.001 or less) and so absorbed dose and Kerma, assuming CPE, are essentially equal in value.[19] There can be another IC correction-factor contribution, $K_{\rm br}$, due to Bremsstrahlung re-absorption, but this is very close to unity in the current context and $K_{\rm br}/(1 - \overline{g})$ is unity to a very good approximation ($\overline{g}$ being a spectrally weighted average of g).

As a theoretical example, we consider using (2) and integrating over E, with $\rho_{\rm air} = 0.001205$ g cm^{-3} (Hubbell & Seltzer, 1995), $T = 20$°C and $P = 101325$ Pa, $L = 5.0$ cm (ADC IC-105 IC), $Q = 1.602176565 \times 10^{-19}$ C, $W_{\rm air} = 33.97$ (0.05) eV (see, for example, Attix, 1986; Podgorsak, 2005) and $K_{\rm IC}(E) = 1$ for the present. The predicted IC currents for a 1 mm × 1 mm X-ray beam at 22.3 m for the SCMPW 3.00 T case, the fixed filtration mentioned previously (*e.g.* see Fig. 4 caption) and *in vacuo* filter sets F0, F2, F4, F5 and F6 would be 2.57 mA, 0.220 mA, 11.1 μA, 1.53 μA and 0.423 μA, respectively. In the

[17] Ion mobilities are $\sim 2 \times 10^{-4}$ m^2 s^{-1} V^{-1} and so for typical IC operating conditions ions will take several hundred microseconds to traverse the gap between the IC plates (electrodes). This is quite long when compared with the separation time between bunches in multi-bunch mode (2 ns; see §2) and so the radiation can be treated as being continuous in nature.

[18] We use the values of Hubbell & Seltzer (1995) by default, but have investigated other sources of data such as Buhr *et al.* (2012).

[19] In general, absorbed dose and Kerma do not occur at the same place in the irradiated sample. The former relates to energy deposited along the length of a charged-particle 'track', whereas the latter occurs at an upstream *point*. These concepts also relate to the so-called 'build-up' effect in the near-surface region of the sample (see also §4.2), where charged-particle equilibrium (CPE), or transient charged-particle equilibrium (TCPE) (see Dutreix *et al.*, 1965), has not been established. Strictly speaking, absorbed dose and Kerma can also differ within a sample if there is a sudden discontinuity of material composition, such as at a boundary between soft tissue and bone or a contrast medium. This will, however, only be the case in very close proximity to the interface (of the order of μm) and can be neglected here.

case of typical monochromatic X-ray beams, IC currents of order tens of nA or less can be expected.

Fig. 6(*a*) provides a more practical example and shows the experimental results obtained from vertical position scans, using a horizontal micro-slit, of the spatially fractionated X-ray beams typically employed at IMBL for step-and-shoot MRT. The two horizontal-beam MRT collimators used both have 12 × 200 μm periods, with one comprising 25 μm Kapton and 175 μm WC layers, the other 50 μm Kapton and 150 μm WC layers. These layers are approximately 5 mm long, in the beam direction, and 30 mm wide, normal to the beam (horizontal). The collimators are flushed with He and the housing is water-cooled. Two types of scan are shown for each collimator, one with the micro-slit stationary and the collimator moved ('collimator scan') and the other with the collimator stationary and the micro-slit moved ('micro-slit scan'). The former provides information on the alignment and integrity of each of the 12 microbeams, whereas the latter incorporates the profile of the (broad) X-ray beam, including the vertical roll-off. As can be seen from the scans, the housing obscures two microbeams on one side for the 25 μm/175 μm collimator, and one microbeam on each side for the 50 μm/150 μm collimator. An ADC IC-105 IC, operated at 2 kV, was used to record the signal. In plotting the results the direction of the abscissa axis has been reversed for the micro-slit scans, relative to that for the collimator scans, so that the microbeams are in correct registration. The former has also been slightly demagnified to compensate for the separation between micro-slit and collimator, *i.e.* the factor 21.9 m/22.3 m = 0.982 has been applied. The effect of the vertical roll-off is quite apparent in the two micro-slit scans and, for actual sample irradiation, slits prior to the collimators are usually set to ∼1 mm vertically in order to select just five microbeams of near-equal peak signals. Slits are also used to limit the size of the microbeams horizontally, to ensure that the contribution of the horizontal roll-off is acceptable.

MRT capitalizes on the so-called 'dose-volume effect', first reported by Zeman *et al.* (1961), and involving their observation that normal tissue was better able to tolerate high radiation doses (in this case, in the form of a deuteron beam) for small beam sizes, down to 25 μm in diameter. They state in their summary '*that tissue radiosensitivity is inversely related to the tissue volume being irradiated*'. Bencokova *et al.* (2008) have provided an insightful comparison, from a radiobiology perspective, of different (synchrotron-based) radiotherapy strategies, including MRT. In MRT one of the most important parameters is the PVDR. Using (1) and (2) we can obtain

$$\dot{D}_0 \approx W_{\rm air} \int I(E)\, K_{\rm IC}(E)\, {\rm d}E/(S\, \rho_{\rm air}\, L\, Q), \qquad (5)$$

where the integral represents the total, corrected, IC current. The approximation made in deriving (5) is that $\mu_{\rm m,en}(E)\, \rho_{\rm air}\, L \ll 1$ for all E. In our present case this quantity is less than 0.01 for X-ray energies of 14 keV and above, and less than 0.1 for 6.7 keV and above. Given the 'hard' nature of the X-ray beam typically used for MRT, (5) is thus quite valid. In this example, the magnitude and nature of $K_{\rm e}(E)$ and $K_{\rm s}$, and thereby $K_{\rm IC}(E)$, is such that from (5) the ratio of the measured peak and valley IC currents will be a quite reasonable estimate of the PVDR. Using the third to seventh microbeams as our set of five, the PVDR from the raw

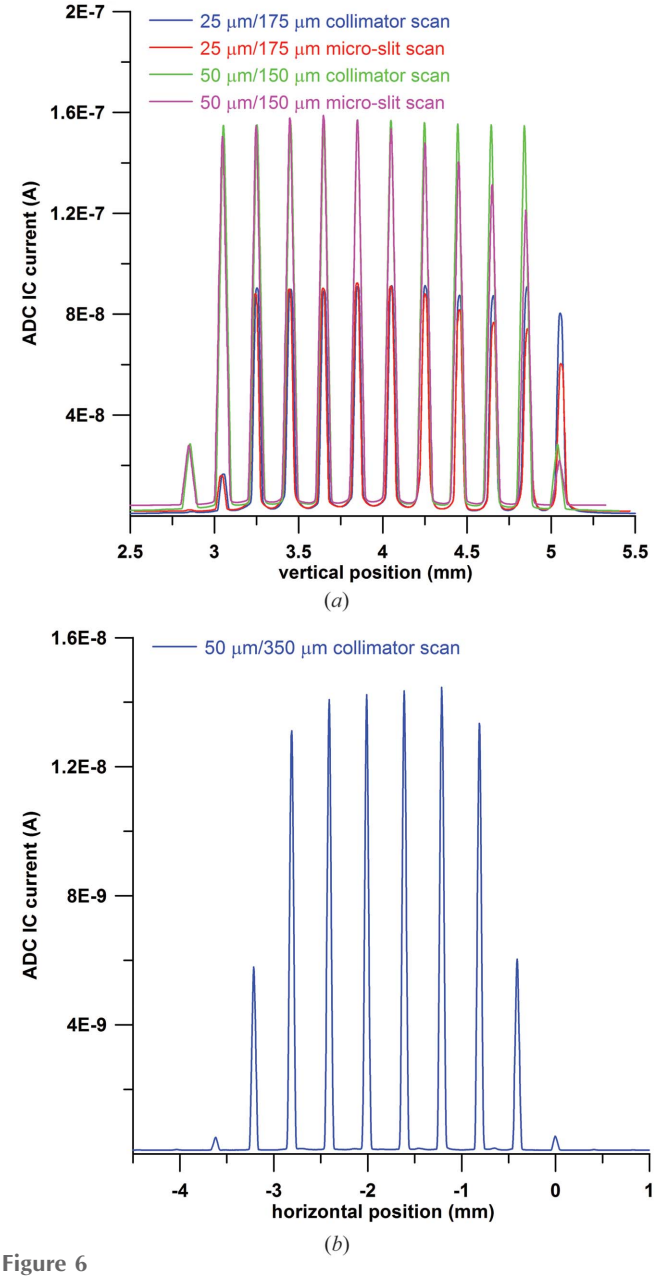

Figure 6
(*a*) Vertical position scans (step size 2 μm) collected in hutch 1B for horizontal-geometry MRT collimators (positioned at 21.9 m). 3.033 GeV, 200 mA (top-up mode); SCMPW field 3.00 (0.05) T; F4 *in vacuo* filter set; fixed filters consisted of 0.6 mm diamond filter (*in vacuo*), 74 mm He path, 0.35 mm Be window (now at 21.1 m instead of 20.4 m, see Table 1), 38 μm Al foil and 1.6 m air path; P = 100800 (300) Pa and T = 24.4 (0.1)°C. The horizontal micro-slit [measured to be 40 (5) μm opening] was at 22.3 m and the ADC IC at 22.8 m (operated at 2 kV). (*b*). Horizontal position scan (step size 5 μm) collected in hutch 2B for the vertical-geometry MRT collimator (positioned at 33.5 m). 3.032 GeV, 200 mA (top-up mode); SCMPW field 3.00 (0.05) T; F4 *in vacuo* filter set; fixed filters consisted of 0.6 mm diamond filter (*in vacuo*), 6.7 m He path, 1.05 mm Be, 114 μm Al, 125 μm Kapton and 6.1 m air path. The 40 μm vertical micro-slit was at 34.0 m and the ADC IC at 34.3 m. See text for further details.

data (micro-slit scans) shown in Fig. 6(*a*) is 26 (3) for the 25 µm/175 µm collimator and 29 (2) for the 50 µm/150 µm collimator. The ratio of the respective peak IC currents is 0.58 (0.02). If we deconvolute these scan data with a 40 µm-wide top-hat function (representing the micro-slit), the PVDRs become 37 (5) and 33 (6), respectively, and the ratio of peak IC currents 0.91 (0.06). The errors in the experimental PVDR values are dominated by the errors in the valley IC currents. Crosbie *et al.* (2008) provide, in their Table 2, the PVDR results (to the surface of water) from Monte Carlo simulations by various authors and using different radiation-transport codes, for the same geometry as our 25 µm/175 µm collimator. The average of the four relevant values is 37, in excellent (and undoubtedly somewhat fortuitous) agreement with the corresponding experimental value obtained above. It should be noted that the PVDR value will also depend on the number of microbeams involved (see, for example, Nariyama *et al.*, 2011). Generally, we would expect PVDR values to increase with increasing period of the MRT collimator and with decreasing beam size (see, for example, Bräuer-Krisch *et al.*, 2015). PVDR values typically decrease with increasing depth in the irradiated sample; this decrease being more pronounced near the entrance surface. A slight increase of PVDR at large depths can be observed, but this is usually associated with proximity to an exit surface, where there is a concomitant reduction in back-scatter (see, for example, Siegbahn *et al.*, 2006).

Fig. 6(*b*) shows the experimental result for a horizontal position scan of the same micro-slit, now mounted vertically, in the case of IMBL's (new) collimator used for dynamic MRT. Apertures have been used to define a beam approximately 4 mm (H) × 1 mm (V) at the collimator, thereby selecting a small subset of the 125 50 µm-wide microbeams. The MRT collimator used has a 400 µm period, comprising 350 µm WC layers and 50 µm (He-flushed) gaps. These layers are approximately 8 mm long, in the beam direction, and 4 mm high, normal to the beam (vertical). The collimators are flushed with He and the housing is water-cooled. The abscissa axis has been slightly demagnified to compensate for the separation between micro-slit and collimator, *i.e.* the factor 33.5 m/34.0 m = 0.985 has been applied. Using the four central microbeams in Fig. 6(*b*), the PVDR value obtained is 109 (3). If we again deconvolute the scan data with the top-hat function representing the micro-slit, the PVDR becomes 116 (3).

4. Comparisons with experiment

The model we are using, as implemented and embodied in *spec.exe*, has been validated to some extent through our comparison of calculation results with those from *SPECTRA*. In this section we will provide further validation *via* comparison with certain experimental results obtained at IMBL.

4.1. Practical aspects of *in vacuo* filters

Firstly, we provide a brief discussion of some of the more practical aspects of the *in vacuo* filters used at IMBL, inasmuch as they affect experimental results. The structural integrity/thickness of these filters is periodically checked by translating them vertically in an X-ray beam (polychromatic) of small cross section, whilst monitoring the transmitted intensity with an IC. The *in vacuo* filter paddles used at IMBL, which each support four separate filters, are accurately aligned but there is still scope for small departures from the nominal filter angles (see §3.3 and Table 1). These might result from small angular deviations of a paddle about the vertical drive axis or from slight bending of the paddle along its length. We have thus performed precise experiments involving recording ADC IC currents for particular *in vacuo* filter combinations and then systematically removing particular filters and 'mimicking' them with an equivalent *ex vacuo* filter mounted on an accurate (vertical) rotation stage. Matching the IC current values, with the IC fixed in position, enables us to determine the effective filter angle quite precisely and accurately, and values of IC correction factors such as K_e and K_s are not required. Particular attention was paid to ensuring that any extraneous scatter, which might compromise the results, was minimized. The effective filter angle determined in this way does not necessarily provide us with a true description of the disposition of a particular filter[20], but does provide the true material thickness as traversed by the X-ray beam. The average effective angle for five critical (Al-, Cu- and Mo-based) filters was determined to be 45.0 (2.1)°, in excellent agreement with the nominal 45° for all of the associated filter paddles. However, the quite large estimated standard deviation reflects the considerable variation in individual values, from 41.8 (0.3)° to 47.0 (0.4)°. Where possible, these determinations were repeated for high-purity filter materials from different sources (*e.g.* Cu from Advent Research Materials Ltd in addition to that from a Gammex 116 HVL attenuator set) and the results were found to be very consistent. In cases where calculations are compared with experimental results in §4, these effective filter angles are included.

In the case of the carbon-based *in vacuo* filters (present in the upstream paddles) the same approach was applied. However, the results obtained were inconsistent and further investigation was deemed necessary. These filters are subjected to very high absorbed-power densities and are critical in protecting downstream beamline components (see §3.3). Except for quite special operating conditions, principally low ring current, the presence of certain carbon (graphite or graphene) *in vacuo* filters is mandatory for any IMBL experiments (imaging, tomography or radiotherapy). Given these anomalous results, plus other anecdotal evidence that these filters were not behaving as expected, samples of the HD graphite were investigated with both synchrotron-based powder diffraction and laboratory-based small-angle X-ray scattering (SAXS). Evidence of scattering from both crystalline and non-crystalline (*e.g.* amorphous) components was apparent. Various authors have discussed the role of scat-

[20] Comparison of the results obtained for filters housed in the same paddle does, however, give some indications, *e.g.* if one assumes that a given paddle is not 'twisted' along its length.

tering, in addition to photoelectric (or 'true') absorption, in the attenuation of X-rays (*e.g.* DeMarco & Suortti, 1971). SAXS from HOPG is still the subject of considerable attention, including the recent study of the complications associated with double Bragg scattering (Ohmasa *et al.*, 2016). Consequently, in the present case, direct attenuation measurements were performed at IMBL as a function of X-ray energy with the carbon-based *in vacuo* filters, *i.e. in situ*.

The DCLM was used to select monochromatic X-ray beams with 12 different energies from 20 to 110 keV, in hutches 1B and 2B. The ring current was maintained at approximately 2 mA (such a beam has an exceedingly long life-time) to ensure that all *in vacuo* filters could be removed as needed, without any risk to downstream optical components (especially the DCLM first Si crystal). Transmission measurements were made with two ADC ICs simultaneously (both operating at 2 kV; one in hutch 1B at 22.8 m from the source and the other in hutch 2B at 35.3 m) for the *in vacuo* (carbon-based) filter combination of graphene (0.45 mm in first paddle; nominal filter angle 0°, *i.e.* filter normal to beam) and graphite (HD; 5 and 10 mm in second and third paddles, respectively; nominal filter angles 45°). These filters are now used almost universally for IMBL experiments conducted at 200 mA ring current, with only the fourth and fifth paddles being changed. The beam size at the first IC was 0.81 mm (H) × 1.15 mm (V); and 1.26 mm (H) × 1.77 mm (V) at the second IC. The ratio of the currents for a given ADC IC will be the same as the ratio of the corresponding fluxes, given that K_s is very close to unity here [see (2)].

Fig. 7 shows the experimentally determined values of μ_m, together with values from the NIST database (see §3.3). At X-ray energies above 70 keV there is excellent agreement with the NIST values but a systematic discrepancy occurs with decreasing X-ray energy. This is consistent with the presence of some extraneous scattering which is not accounted for in the NIST values. Before accepting these experimental μ_m values, some investigation of the role of harmonic contamination in the lower-energy data was deemed prudent. As an (albeit extreme) example of harmonic contamination, Fig. 8 shows the results of transmission measurements obtained at 25 keV for a 2 mm-thick Al filter (Gammex 115A HVL attenuator set), which was rotated about a vertical axis (almost ±90°), at 22.3 m from the source, in order to vary the effective Al thickness, as seen by the X-ray beam. The experimental details are similar to those for Fig. 7, with just one ADC IC used (hutch 1B). The ring current was the nominal 200 mA (user-beam, top-up mode); filter paddle 4 had 2 mm Al (at 45°) and paddle 5 was empty; the beam size at the IC was approximately 0.62 mm (H) × 3.1 mm (V), the narrow horizontal dimension chosen so that the *ex vacuo* Al filter would still intercept all of the X-ray beam when rotated to extreme angles (∼±89°). Experimental transmission data sets were collected for different thicknesses of *ex vacuo* Cu (Gammex 116 HVL attenuator set) placed upstream of the *ex vacuo* Al and then converted to effective μ_m values. The measured IC currents involved vary by a factor of more than 300 and so the variation in signal-to-noise ratio is obvious. In the case of a

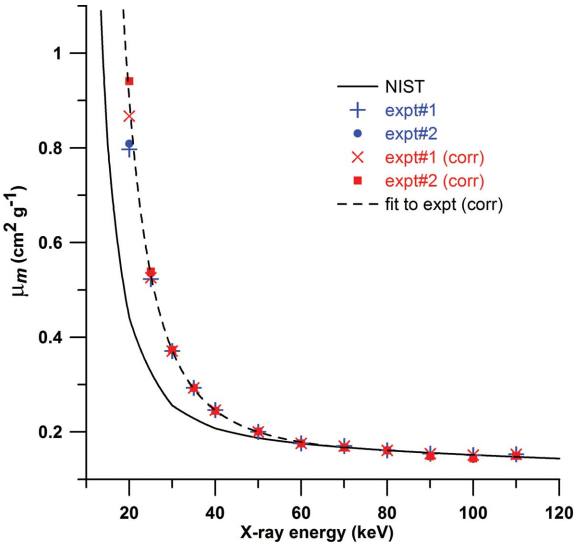

Figure 7
Experimental values of mass-attenuation coefficient μ_m as a function of X-ray energy, derived from data collected for the most common *in vacuo* carbon-filter combination used at IMBL. Values from the NIST database are included for comparison. Corrections have also been included for the effect of harmonic contamination in the raw data. See text for further details.

perfectly monochromatic 25 keV X-ray beam, these μ_m values would all have the same value (1.86 cm^2 g^{-1} from the NIST database), independent of Cu thickness and Al rotation angle. The fact that there are harmonics present results in beam hardening, which manifests itself as the vertical shift of the curves (due to the variation of Cu thickness) and the curvature

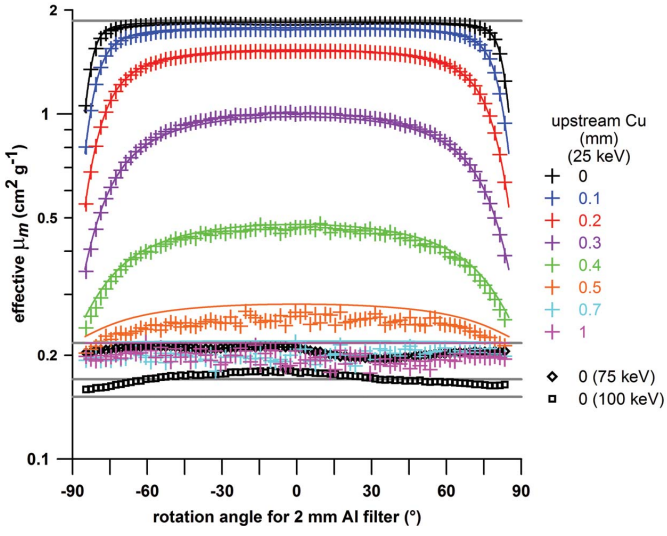

Figure 8
Experimental values of effective mass-attenuation coefficient μ_m as a function of rotation angle for a 2 mm Al filter obtained with a 25 keV monochromatic X-ray beam. Different thicknesses of Cu filter have been included upstream of the Al. Values of μ_m from the NIST database, for the fundamental and first three harmonics, are included for comparison (grey lines). Experimental values are also shown for 75 and 100 keV monochromatic beams. Each of the 25 keV data sets has an accompanying solid line which is from calculation and assuming the presence of just the fundamental and λ/3 components. See text for further details.

away from horizontal toward the rotation-angle extremes (due to the variation of effective Al thickness). The grey horizontal lines correspond to the NIST-database values of μ_m for the fundamental (25 keV) and harmonic (75, 100 and 125 keV) components of the beam, from top to bottom, respectively. We have also included experimental results, obtained using no *ex vacuo* Cu, with the DCLM tuned to diffract 75 and 100 keV fundamental components. In these cases the flux for any harmonic components (225 keV and above) is insignificant, and there is quite reasonable agreement with the corresponding NIST values.

We can calculate the expected form of the effective-μ_m curves for different Cu thicknesses by assuming that the X-ray beam prior to any *ex vacuo* Cu comprises only fundamental (25 keV) and λ/3 harmonic (75 keV) components, and that the beam with 1 mm *ex vacuo* Cu (and no *ex vacuo* Al) can be attributed solely to the λ/3 component. These are the corresponding solid lines in Fig. 8 and show excellent agreement with the experimental data sets for Cu thicknesses up to and including 0.4 mm. In the cases of 0.5, 0.7 and 1 mm Cu these calculations tend to overestimate the effective μ_m values. This discrepancy is associated with our neglect, in the calculations, of the presence of higher-order (such as λ/4 and λ/5) harmonics which are quite evident in the experimental data.

We provide a further example of the effects of harmonic contamination in Fig. 9. The DCLM was set to the X-ray energy for the Rh *K*-edge (23.23 keV): 3.033 GeV, 185 mA (top-up mode); F2 *in vacuo* filter set; SCMPW operating at 3.00 T; DCLM crystals (see below for more details) bent with a radius of curvature of 10 m (concave when viewed from the X-ray source). Two-dimensional distributions of IC current were measured as a function of the Bragg-rotation angles for the two DCLM Si crystals. Three different ICs, located in hutches 1B, 2A and 2B, were employed simultaneously. A 100 µm (actually 0.004 inch) W filter was positioned in between the second and third ICs, and a 12.5 µm-thick Rh filter between the first and second ICs. These filters were selected due to the ratio of the respective *K*-edge X-ray energies being very close to 3 (69.53 keV: 23.23 keV = 2.993)[21], enabling the concomitant effects to be seen for the λ/3 harmonic and fundamental components in the beam (respectively) simultaneously. The two Bragg-rotation angles covered the range ±0.04° in 0.0005° steps, providing a total of 25921 data points in each of the two-dimensional distributions. These are basically characterized by a thin streak extending diagonally from the lower-left to top-right corner, corresponding to the variation of X-ray energy. In the interests of more efficient presentation, we have applied an affine transformation in Fig. 9, involving the translation of each column of values (parallel to the $\Delta\theta_1$ axis, *i.e.* a line of constant $\Delta\theta_2$) by $-\Delta\theta_2$ (see, for example, Mathieson & Stevenson, 1985). In the

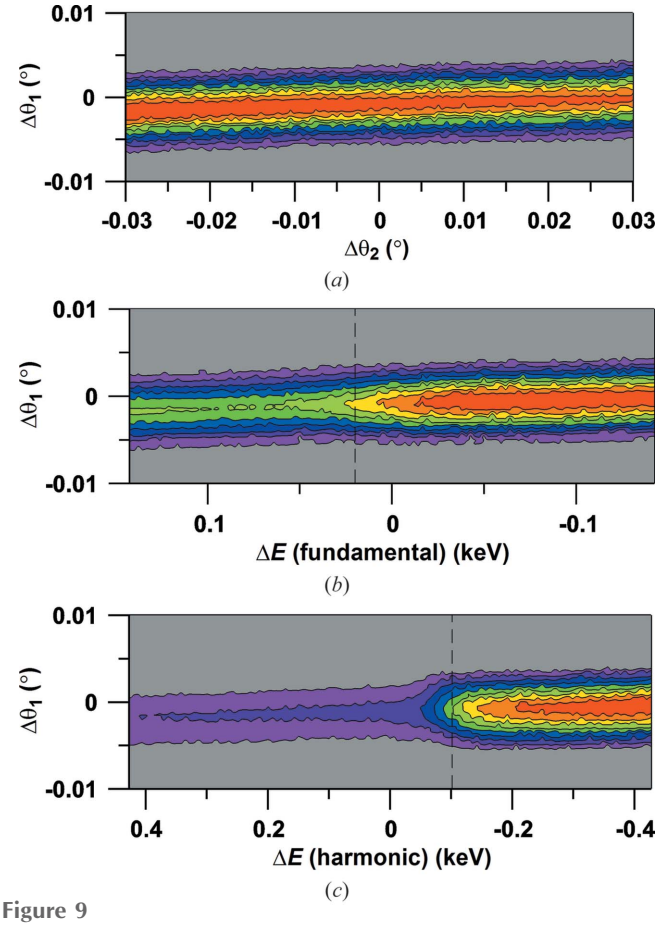

Figure 9
Two-dimensional IC-current distributions collected as a function of Bragg-rotation angle for the first and second crystals of the DCLM ($\Delta\theta_1$ and $\Delta\theta_2$, respectively). The contour levels are from 0 to 100% of the maximum current value in steps of 10%. (*a*) IC at 23.8 m from the X-ray source (hutch 1B); (*b*) IC at 31.3 m (hutch 2A); (*c*) IC at 36.0 m (hutch 2B). See text for further details.

case of Figs. 9(*b*) and 9(*c*) we have used the differential form of Bragg's law to convert the horizontal axis from $\Delta\theta_2$ to change in X-ray energy ΔE. Fig. 9(*a*) shows the experimental distribution in the absence of any extra absorption edges, whereas Fig. 9(*b*) clearly shows the effect of the Rh *K*-edge for the fundamental component, and Fig. 9(*c*) the effect of the W *K*-edge for the λ/3 harmonic component (the transmission of the fundamental for 100 µm of W is less than 0.02%, whereas the transmission of the harmonic for 12.5 µm of Rh is ∼95%). The vertical dashed lines represent our estimates of the *K*-edge (mid-)positions, based on calculations of the expected IC-current change across the absorption edges. The Rh *K*-edge position is 20 eV from the anticipated (central) position and the W *K*-edge position approximately 100 eV below. Thus, experimentally, the energy of the λ/3 harmonic is 3 × 20 eV + 100 eV = 160 eV higher than the W *K*-edge energy, *cf.* 3 × 23.23 keV − 69.53 keV = 160 eV, in excellent agreement. We have not allowed for the deviations from the exact Bragg angle which occur due to refraction effects; however, given that these values are 2.2 and 0.24 arcsec for the fundamental and harmonic components, respectively [calculated using equation (29) of Stevenson *et al.* (2012)], such neglect is justifiable. We

[21] Given the DCLM energy range of ∼17 to 120 keV, and excluding the highest-atomic number, radioactive elements from consideration dictates that we are limited to *K*-edges (rather than *L*-edges) and 12 atom pairs from Y/Tb to Sb/Bi (excluding Tc/Lu). Rh/W is the pair most closely satisfying the criterion, with other atom pairs also having issues with availability and/or practicality, *e.g.* Mo/Tm and In/Hg.

do not see any evidence of modulations in the IC current on the high-energy side of the absorption edges, as would be associated with EXAFS/XANES. This is not, however, surprising given the typical energy bandpass expected for the IMBL (bent-crystal) DCLM, a few tens of eV [as will be discussed below, and also consistent with the observed 'widths' of the edges seen in Figs. 9(*b*) and 9(*c*)].[22]

In order to allow for harmonic contamination in the lower-energy data presented in Fig. 7, we performed calculations of peak reflectivities (R_1 and R_2) and energy bandpasses (δE_1 and δE_2) as a function of X-ray energy and Bragg reflection (111, 333, 444 and 555) for each of the (meridionally) bent crystals in the DCLM. We largely followed the formalism developed by Erola *et al.* (1990) for the lamellar model, involving dividing the crystal into thin perfect-crystal slices of appropriately varying lattice spacing and orientation. This method is more simplistic than, say, the theoretical approaches of Penning & Polder (1961) and Polder & Penning (1964), or Takagi (1962, 1969) and Taupin (1964). However, the results obtained are quite satisfactory for the present purposes, as long as care is taken with the values of the lamella thickness and Poisson's ratio (ν).

In performing these calculations the following properties of the two Si crystals have been used: lattice parameter 5.4309 Å (NBS, 1976); Debye–Waller factor 0.45 Å^2 (Prager, 1971); atomic scattering-factor parameterization of Doyle & Turner (1968); anomalous-dispersion corrections have been derived by logarithmic interpolation of data values from the NIST database (see Chantler *et al.*, 2005); both crystals are 1.00 mm thick and bent (assumed cylindrically) to be concave when viewed from the X-ray source, the radius of curvature being 9.4 m for both crystals; both crystals use {111} Bragg planes [in the case of the fundamental (λ) component] with the Bragg-rotation axes (horizontal and normal to the optic axis) being a ⟨110⟩ direction[23]; the asymmetry angle (χ) is 14.7° for both crystals. Fig. 10 provides a schematic diagram, plus a photograph of one of the Si crystals. The fact that the two crystals have the same values of the relevant parameters, such as radius of curvature, simplifies the calculations. Referring to equation (3) of Erola *et al.* (1990), which is related to the lattice-angle change (and rocking-curve width), and Fig. 1 of Erola *et al.* (1990), we have the 'lower' case as long as the Bragg angle (θ_B) is smaller than χ, *i.e.* as long as the X-ray energy is higher than 7.8 keV (which is true of all cases considered here). The structure-factor calculations were performed as described by Stevenson *et al.* (2012); see their equation (20).

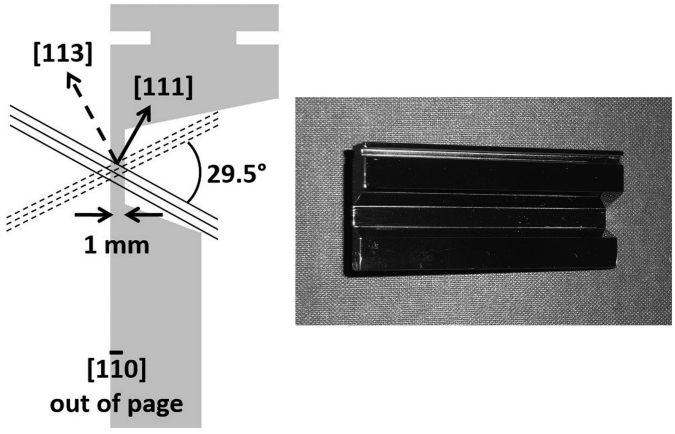

Figure 10
Schematic diagram (not to scale) (left) and photograph (right) of one of the DCLM Si crystals. The disposition of the diagram is such that, for the first crystal, the X-ray beam would be incident from the right and diffract from the (111) Bragg planes, with the [1$\bar{1}$0] rotation axis pointing away from the storage ring. In the case of the second crystal, the singly diffracted X-ray beam would be incident from the left and diffract from the ($\bar{1}\bar{1}\bar{1}$) Bragg planes, with the [1$\bar{1}$0] rotation axis pointing toward the storage ring, *i.e.* [$\bar{1}$10] points away in this case. The crystals are designed so that the (113) (first crystal) and ($\bar{1}\bar{1}\bar{3}$) (second crystal) Bragg planes (shown dashed) can also be utilized for higher X-ray energies.

The formalism developed by Erola *et al.* (1990) assumes that the crystal has isotropic elastic properties and so involves just a single value for Poisson's ratio.[24] However, Si is elastically quite anisotropic, with the isotropic average of ν usually taken to be 0.22 [this value can be obtained by averaging, assuming uniform strain, over the elastic constant values (C_{ij}) of Hall (1967), the so-called Voigt average (Voigt, 1928); 0.23 results if the average is taken, assuming uniform stress, over elastic compliance values (S_{ij}), the so-called Reuss average (Reuss, 1929); see Hill (1952)]. The experimental elastic constant data provided by Hall (1967) is for the (100) Bragg planes of Si. The recent work of Zhang *et al.* (2014) allows for the calculation of anisotropic elastic constant values for arbitrary crystallographic orientations. A means of calculating an effective isotropic ν-value as an average of two anisotropic values is also presented and this yields, for the IMBL DCLM Si crystals, a value of 0.18. An alternative approach to calculating an effective isotropic ν-value is *via* equation (2) of Schulze *et al.* (1998) [see also equation (5) of Schulze & Chapman (1995)]. It is closely related to (but not the same as) Erola *et al.* (1990) equation (3) and yields values of lattice-angle change which agree to within ∼0.2% for typical values of θ_B, χ and ν relevant to IMBL. The advantage of this equation is that it is applicable to the anisotropic case and could be used to provide an effective isotropic ν-value (0.14 here) of the form $-(S_{13} + S_{15}\cot\chi)/S_{11}$, provided that the S_{ij}-values relate to the particular crystallographic orientation concerned [we will,

[22] Si (111) monochromators used at X-ray absorption spectroscopy beamlines generally have an energy resolution ($\delta E/E$) of 2×10^{-4} or better, and so a bandpass of ∼5 eV at 25 keV. If we apply the full, anisotropic formalism developed later in this section, we calculate that the energy bandpass for one of our bent Si crystals, in the present case, is actually 14.6 eV for the fundamental component and 43.8 eV for the λ/3 harmonic. The respective (single-crystal) reflectivities are 0.492 and 0.195. The integrated reflectivities for the DCLM as a whole are then 1.76 and 0.832 eV, respectively.

[23] To be rigorous, the operational Bragg planes can be denoted (111) and ($\bar{1}\bar{1}\bar{1}$) for the first and second crystals, and the rotation axes (pointing away from the storage ring) [1$\bar{1}$0] and [$\bar{1}$10], respectively. Given that Si possesses a centrosymmetric crystal structure, such fine details are of little practical consequence however.

[24] ν must lie between the limits −1 and 0.5, the former associated with the requirement that the shear modulus is always positive and the latter that the bulk modulus is always positive.

however, use the full equation of Schulze & Chapman (1995) in our calculations]. In the isotropic case, $S_{13} = S_{12}$ and $S_{15} = 0$ and so ν reduces to its usual value of $-S_{12}/S_{11}$ [0.28 from the data of Hall (1967)], independent of χ. In order to calculate the values of S_{11}, S_{13} and S_{15} we followed the treatment of Wortman & Evans (1965) (see also Hearmon, 1961; Sanchez del Rio *et al.*, 2015) and obtained 0.00591, −0.000850 and 0 GPa^{-1}, respectively. As expected, these values are quite different from those derived from Hall (1967) data (0.00769, −0.00214 and 0 GPa^{-1}, respectively).

The integrated reflectivity for the DCLM as a whole is given by $R_1R_2\delta E_{min}/2$, where δE_{min} is the smaller of δE_1 and δE_2. This value is then multiplied by the value of IC current per eV calculated using *spec.exe*, including the filtration afforded by windows, a new FE diamond filter (see §4.4.2) and air/He paths. The results of such calculations can be used to provide, at a given (fundamental) X-ray energy, a breakdown of the measured ADC IC currents between the fundamental and harmonic components. If we choose to consider that contributions smaller than 0.25% are insignificant, then the λ/3 harmonic is only significant for our experimental energy values of 20 and 25 keV and the λ/4 harmonic for only 20 keV, *e.g.* the breakdown for the lowest energy value (20 keV) is 96.7%:3.0%:0.3% for the upstream ADC IC, and 94.8%:4.7%:0.4% for the downstream ADC IC, the latter case reflecting the 'hardening' of the multi-component beam as a result of its traverse through an extra 5.8 m of air and 6.7 m of He. Fig. 7 also includes the experimental data points after correcting for the harmonic contamination[25] and the corresponding fit curve[26]. We will use this fit curve up to 70 keV and NIST values at higher energies. This data analysis, without corrections for harmonic contamination, is independent of K_e. However, this is no longer true when the presence of harmonics is acknowledged due to the significant energy dependence of K_e and so we have included it here. It turns out that this effect is only significant for the 20 keV data. We will discuss electron-loss corrections at length in §4.3 and so here just mention that the values of K_e for 20, 60, 80 and 100 keV have been calculated (Monte Carlo) to be 1.01, 1.43, 1.23 and 1.12 for the ADC IC, respectively. This means that not including K_e would artificially increase the role of the harmonics and thereby overestimate the μ_m values (by ∼6% on average at 20 keV). Some measurements were also made for different degrees of bending of the DCLM crystals, including having them convex as viewed from the X-ray source [see, for example, Suortti & Schulze (1995) for detailed discussion of the different non-dispersive Laue crystal dispositions]. Observed variations in the derived μ_m values were relatively small.

Whilst the μ_m values for the two ADC ICs are generally quite close, at 20 keV the value for the downstream IC is significantly higher, especially after correction for harmonic contamination. We attribute this to more of the extraneous scattering from the carbon-based *in vacuo* filters being outside of the 'acceptance' area (solid angle) of the downstream IC. The horizontal opening of the ADC ICs is quite large (100 mm) but is only 10 mm vertically; so in the case of the downstream IC this represents an angle of approximately ±0.24 mrad subtended at the filters, compared with ±0.60 mrad for the upstream IC. This observation points to a comprehensive model of the influence of the carbon-based filters being quite complex since μ_m values can depend on the size, geometry and position of the X-ray beam cross-section (in solid-angle terms). The definition of the beam incident on the *in vacuo* filters, as well as any downstream restrictions of the beam, are important factors to be considered. In the present context the fact that the influence of this extraneous scatter is largely confined to relatively low X-ray energies justifies using our rather simplistic model. However, care needs to be taken, especially if the filtration being used is such that lower X-ray energies play a significant role. In order to demonstrate this point, the integrated flux values in Table 4 (last column) are reduced by 29.9, 15.3, 0.6 and 0.0% for F1 to F4, respectively, as a result of using the μ_m values from the fit curve just described, to allow for the extraneous scattering effects attributed to the carbon-based *in vacuo* filters.

Warren (1949) used a double-crystal spectrometer with Cu *Kα* X-rays to obtain measurements of the total power in the SAXS from a sample of carbon black. Whilst carbon black is often assumed to be amorphous, it is the result of pyrolysis and usually contains very small crystalline regions of graphite-like (or even diamond-like) carbon. Warren (1949) noted that '*the additional absorption caused by small-angle scattering is for this material more than twice the ordinary absorption*'. It was also possible to obtain, under certain assumptions, an estimate of the effective particle size. A radius value of 220 Å was obtained, consistent with earlier measurements (95–275 Å) of Biscoe & Warren (1942) for the same material. If we, rather simplistically, apply the same formulae to the 20 keV data shown in Fig. 7, an effective particle radius of 64 Å is obtained. Another particularly relevant study was that of Chipman (1955), who made measurements, also with a double-crystal spectrometer, of μ_m for carbon with Cu $K\alpha_1$ X-rays, for samples of graphite, polystyrene (C_8H_8) and paraffin (C_nH_{2n+2} in general) (with allowance made for the contribution of hydrogen for the last two). The graphite was described as '*high purity artificial graphite of density 1.70*' and so is (possibly) rather similar to that used at IMBL. The measurements were performed as a function of the detector-aperture width and this had virtually no effect for the polystyrene and paraffin, but there was a dramatic increase in the derived μ_m-value for graphite once the aperture width was decreased below ∼0.15°. Chipman (1955) points out that, unlike polystyrene and paraffin, graphite can '*give considerable small angle scattering*' and as the aperture width is decreased below a certain level this SAXS will be excluded and the derived μ_m-value (artifi-

[25] These corrections are based on using the NIST values of μ_m for the harmonic components (given that the lowest-energy harmonic to be considered is 60 keV) and solving for the value at the energy of the fundamental component.

[26] Fitting is based on varying the coefficients Λ_i in the equation $\mu_m = \Lambda_0 + \Lambda_1/E + \Lambda_2/E^2 + \Lambda_3/E^3$, for the experimental data between 20 and 70 keV inclusive. In this case we have used the average values of μ_m from the two ADC ICs, after correction for harmonic contamination.

Table 6
spec.exe calculation results for comparison with graphite-calorimeter measurements of Harty *et al.* (2014).

Since the flux values have been calculated for a 0.1 mm × 0.1 mm X-ray beam, the second last column could also be termed 1% of the photon fluence rate at the detector (photons s^{-1} mm^{-2}) and the last column the peak absorbed-dose rate to water (Gy s^{-1}).

Harty *et al.* (2014) Filtration	Maximum flux [photons s^{-1} (0.1% bandwidth)$^{-1}$]	Energy for maximum flux (keV)	FWHM (keV)	Weighted-average energy (keV)	Integrated flux (photons s^{-1})	Absorbed-dose rate to water (Gy s^{-1})
1	2.40×10^7	75.7	51.6	82.5	1.67×10^{10}	62.0
2	1.02×10^7	87.4	54.0	95.0	6.45×10^9	26.3

cially) increased. Chipman (1955) recommended a value of 4.15 cm^2 g^{-1}, some 20% lower than the largest value he measured, *i.e.* with the narrowest detector aperture. This value is significantly lower than the other values available to Chipman (1955) for comparison at that time: 4.52, 4.87 and 5.50 cm^2 g^{-1} from Compton & Allison (1955), Andrews (1938) and *Internationale Tabellen zur Bestimmung von Kristallstrukturen* (1935), respectively. The weight of the arguments presented has now diminished somewhat in light of the value from the NIST database being 4.49 cm^2 g^{-1}, and that from *International Tables for X-ray Crystallography* (1962) being 4.60 cm^2 g^{-1}. However, the nature and importance of the SAXS contribution to the μ_m-value associated with carbon-based filters is quite clear and well established.

4.2. Predicting absorbed-dose rates

In the paper by Crosbie *et al.* (2013) a low-energy free-air ionization chamber (LEFAC) from the Australian Radiation Protection and Nuclear Safety Agency (ARPANSA) was used for dosimetry measurements in IMBL hutch 1B. The LEFAC is a replica of the Australian primary-standard dosimeter for kilovoltage X-ray beams. The APS wiggler was in operation at this time and, if we use essentially the same experimental parameters as those detailed by Crosbie *et al.* (2013)[27], *spec.exe* yields first, second and third HVLs for Cu of 0.446, 0.531 and 0.622 mm, respectively, and a first HVL for water of 33.0 mm. The corresponding values from the LEFAC measurements were 0.405 (0.015), 0.516 (0.023) and 0.603 (0.018) mm for Cu and '*approximately 30 mm*' for water. All of the *spec.exe* results reported in this section were calculated with an X-ray energy range from 1 to 1000 keV (in 0.1 keV steps) and emittance effects are included. *spec.exe* predicts a maximum flux value of 2.60×10^9 photons s^{-1} (0.1% bandwidth)$^{-1}$ at 57.5 keV, FWHM of 27.4 keV, weighted-average energy of 60.5 keV and integrated flux of 1.29×10^{12} photons s^{-1}, in comparison with a '*mean energy*' of 61.4 keV from Crosbie *et al.* (2013) (see also their Fig. 1). Finally, the air-Kerma rate (actually surface absorbed-dose rate to air) from *spec.exe* is 75.3 Gy s^{-1}, compared with 63.8 (1.8) Gy s^{-1} measured with the LEFAC. We will discuss, below and in §5, the fact that the *spec.exe* value is some 18% higher. It should also be noted that the small beam used in this case ensures that the roll-off effects in the horizontal direction are insignificant. However, if we reduce the vertical height of the beam to 0.1 mm at 20.4 m, instead of 0.74 mm, the calculated air-Kerma rate becomes 78.2 Gy s^{-1}, the 4% increase being associated with roll-off effects in the vertical direction.

Harty *et al.* (2014) employed a graphite calorimeter in IMBL hutch 3B to measure the absolute absorbed-dose rate to graphite. The measure of absorbed dose derives from the increase in temperature which occurs in the graphite when irradiated, and this is then converted to peak absorbed-dose rate to graphite using careful measurements of the cross-sectional X-ray beam area and profile, for different beam sizes, using Gafchromic film exposures. Monte Carlo calculations were then used to convert to the peak absorbed-dose rate to water. The SCMPW was in operation at this time and if we use essentially the same experimental parameters as those detailed by Harty *et al.* (2014)[28], *spec.exe* yields the results in Table 6. These calculations have been performed for a 0.1 mm × 0.1 mm X-ray beam, at 138.2 m, so that no roll-off effects are present, and a direct comparison with the peak absorbed-dose rate to water values of Harty *et al.* (2014) can be made. Harty *et al.* (2014) state that the average energy for *Filtration 1* 'was about 80 keV', and for *Filtration 2* 'was about 90 keV', in accord with the results in Table 6. Their value of peak absorbed-dose rate to water for *Filtration 1*, determined from the calorimeter measurement for 1 mm depth in graphite, was 52.1 (1.4) Gy s^{-1}; the corresponding value in Table 6 is 19% higher. For *Filtration 2*, and 2 mm depth in graphite, the value obtained by Harty *et al.* (2014) was 20.4 (0.6) Gy s^{-1}; the Table 6 value is 29% higher. The *Filtration 1* air-Kerma rate from *spec.exe* is a factor of 1.076 smaller than the Table 6 value, in agreement with the factor in Table III of Harty *et al.* (2014); they also quote a back-scatter factor for water of 1.022 which *spec.exe* does not include [see also the AAPM TG-61

[27] 3.032 GeV, 200 mA, 20.4 m from the source, APS wiggler operating at 1.31 T, 0.5 mm × 0.5 mm beam at the *in vacuo* primary slits [see Table 1 and Fig. 1(*a*)], 74 mm He path, 1.0 m air path, 0.35 mm Be window, 38 µm Al foil, $2.5\sqrt{2}$ mm flexible graphite, $(0.2\sqrt{2} + 0.5\sqrt{3}/2)$ mm Al, $\sqrt{2}$ mm Cu. The last three filters are *in vacuo*; we have used an effective density of 1.7 g cm^{-3} for the flexible graphite, based on separate experiments, allowing for extraneous scattering, *e.g.* data recorded at the Australian Synchrotron's Powder Diffraction beamline with a Mythen micro-strip detector showed clear evidence of diffraction peaks, which could be indexed as 002, 004 and 006 graphite reflections based on a HOPG 002 interplanar spacing of 3.35 Å; the Al effective thickness arises from having 0.2 mm with filter angle 45° and 0.5 mm with 30°.

[28] 3.032 GeV, 200 mA, 138.2 m from the source, SCMPW operating at 3.00 T, 205 mm He path, 3.0 m air path, 2.7 mm Be window(s), 114 µm Al foil(s), 100 µm Kapton, $15.0\sqrt{2}$ mm flexible graphite (*in vacuo*). As above we have used an effective density of 1.7 g cm^{-3} for the flexible graphite. Additionally, for Harty *et al.* (2014) '*Filtration 1*', there is $1.5\sqrt{2}$ mm Al and $\sqrt{2}$ mm Cu *in vacuo*; whereas, for their '*Filtration 2*', there is $0.5\sqrt{2}$ mm Al and $2\sqrt{2}$ mm Cu *in vacuo*.

protocol; Ma *et al.* (2001)]. The observed absorbed-dose rate discrepancies will be discussed below and in §5.

We used a PTW Type 31014 PinPoint chamber (measuring volume 0.015 cm^3; Al electrode; operated at 400 V) in conjunction with a Type 10023 UNIDOS webline dosemeter/electrometer to measure the absorbed-dose rate to water as a function of *in vacuo* filtration (F3, F4 and F5), beam size (5 mm × 5 mm, 10 mm × 10 mm and 20 mm × 20 mm) and water depth (10 to 100 mm in 10 mm steps, plus 5 and 15 mm) in hutch 2B. These values have in turn been used to obtain the PDD data presented in Fig. 11. PDD values are referred to (that is, have as their denominator) the maximum dose (D_{max}) which, in general, does not occur at the water surface. The phenomenon of 'build-up', associated with the secondary electrons produced by X-ray photon interactions, competes with X-ray attenuation and can thereby result in D_{max} occurring some distance into the water. However, for the predominantly kilovoltage X-rays used at IMBL (rather than orthovoltage or megavoltage X-rays), a more subtle change to the exponential-like decrease associated with attenuation alone is observed, *i.e.* the near-surface region may exhibit a plateau region rather than a distinct peak, especially given the limited depth resolution for measurements involved here. We have thus used the dose at 5 mm water depth as the denominator for the experimental PDD data presented in Fig. 11, rather than perform an extrapolation with an exponential function, involving a concomitant overestimation of the surface dose. The calculated PDD curves from *spec.exe*[29], being based purely on attenuation, with no allowance made for build-up effects nor back-scatter contributions (see, for example, Grosswendt, 1990; Klevenhagen *et al.*, 1996; Hill *et al.*, 2014), show an exponential-like decrease with water depth. More realistic PDD values rely on Monte Carlo simulations, such as those of Zeinali-Rafsanjani *et al.* (2015). In order to be consistent with the experimental data, we have also referred the calculated PDD curves to the corresponding dose value at 5 mm water depth. In the case of the F4 *in vacuo* filter set, the differences between the calculated curves (for different beam sizes) are not discernible. The experimental and calculated PDD curves show reasonable agreement, considering the somewhat crude approximations made for the latter.

In order to make a comparison of absolute experimental and calculated absorbed-dose rates to water, rather than PDD values, we need to correct the PinPoint-chamber results for K_Q, K_{TP} and K_h; see (4) and IAEA (2000). K_{TP} is 1.019 for our measured values of $T = 23.4°C$[30] and $P = 100620$ Pa. Individual values of K_Q were determined from data provided in the PTB (Germany) calibration certificate for the different beam qualities, as specified by first HVLs for Al and Cu. The IMBL

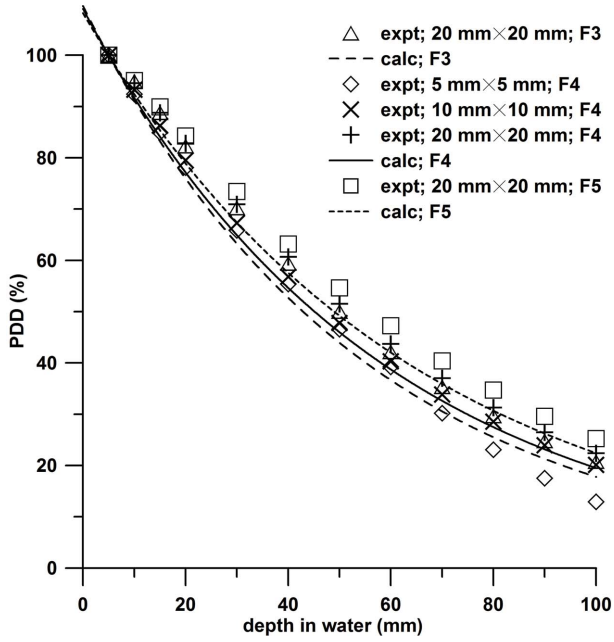

Figure 11
Experimental and calculated PDD curves in (liquid) water for different beam sizes and *in vacuo* filtration. The former were collected with a PTW Type 31014 PinPoint chamber in hutch 2B with a 2 mm-high (broad) X-ray beam in dynamic radiotherapy mode (motor speed 20 mm s^{-1}). The calculations were performed with *spec.exe* and involved step sizes of 25 µm and 0.1 keV (for 1 to 1000 keV). It has been assumed that D_{max} corresponds to a 5 mm water depth. See text for further details.

first HVLs are given in Table 5 and the resulting K_Q values varied only slightly, enabling us to use the average value of 0.950 (0.001) throughout. We found that the calculated dose rates were greater than the experimental dose rates for all five cases in Fig. 11, the average discrepancy being 26.0 (9.5)%. The discrepancy increased with increasing hardness of the beam (from F3 to F5) and with decreasing beam size (from 20 mm × 20 mm to 5 mm × 5 mm).

In this section we further demonstrated the utility, value and versatility of our model, as implemented in *spec.exe*, in relation to absorbed-dose rates. We have also seen that the model has its limitations, and, in particular, a consistent trend where the calculated dose rates are some 20 to 30% larger than experimental values is observed. Whilst the importance of programs such as *SPECTRA, XOP* and *spec.exe* has been demonstrated by researchers at synchrotron-radiation facilities around the world for many years, much of this usage relates to applications which are not reliant on absolute determinations of flux, fluence, dose and so on. In fact, literature surveys reveal a considerable paucity of synchrotron studies where such programs have been tested in an *absolute* sense. One of the few examples known to us is the study of a novel SPring-8 ID (a 'figure-8' undulator), by Tanaka *et al.* (2000). A gas-scattering method was used to measure absolute values of angular flux density (our terminology) as a function of undulator gap, and these were compared with calculations. Tanaka *et al.* (2000) state: '*As for the absolute value of the flux, the measured value is slightly smaller than the calculated one in each case. Typically, the difference is about 20%.*' They do not

[29] 3.032 GeV, 200 mA, 33.9 m from the source, SCMPW operating at 3.00 T, 6.7 m He path, 6.0 m air path, 0.7 mm Be window(s), 0.6 mm diamond filter (*in vacuo*), 76 µm Al foil(s), 225 µm Kapton, F4 (*in vacuo*; see also §4.1).
[30] The specification for temperature in the experimental hall at the Australian Synchrotron is 22 (1)°C at 4 m height above the floor. In the machine tunnels the 'steady-state' temperature is 24.0 (0.1)°C. The local temperature in beamline experimental hutches may, of course, vary considerably and is typically within the range 23.0–24.5°C at IMBL. The humidity at the facility is not controlled.

specifically account for the discrepancy but state that it is small enough to be attributed to experimental uncertainties in dimensions of apertures used and thicknesses of filters/windows, and the efficiency of the Ge solid-state detector used. It is interesting (and possibly fortuitous) that the discrepancy reported by Tanaka *et al.* (2000) is quite similar in size to that in the present work. Further work to identify the origin of these discrepancies would be opportune.

In order to put such discrepancies between calculated and experimental dose rates into context, we consider some recent comparisons between experimentally determined (synchrotron) dose rates obtained using different dosimeters. Lye *et al.* (2016) have used IMBL to make such a comparison between dose rates (surface absorbed-dose rates to water) measured with an ADC IC-105 IC (operating as a FAC), a PTW 31014 PinPoint chamber, a PTW 34001 Roos chamber, and a graphite calorimeter (Harty *et al.*, 2014). The FAC results were between 3 and 5% higher than for the calorimeter, the Roos results ∼2% higher, and the PinPoint results up to ∼2% lower. Donzelli *et al.* (2016) have reported air-Kerma measurements made at ID17 (ESRF) with a PTW 31010 Semiflex chamber and a Radcal 10X6-6 chamber, the results from the former being typically ∼15% higher. Such results are indeed impressive, but do help to put the above-mentioned discrepancy with our model into perspective.

4.3. 'Rotating-filter' method and electron-loss effects (K_e)

The utility of collecting transmission data for a rotating filter in the case of a monochromatic X-ray beam, albeit with harmonic contamination (see Fig. 8), has already been demonstrated. This technique can also be used with a polychromatic X-ray beam as an extension of standard HVL measurements (which are discussed in more detail in §4.4.2). In this section, we will describe and demonstrate the power of the method in verifying one of the critical parameter values in our model, namely the magnetic field strength in the wiggler.

We have already foreshadowed the need to carefully consider the roles of electron-loss effects (K_e) and recombination (K_s) for our free-air, parallel-plate ICs since these are the most significant IC correction factors of concern in this study (see §3.4). The two are linked inasmuch as recombination effects can in general be lessened by reducing the plate separation in the IC (thereby increasing the field strength), but this will serve to increase the severity of electron-loss effects. Such design considerations can, of course, also impact other aspects of IC operation [see, for example, the early work of Failla (1929) in respect of field distortions]. In the case of the ADC IC used here, K_e has a strong energy dependence with a local maximum at ∼50 keV and a local minimum at ∼100 keV, followed by a rapid increase. This is important in the context of IMBL, especially for radiotherapy, where the higher-energy X-rays play a significant role, *e.g.* see the column of weighted-average X-ray energies in Table 4. Grimbergen *et al.* (1998) provide a comprehensive discussion of the energy dependence of K_e and the '*competing effects: increase of the range of the photo-electrons and decrease of the relative number of photoelectric interactions compared to Compton interactions*'.

Electron loss occurs when the IC plate separation is not sufficient to ensure that all secondary electrons produced by interactions within the air which constitutes the defined irradiated chamber volume (V_c) are able to deposit all of their kinetic energy (see, for example, Kemp & Hall, 1954; Attix & DeLaVergne, 1954), *i.e.* these, usually more energetic, electrons are able to reach the IC electrodes or walls. One of us (JEL) has used the *BEAMnrc* (based on the *EGSnrc*) Monte Carlo code for radiation transport (Rogers *et al.*, 1995) to model the electron-loss effects as a function of X-ray energy for the ADC IC (see Lye *et al.*, 2010). Linear-polarization effects are not incorporated into this model (see §3.4). The lower thresholds for electron and photon energies were set to 512 and 1 keV, respectively. K_e is calculated, at each value of E, as a ratio whose numerator is the energy deposited in V_c plus the air outside of V_c plus the electrodes and chamber walls, by secondary electrons (and their progeny) produced in the first interaction with a primary X-ray photon; the denominator is the energy so deposited in V_c alone (see Kurosawa & Takata, 2005[31]). Some investigation of the dependence of K_e on the X-ray beam cross section was undertaken and found not to be significant for the present work.

Whilst the calculated values of $K_e(E)$ will be applied to individual energy components prior to any integration, it will prove useful to have a single measure of the electron-loss effects for a given polychromatic X-ray beam. This could, for example, take the form of the appropriate spectrally weighted average (Grimbergen *et al.*, 1998; Lin & Chu, 2006) or the value of $K_e(E)$ for the weighted-average X-ray energy. However, for our purposes, a more practical definition is the ratio of the (calculated) integrated IC currents without (numerator) and with (denominator) allowance for electron-loss effects, $K_{e,\mathrm{eff}}$.

In this section we will rely on the fact that, whilst (volume) ion recombination (K_s) is critically dependent on IC geometry and operating conditions (in particular plate separation D and applied high voltage V, respectively), in addition to the rate at which charge is liberated within the chamber volume[32], ion recombination is essentially independent of beam quality[33]. This important point will be demonstrated in §4.4, in the context of a detailed discussion of absolute IC measurements, and has been a key finding of various other studies, such as that by Bruggmoser *et al.* (2007). It affords us a valuable means of further testing our model, as implemented in

[31] Note that we refer to K_e as being for the mono-energetic case, *i.e.* explicitly, $K_e(E)$. Also note that there is a typographical error(s) in Kurosawa & Takata (2005) in that their equation (2) is actually for K_{sc} and their equation (3) is for K_e.

[32] Strictly speaking, we use the charge liberated within the chamber volume, *as corrected for electron-loss effects*.

[33] Burns & Büermann (2009), for example, have stated that '*ion recombination and diffusion effects do not depend measurably on the X-ray spectrum. A further consequence of this is that K_s does not need to be measured separately for each X-ray spectrum. The same equation for K_s as a function of ionization current can be used for all X-ray qualities.*'

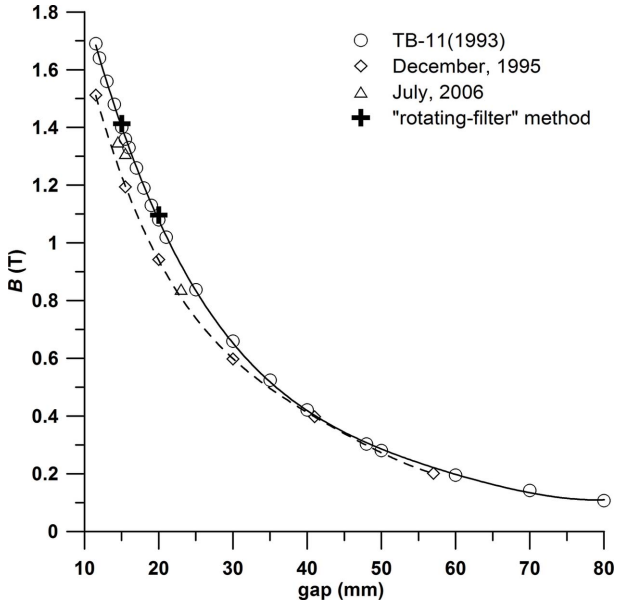

Figure 12
Wiggler field as a function of permanent-magnet gap for the APS A wiggler. Data from several places are presented. See text for further details.

spec.exe, independent of the difficulties associated with accurately determining K_s.

4.3.1. APS A wiggler. Fig. 12 provides a plot of the wiggler field as a function of permanent-magnet gap for the APS A wiggler. These results are taken from several places: an APS technical bulletin (TB-11; Lai *et al.*, 1993) on general specifications and characteristics for this type of wiggler; measurements collected (December 1995) for a different wiggler (No. 23) of the same type; measurements collected (July 2006) specifically for the IMBL wiggler (No. 24) prior to shipping to Australia. Precise measurements of the physical wiggler gap were performed *in situ* and found to agree extremely well with the nominal values. The presence of the evacuated electron-beam tube (Al; approximately 13 mm outer dimension vertically; wall thickness approximately 1 mm) precluded making *in situ* Hall-probe measurements of the on-axis (central) magnetic field, but off-axis measurements (with an accuracy of ∼5%) collected with a 16.5 mm wiggler gap were shown, by applying the appropriate equations (Maxwell, 1865), to at least be consistent with the nominal (on-axis) value.

Fig. 13(*a*) shows experimental results obtained with the APS A wiggler being operated with 15 and 20 mm gaps.[34] Additional *ex vacuo* filtration was provided by fixed 2 mm-thick Cu at 33.1 m and a rotatable filter at 33.6 m. The latter involved 4.5 mm Al (F1′), 0.25 mm Cu (F2′), 0.105 mm Mo (F3′) or 50 µm Au (F4′), in between 0.5 mm Al sheets, *e.g.* F1′ was 5.5 mm Al in total. All of these filters were of high quality/purity (Al and Cu, Gammex 115 A and 116 HVL attenuator

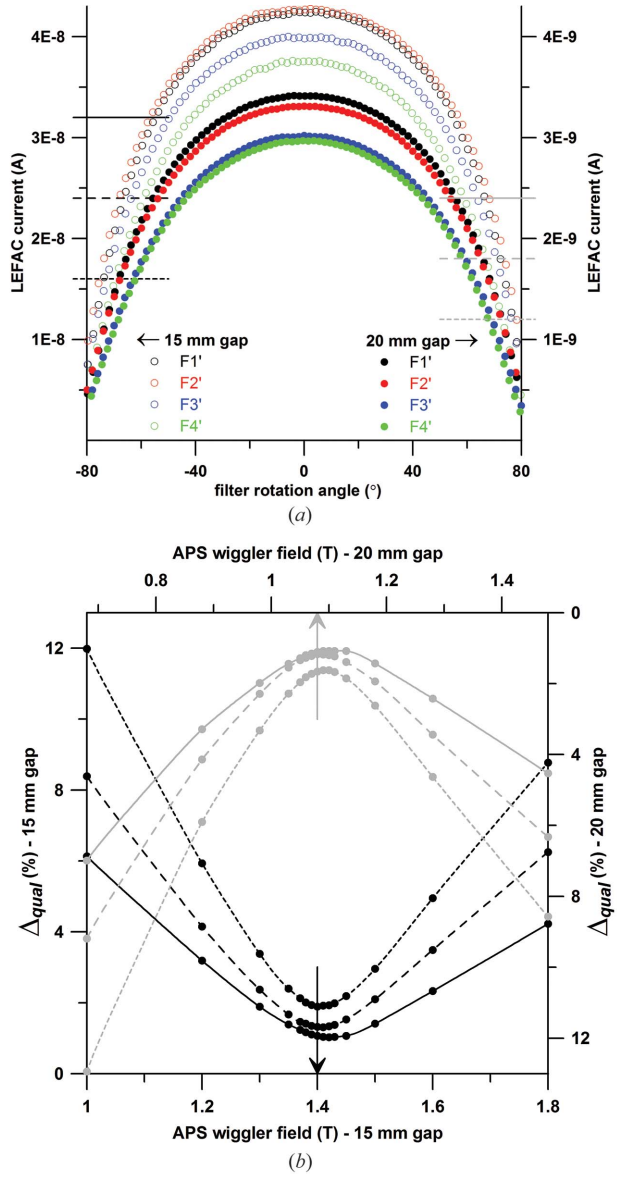

Figure 13
(*a*). Experimental LEFAC currents for the 'rotating-filter' method, using the APS A wiggler (with 15 and 20 mm gaps). Four different *ex vacuo* filter combinations have been used and rotated over the range ±80°: F1′, 4.5 mm Al; F2′, 0.25 mm Cu; F3′, 0.105 mm Mo; F4′, 50 µm Au; all in between 0.5 mm Al sheets. The three short horizontal lines for each wiggler gap mark the values of IC current used in the subsequent analysis. (*b*). Results of the analysis of data in (*a*). Δ_{qual} is the standard deviation (%) for the average of the four calculated IC currents (for F1′ to F4′). Each curve corresponds to one of the horizontal lines in (*a*). The *spec.exe* calculations were performed with X-ray energies from 1 to 1000 keV in 0.1 keV steps; 20 µm steps across the extent of the beam (horizontally and vertically); include emittance effects. The two vertical arrows indicate the wiggler-field values from TB-11. See text for further details.

sets; Mo, Advent Research Materials Ltd and Goodfellow Cambridge Ltd, 99.9% purity or better, temper annealed; Au, Advent Research Materials Ltd, 99.99% purity, temper as rolled). Each of the four filter combinations was rotated over a range of ±80° in 2° steps, after ensuring that the 0° position corresponded to the filters being (accurately) normal to the X-ray beam. The LEFAC (located at 34.3 m from the source;

[34] 3.032 GeV, 200 mA (top-up mode), pink beam, hutch 2B, 0.6 mm diamond window (in FE and actually a window, rather than the filter mentioned elsewhere), 7.0 m He path, 6.9 m air path, 0.35 mm Be window, 38 µm Al foil, 200 µm Kapton, 2 mm Cu, $2.5\sqrt{2}$ mm flexible graphite (*in vacuo*), $1.2\sqrt{2}$ mm Al (*in vacuo*), T = 23.0 (0.4)°C, P = 101100 (300) Pa.

operated with V = 3.00 kV) was used to record IC current. The LEFAC has L = 1.9985 cm and D = 6.0 cm, providing smaller electron-loss effects but significantly larger recombination effects, in general, in comparison with the ADC IC (the higher operating voltage for the LEFAC does help reduce recombination to some extent, but the much larger plate separation is the dominant contributing factor; see §4.4.1). To illustrate this point, the calculated value of $K_{e,eff}$ for the case of the 15 mm gap, F2′ and rotation angle of 0°, is 1.08, whereas the value for the ADC IC (with V = 2.00 V) is 1.33. The data shown in Fig. 13(*a*) have not been processed in any way except for scaling each IC current to a ring-current value of 200.3 mA. Three representative IC-current values were selected for each wiggler gap, as indicated by the short horizontal lines. Each of these, after linear interpolation between the relevant adjacent filter rotation-angle values, provides us with four different X-ray beam qualities, based on *ex vacuo* filter sets F1′ to F4′, which all yield the same experimental IC-current value. The largest variation in beam quality occurs at the smallest IC-current value for each wiggler gap (see below). TB-11 provides wiggler-field values of 1.40 and 1.08 T for the 15 and 20 mm gaps, respectively. Assuming, for the present, that these values apply, the (calculated) weighted-average X-ray energy varies from 68.9 (F4′) to 74.5 keV (F3′), and the first HVL for Cu from 0.650 (F4′) to 0.776 mm (F3′), for the case of 16 nA IC current and 15 mm gap. The weighted-average X-ray energy varies from 64.8 (F1′) to 67.7 keV (F3′), and the first HVL for Cu from 0.549 (F1′) to 0.616 mm (F3′), for the case of 1.2 nA IC current and 20 mm gap. The average value of the four weighted-average energies is 71.9 keV ± 3.7%, 70.4 keV ± 2.6% and 69.3 keV ± 1.9% for IC currents of 16, 24 and 32 nA (15 mm gap), respectively. The corresponding values of the first HVL for Cu are 0.715 mm ± 8.7%, 0.673 mm ± 6.2% and 0.645 mm ± 4.5%, respectively. The average value of the four weighted-average energies is 66.2 keV ± 2.3%, 64.9 keV ± 1.7% and 64.0 keV ± 1.2% for IC currents of 1.2, 1.8 and 2.4 nA (20 mm gap), respectively. The corresponding values of the first HVL for Cu are 0.584 mm ± 5.7%, 0.554 mm ± 4.2% and 0.533 mm ± 3.0%, respectively.

Fig. 13(*b*) provides the results from the analysis of the data in Fig. 13(*a*). We have used *spec.exe* to obtain the standard deviation (Δ_{qual}) for the average of the four calculated IC currents (for F1′ to F4′), as a function of wiggler field, in each case. The vertical arrows indicate the wiggler-field values from TB-11. A quadratic fit to each curve, for a range of approximately ±0.1 T about the minimum Δ_{qual} value, was used to obtain a value for the wiggler field. The average of the three such values was 1.413 (0.009) and 1.096 (0.008) T for the 15 and 20 mm gaps, respectively. These values are shown in Fig. 12 and are in excellent agreement with the TB-11 values. We would expect the most significant differences in spectra for the different beam qualities to occur at higher X-ray energies. This, coupled with the observation above that the largest variation in beam quality occurs at the smallest IC-current values, suggests that the rotating-filter method should provide better sensitivity to wiggler field when the level of filtration employed is greater. This is indeed the case as we see the curves in Fig. 13(*b*) are less peaked as we go toward larger LEFAC current.

4.3.2. SCMPW. We have also applied the rotating-filter method to data obtained with the SCMPW. A more detailed set of results will be presented elsewhere for a range of wiggler fields. As an example, we have used an ADC IC (V = 2.00 kV; D = 1.425 cm; L = 5.0 cm) at 23.4 m from the source (hutch 1B) with the nominal wiggler field set to 2.20 (0.05) T. The relevant experimental conditions included: 3.033 GeV, 200 mA (top-up mode); F1, plus $\sqrt{2}$ mm Al, *in vacuo* filter set; fixed filters consisted of 73 mm He path, 0.35 mm Be window, 38 µm Al foil and 3.0 m air path (there was no *in vacuo* diamond); P = 101000 Pa and T = 24.4°C. The data were collected using the same *ex vacuo* filter sets F1′ to F4′, with the three selected IC currents being much larger this time (2.5, 3.5 and 4.5 µA). The final value we determined for the wiggler field was 2.19 (0.05) T, in excellent agreement with the nominal value.

The (calculated) weighted-average X-ray energy varies from 59.6 (F1′) to 65.3 keV (F3′), and the first HVL for Cu from 0.392 (F1′) to 0.508 mm (F3′), for the case of 2.5 µA IC current. The average value of the four weighted-average energies is 62.5 keV ± 4.5%, 59.4 keV ± 3.3% and 57.0 keV ± 2.7% for IC currents of 2.5, 3.5 and 4.5 µA, respectively. The corresponding values of the first HVL for Cu are 0.455 mm ± 11.9%, 0.391 mm ± 9.0% and 0.348 mm ± 7.5%, respectively.

4.4. Absolute IC measurements and ion recombination (K_s)

4.4.1. Theory. We will start by discussing the remaining and often most significant factor (for IMBL) in (4); the recombination correction K_s. The standard current *versus* voltage curve for an IC is characterized by quite distinct regions (voltage ranges) of operation including 'continuous discharge' at the highest voltages, then 'Geiger-Müller' at lower voltage, followed by 'limited proportionality', 'proportional counting' and, at still lower voltage, 'saturation'. It is in this latter region, characterized by a plateau of essentially constant current and with operating voltages of just a few kV, which we wish to operate. The ADC IC-105 cannot be operated above 2.00 kV (ideally 1.70 kV) and, if this is not high enough to attain saturation, opposite charges will recombine prior to collection. The collection efficiency f is given by $f = 1/K_s = I/I_{sat}$, with the 'near-saturation' region often defined as being for $f > 0.98$. In fact, we can have:

(i) General (or volume) recombination, an inter-track effect, where opposite charges from different tracks collide and recombine.

(ii) Initial (or columnar) recombination, involving the same process except that the colliding charges are from the same track, *i.e.* an intra-track effect.

(iii) Geminate (or preferential) recombination, involving recapture of an electron, or the negative ion of which it has become part, by its parent positive ion.

(iv) Ion-diffusion loss, where charges diffuse against the prevailing electric field.

Initial recombination is in general independent of dose or dose rate, whereas the opposite is true of general recombination (see, for example, Burns & Rosser, 1990). Given that we operate our free-air, parallel-plate ICs with reasonably high electric field strength ($E_{fs} = V/D$, for operating voltage V and plate separation D; typically $\sim$1 kV cm^{-1} here) and air at atmospheric pressure, initial recombination can usually be neglected in our case [the correction factor (to K_s) is given by $1 + E_1/E_{fs} = 1.00004$, for the constant $E_1 = 0.044$ V cm^{-1}, V = 2 kV and D = 2 cm; see Kara-Michailova & Lea, 1940; Böhm, 1976]. Geminate recombination (see, for example, early work by Harper, 1933; Onsager, 1938; Bradbury, 1940), can similarly be neglected here. Finally, ion-diffusion loss is also negligible in general, in the present case [diffusion-loss correction factor (to K_s) is given by $1 + 2k_BT/(VQ) = 1.00003$, for $T = 20$°C and V = 2 kV; see Langevin (1913)].

Use is often made, when operating near saturation, of the approximate relationship $1/I \approx 1/I_{sat}$ + constant/V^2 for general recombination ($1/I \approx 1/I_{sat}$ + constant/V for initial recombination; see Jaffé, 1913; Burns & Burns, 1993). The values of I and V under normal operating conditions and at a second, lower, voltage are used to obtain a value of K_s *via* the so-called 'two-voltage method'; see Almond (1981).[35] More sophisticated approaches and fitting procedures can also be applied when more extensive input data are available; see, for example, Andersson *et al.* (2012).

Considerable attention has been paid to developing theoretical expressions for f (or K_s) in the case of electronegative gases such as air, where a free electron resulting from ionization can subsequently become attached to a neutral gas atom to produce a negative ion. The drift velocity of such negative ions is $\sim 10^3$ times smaller than for (much less massive) free electrons, making it much more difficult to achieve IC saturation compared with the case of a non-electronegative gas. Boag & Wilson (1952), using a simple physical model, obtained the approximate result for a parallel-plate IC, assuming an electronegative gas (and continuous radiation and constant dose rate):

$$f = 2/\left[1 + \left(1 + 2\xi^2/3\right)^{1/2}\right], \tag{6}$$

where

$$\xi = \left(\frac{\alpha}{Qk_+k_-}\right)^{1/2} \frac{D^2\sqrt{q}}{V}. \tag{7}$$

The dimensionless parameter ξ, which is dependent on IC geometry, will be discussed in detail later; α is the recombination coefficient (see, for example, Jaffé, 1940), k_+ and k_- are the mobilities of the positive and negative ions, respectively, and q represents the charge liberated in the IC per unit volume, per unit time. Drift velocities are given by $d_+ = k_+E_{fs}$ and $d_- = k_-E_{fs}$ in the respective cases. The limit behaviour of (6) is such that $f \rightarrow 1 - \xi^2/6$ as $\xi \rightarrow 0$.

The derivation of (6) does not make allowance for space-charge effects and these are likely to be quite significant in the context of the present study. Such effects can distort the electric field, thereby affecting the collection efficiency of the IC. The original differential equations describing the transport of charge in a continuously irradiated, gas-filled, parallel-plate IC, including space-charge effects, date back to Thomson (1899) (see also Thomson & Rutherford, 1896; Thomson & Thomson, 1928). Unfortunately, these equations cannot be solved analytically and various authors have therefore obtained numerical solutions for specific applications, *e.g.* Novković *et al.* (1998) and Armstrong & Tate (1965). In the seminal paper by Mie (1904), approximate current–voltage relations were provided for two limiting cases, which can be written as

$$\left(\frac{f}{1-f}\right)^{1/2}\left[1 - \frac{4-\beta}{10}(1-f)\right] = \frac{\sqrt{6}}{\xi} \tag{8}$$

for $f \gtrsim 0.6$ (see, also, Seemann, 1912) and

$$f(1 + C_1 f) = \frac{k_+ + k_-}{\xi\sqrt{k_+k_-}} \tag{9}$$

for $f \lesssim 0.6$, where C_1 is a function of the dimensionless quantity β (as discussed below):

$$\beta = \left[\frac{Q\left(k_+ + k_-\right)}{\alpha\,\varepsilon_0}\right], \tag{10}$$

ε_0 being the free-space permittivity. Whilst the values of fundamental constants Q and ε_0 are very accurately known, there is considerable variability in the literature in respect of values for α, k_+ and k_-. Greening (1964) performed an extensive survey of experimental values of the quantity $[\alpha/(Q\,k_+k_-)]^{1/2}$ under STP (or near-STP) conditions[36] and obtained the value $(2.01 \pm 0.12) \times 10^7$ s$^{1/2}$ V m$^{-1/2}$ C$^{-1/2}$, in excellent, and probably somewhat fortuitous, agreement with theoretical values of Mie (1904), Scott & Greening (1961) and Ritz & Attix (1962); see also Boag (1987). McGowan (1965) and Boutillon (1998) have both found that the value of this quantity has little or no dependence on X-ray energy/beam quality[37]. In obtaining their numerical solutions, Armstrong & Tate (1965) have relied on $(k_+ - k_-)/(k_+ + k_-)$ having the value -0.163, this being based on data from Bradbury (1932). Finally, a well accepted value of α is 1.66×10^{-12} m^3 s^{-1} (Aglincev, 1957), and using this value together with the above two conditions for the ion mobilities yields $k_+ = 1.36 \times 10^{-4}$ m^2 s^{-1} V^{-1} and $k_- = 1.89 \times 10^{-4}$ m^2 s^{-1} V^{-1}. There is a measure of internal consistency in that the values provided by Aglincev (1957) (not used here) were 1.37×10^{-4} and 1.87×10^{-4} m^2 s^{-1} V^{-1}, respectively. We thus obtain a value for β

[35] Almond (1981) described the two-voltage method and demonstrated its use with a Victoreen electrometer, by selecting a second voltage which was 40% of the standard operating voltage. It should be noted that his crucial equation (5) has two typographical errors: the V in the denominator of the first factor should be V_2, and the second factor should be divided into, not multiplied by, the first factor.

[36] We should point out in respect of this quantity that we have made allowance for an error in the original paper; see the subsequent discussion of Katoh & Greening (1965) and Greening (1965).

[37] Boutillon (1998) also made a very careful experimental determination of this quantity, obtaining a value of $(1.99 \pm 0.02) \times 10^7$ s$^{1/2}$ V m$^{-1/2}$ C$^{-1/2}$, in excellent agreement with the value from Greening (1964).

from (10) of 3.54. This means that the second term in the square brackets in (8) has a maximum value of just 0.02 (for $f \gtrsim 0.6$) and so neglecting it is not unreasonable and one then obtains

$$f = 1/\left(1 + \xi^2/6\right). \quad (11)$$

In the present case, the f-value calculated with (11) will be slightly lower than that calculated with (8). It should be noted that the range of validity of (11) is generally accepted as being $f > 0.7$ (see, for example, Armstrong & Tate, 1965) and it has the same limit behaviour as (6) inasmuch as $f \rightarrow 1 - \xi^2/6$ as $\xi \rightarrow 0$.

If one chooses not to neglect the term containing β in (8)[38], a cubic equation for f results. For $\xi = 0$ we have the trivial solution $f = 1$, and for $\xi > 0$ the cubic equation has a discriminant,

$$\Delta = 12C^2\xi^2\left[2(C-1)^3\xi^4 + 3(C^2 - 20C - 8)\xi^2 - 72\right], \quad (12)$$

where $C = (4 - \beta)/10$. For all practical values of C which we need to consider, $\Delta < 0$ and so there will only be one real solution (the other two being complex conjugates and non-real),

$$f = \left\{\left[(C-1)^2\xi^2 - 18\right]/\tau + 2(C-1)\xi + \tau\right\}/(3C\xi), \quad (13)$$

where

$$\tau = \left[-(C-1)^3\xi^3 + 27(C+2)\xi + 3\sqrt{-3\Delta}/(2C\xi)\right]^{1/3}. \quad (14)$$

The other current–voltage relation [(9)] involves a quadratic equation for f, with the only physically reasonable solution being

$$f = \left\{-1 + \left[1 + 4C_1\left(k_+ + k_-\right)/\left(\xi\sqrt{k_+k_-}\right)\right]^{1/2}\right\}/(2C_1). \quad (15)$$

If f is suitably small (ξ large), (15) simplifies to $f \approx (k_+ + k_-)/(\xi\sqrt{k_+k_-})$, and further to $f \approx 2/\xi$ if $k_+ \approx k_-$. It only remains to establish the value C_1 which is dependent on β as already mentioned. Performing a cubic fit to the 'Computer' data in Table 3 of Armstrong & Tate (1965) yields $C_1 = 0.990$.

Fig. 14 provides a summary of these recombination results by showing f as a function of ξ, on a log–log plot, for (6), (13) and (15), *i.e.* the Boag & Wilson (1952) result, and our results based on the theory of Mie (1904) for $f \gtrsim 0.6$ and $f \lesssim 0.6$, respectively. For convenience, K_s values can also be obtained by referring to the axis on the right-hand-side. The results of (6) start to diverge quite significantly from those of (13) for $f < 0.8$; to be more specific, when $f = 0.9$ for (6) the discrepancy (in f) is 1.0%, when $f = 0.8$ the discrepancy is 4.4%, and when $f = 0.7$ the discrepancy is 10.8%. The results of (15) are always larger than those of (13), *i.e.* the two curves never cross. The value of ξ at which the percentage-difference between f values is a minimum (2.7%) is 1.90, these f values being 0.632 and 0.649 for (13) and (15), respectively, in accord with the above-mentioned nominal value for the transition from one formula to the other (0.6). In order to specify a 'composite' curve for f (or K_s) over the entire range of ξ, we use (13) for $\xi \leq 1.5$, (15) for $\xi \geq 2.5$, and a quadratic fit[39] for $1.5 \leq \xi \leq 2.5$. The magnified insert in Fig. 14 shows the critical region and the thick grey line is a section of the composite curve. The individual data points shown on the main graph correspond to numerical solutions obtained by Novković *et al.* (1998) and Armstrong & Tate (1965). These are in excellent agreement with our composite curve.

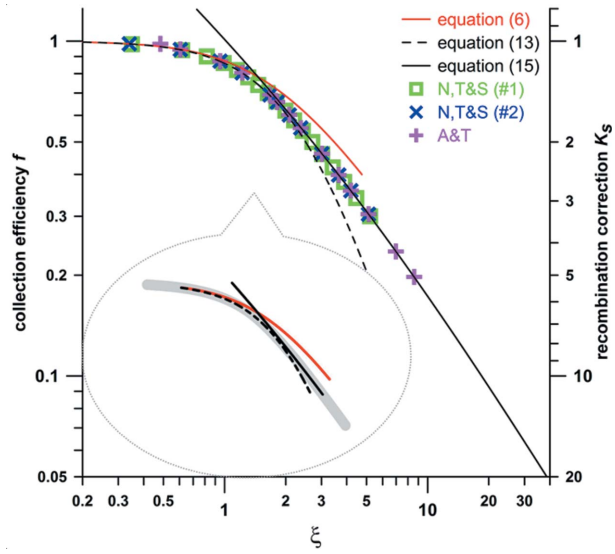

Figure 14
Calculated recombination results from (6), (13) and (15). Both f and K_s as a function of ξ are presented. The magnified insert shows the critical region in greater detail, with the thick grey line being a section of the 'composite' curve. The individual data points shown on the main graph correspond to numerical solutions obtained by Novković *et al.* (1998) and Armstrong & Tate (1965). 'N,T&S (#1)' refers to data from Table 3 of Novković *et al.* (1998); 'N,T&S (#2)' refers to data from Table 6 of Novković *et al.* (1998), with their values of 'τ/T' being equivalent to $1.014/\xi$ when our values of k_+ and k_- are used; 'A&T' refers to data from Table 2 of Armstrong & Tate (1965), with their values of 'τ/T ' being treated in the same way. See text for further details.

The treatment developed in this section is quite general in that it can be applied to various ICs such as those with cylindrical and spherical geometries, providing that the expression for ξ is modified accordingly (*e.g.* Boag, 1987). The expression for ξ given in (7) is appropriate to a conventional parallel-plate IC, where the X-ray beam is perpendicular to the plates. Some consideration of the theory for a FAC has been given by Scott & Greening (1961) and Boag (1969). Nariyama (2006, 2007) has also presented synchrotron-specific studies. In the case of a FAC, with the geometry described above, the appropriate formula in our terminology is

[38] This may be on the grounds of accuracy, and, if the IC is used with windows and other electronegative gases such as H_2 or Xe, β may well have a significantly different value from 3.54, *e.g.* ion mobilities for H_2 have been estimated to be almost an order of magnitude larger than those for air (*e.g.* Mason & Vanderslice, 1959). Andersson (2013) has derived a more accurate approximation to (8) than (11): this was motivated by his consideration of ICs employing non-polar dielectric liquids (with $\beta = 1$) as the medium, instead of air.

[39] Based on the f-value from (13) for $\xi = 1.5$, the average of the f-values from (13) and (15) for $\xi = 2.0$, and the f-value from (15) for $\xi = 2.5$.

$$\xi = \left(\frac{3\alpha}{\pi Qk_+k_-}\right)^{1/2} \frac{D(Sq)^{1/2}}{V}$$
$$= \left(\frac{3\alpha}{\pi Qk_+k_-}\right)^{1/2} \frac{1}{E_{\rm fs}} \left(\frac{I_{\rm sat}}{L}\right)^{1/2}. \quad (16)$$

4.4.2. Experiment. In this section we will present results of very recent experiments performed in IMBL hutch 3B with the aim of characterizing the performance of our ADC ICs with a polychromatic X-ray beam. The ring energy was 3.033 GeV, SCMPW field 3.00 (0.05) T and 'decay' (rather than the usual top-up; see §2) mode of operation was used. The recent FE upgrade (January 2015; see §3.2) included the installation of a 0.6 mm-thick diamond filter; other *in vacuo* filtration used consisted, initially, of the F2 filter set (see Fig. 4) minus the $2\sqrt{2}$ mm Al (we will refer to this combination as the F1 *in vacuo* filter set). *Ex vacuo* filtration (Be windows, He and air paths, Al foils) up to and including the Be window at 135.8 m from the source are as detailed in Table 1. The ADC IC was positioned at 138.2 m from the source, thereby contributing a further 2.3 m air path. It was read out *via* a Keithley 6487 picoammeter and operated with V = 2.00 kV and D = 1.425 cm, *i.e.* $E_{\rm fs}$ = 1.40 kV cm^{-1}. The air pressure and temperature were P = 100500 (300) Pa and T = 22.2 (0.1)°C.

Some of the results presented here were collected during special low-current periods and so it is important to establish the offset current (see §2). A circular aperture with 5 mm diameter (in 4 mm-thick high-density W-alloy), mounted on a multi-axis stage for alignment/orientation purposes, was located at 137.6 m, *i.e.* 0.6 m upstream of the ADC IC. The proximity of this aperture to the ADC IC ensures that any issues associated with penumbral blurring are insignificant, even horizontally, where the source size is largest; see, for example, Stevenson *et al.* (2012). However, it is still far enough away to avoid complications associated with extraneous scatter. Fig. 15 shows data collected for 15 different ring currents from 45 µA to 200 mA. The linear fit to the lowest of the ring-current values yields an offset-current value of 35 (3) µA; see the intercept of the short grey dashed line with the abscissa axis. The increasing discrepancy between the linear fit (taken to be experimental $I_{\rm sat}$ values) and experimental data points, with increasing ring current, is associated with recombination; see also the recent work by Fournier *et al.* (2016). The calculated $I_{\rm sat}$ values (black solid line) show reasonable agreement with those based on extrapolation from low-current experimental values. The calculated IC current values (*spec.exe*; see the formulae provided in §3.4) with allowance made for both electron-loss ($K_{\rm e}$) and recombination ($K_{\rm s}$) effects show much-improved agreement with the experimental values, relative to the (uncorrected) linear fit, although it appears that recombination effects are being somewhat overestimated. The calculated $K_{\rm s}$ values have been obtained *via* the 'composite' curve derived in §4.4.1; the maximum value of $K_{\rm s}$ was 2.42 (at a ring current of 200 mA), which represents an extremely large recombination correction. When recombination effects are negligible (or at least quite small) we expect the ADC IC current to be directly proportional to the ring current, as seen in all cases in Fig. 15, at small ring currents. If the recombination effects are large (as at large ring currents), we have $K_{\rm s} \propto \xi$ (see §4.4.1 and Fig. 14), and the ADC IC current should be directly proportional to the square root of the ring current. This is in accord with the experimental data and results of the full calculation (including both $K_{\rm e}$ and $K_{\rm s}$) in Fig. 15, with a smooth transition from one functional dependence to the other. The value of $K_{\rm e,eff}$ was 1.23, consistent with the modest filtration employed in this case, *i.e.* a high-integrated-flux and quite 'soft' X-ray beam (weighted-average X-ray energy of just 39.3 keV).

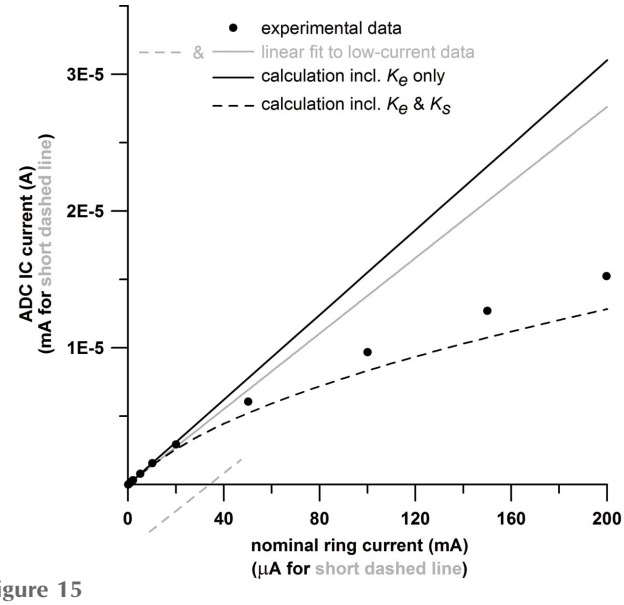

Figure 15
Plot of experimental ADC IC current values as a function of nominal ring current (black dots). The grey solid line represents a linear fit to the experimental data points with the smallest nominal ring-current values. The short grey dashed line is the same linear fit but has been plotted on a scale where both axes have been 'magnified' by a factor of 1000. The black solid line shows the results of calculations performed with *spec.exe*, including IC electron-loss, but not recombination effects. Finally, the black dashed curve is the result of full *spec.exe* calculations, including both $K_{\rm e}$ and $K_{\rm s}$. Calculations were performed for X-ray energies from 1 to 1000 keV in 0.1 keV steps, and 20 µm steps across the beam. See text for further details.

Various tests for the ADC IC were performed including:

(i) Swapping with another, identical, IC to check on reproducibility; agreement was within 2%.

(ii) Changing the polarity of the operating voltage V; agreement was within 0.4% for the usual +2 kV to −2 kV (see also discussion of $K_{\rm pol}$ in §3.4).

(iii) Changing the plate separation D from the usual value of 1.425 cm; in the context of the measurement shown in Fig. 15 for a ring current of 200 mA, the ADC IC current increases by 43% for D = 1.00 cm (minimum possible D) and decreases by 31% for D = 1.85 cm (maximum possible D).

(iv) Rotating by 90° about the beam direction (optic axis), as a check on possible effects due to polarization (see, for example, Hugtenburg *et al.*, 2010; Bartzsch *et al.*, 2014; Cornelius *et al.*, 2014); measured IC current changed by up to 9% in certain cases, *e.g.* depending on beam size and quality.

(v) Investigating the dependence of the measured IC current on the entrance position of the beam (the entrance aperture is approximately 100 mm wide and 10 mm high, for the normal disposition of the IC); for X-ray beams with dimensions of a few mm, the horizontal position is not critical, but variations of order 10% were observed when the vertical position is 'off-axis'.

(vi) The absolute values of measured ('background') IC currents, in the absence of X-rays, had a maximum of 1 pA.

Table 7
Experimental and calculated ADC IC currents for a variety of circular aperture sizes and both low and high ring currents.

The calculated value of $K_{e,eff}$ was 1.27 in all eight cases. See text for further details.

Aperture diameter (μm)	Nominal ring current (mA)	ADC IC current (expt) (A)	ADC IC current (calc) (A)	Ratio (expt/calc)	K_s (calc)
400	4.69	2.40×10^{-10}	2.18×10^{-10}	1.10	1.00
1000	4.70	1.18×10^{-9}	1.36×10^{-9}	0.868	1.00
2000	4.70	4.01×10^{-9}	5.44×10^{-9}	0.737	1.00
200	179.53	1.94×10^{-9}	2.10×10^{-9}	0.924	1.00
400	184.49	8.64×10^{-9}	8.62×10^{-9}	1.00	1.00
1000	182.85	4.49×10^{-8}	5.31×10^{-8}	0.846	1.00
2000	181.39	1.52×10^{-7}	2.08×10^{-7}	0.731	1.01
5000	172.10	8.69×10^{-7}	1.14×10^{-6}	0.762	1.08

Table 7 shows ADC IC current measurements and theoretical values for a range of circular apertures. Extra shielding was employed in the vicinity of the aperture stage and ADC IC in order to protect against extraneous scattering. The *in vacuo* filtration used in this case consisted of the F2 filter set (see Fig. 4) plus $\sqrt{2}$ mm Cu (we will refer to this combination as the F3 *in vacuo* filter set), with all other details unchanged from those above. The apertures used included the 5 mm-diameter one as detailed above, plus other apertures supplied by Amptek™, which are all 2 mm-thick HD17 W alloy (90 wt% W, 6 wt% Ni and 4 wt% Cu; ρ = 17 g cm^{-3}). The transmission, on the optic axis, through 2 mm of HD17 for this X-ray beam, is calculated to be ∼0.1%[40], which is acceptable. There is essentially no roll-off in the horizontal direction for such small apertures; however, in the vertical direction, calculations predict ∼7% decrease of signal at the extreme positions for the 5 mm aperture, whereas the decrease is ∼1% for the 2 mm aperture and ∼0.3% for the 1 mm aperture.[41] We will therefore not explicitly make allowance for beam non-uniformity in this case. The calculations do make allowance for the small magnification effect from the aperture to the ADC IC, and also for the offset current as determined above. The agreement between theory and experiment is reasonable, with the average value of the ratio, provided in the fifth column, being 0.87 (0.13). The paucity of data makes it difficult to speculate on any trends present; however, there is a suggestion that the agreement is better for the smaller apertures. It is also interesting to note that the ratio values obtained at low ring currents are seemingly well reproduced at high ring currents, for each of the three apertures concerned.

As a further investigation of recombination effects, Fig. 16 shows normalized ADC IC current values (both experiment and theory) as a function of operating voltage for five different *in vacuo* filter sets (F1 to F5) described previously. The 5 mm-diameter circular aperture was used and other experimental conditions were unchanged. The synchrotron was operated in top-up mode and all measurements were made with a nominal ring current of 200.3 mA. The measured current values cover a range of well over two orders of magnitude and represent an excellent test of our theoretical model. The beam quality changes quite dramatically, with the weighted-average X-ray energy having values of 47.4, 52.5, 82.6, 95.1 and 125 keV for filter sets F1 to F5, respectively. The respective calculated values of $K_{e,eff}$ were 1.23, 1.30, 1.26, 1.23 and 1.28, the trend reflecting the distribution of K_e with E. Whilst there remain some discrepancies between theory and experiment, the overall agreement is quite impressive, especially when one considers the wide range of experimental conditions being explored. It should be emphasized that the application of the theoretical model does not involve any element of fitting, with predicted IC currents being absolute. The minimum value of K_s was 1.01 (for filter set F5 and V = 2.00 kV) and the

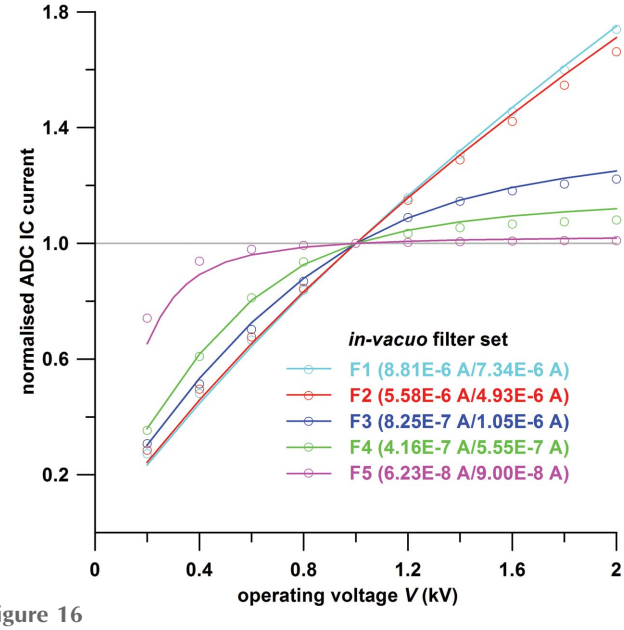

Figure 16
Plot of experimental ADC IC current values as a function of operating voltage V for various *in vacuo* filter sets (F1 to F5; described previously). The lines are corresponding full calculations, including K_e and K_s. For reasons of clarity, each data set has been normalized by the ADC IC current value at 1.00 kV, this value being given in the legend (the first value being for the experimental data and the second for the calculated data). The grey horizontal line represents the idealized case of zero recombination. See text for further details.

[40] Actually 0.066, 0.10 or 0.14% depending on whether it is based on integrated flux, ADC IC current or surface absorbed-dose rate to air, respectively.

[41] Another way of expressing this point is to note that the calculated value of the weighted-average X-ray energy is 82.8 keV for the 0.2 mm aperture and this value decreases by 0, 5, 21 and 133 eV for the 0.4, 1, 2 and 5 mm apertures, respectively [in accordance with the slight softening of the beam at the (vertical) extreme positions for the larger apertures].

maximum value was 18.1 (for filter set F1 and V = 0.20 kV), well beyond the range of applicability of more conventional theoretical models; see, for example, §4.4.1 and the discussion of (11), with $f > 0.7 \Rightarrow K_s < 1.4$.

In Fig. 17 we present a similar data set but, rather than varying beam quality (*via in vacuo* filtration), the ring current was varied (from 0.5 to 200 mA). In this case the measured ADC IC current values were normalized by the ring current, making these data 'absolute' and providing an even more stringent test of the model. The ring energy was 3.033 GeV; SCMPW operated at 3.00 T; F1, plus $\sqrt{2}$ mm Al, *in vacuo* filter set; fixed filters consisted of 73 mm He path, 0.35 mm Be window, 38 µm Al foil and 2.9 m air path (there was no *in vacuo* diamond); P = 101130 (50) Pa and T = 24.2 (0.1)°C. The offset current, of significance for the lowest ring currents, was estimated from a recent shutdown period to be 20 µA. The ADC IC (V = 2.00 kV) was located at 23.4 m from the X-ray source and intercepted a beam of size of 1.84 mm (H) × 1.30 mm (V). The effects of recombination are quite obvious, particularly at the highest ring currents; where the shape of the curve shows much less evidence of approaching a plateau at the largest IC operating voltages, and the measured (normalized) IC-current values are greatly reduced.

Calculated values (*spec.exe*) are also provided in Fig. 17 using step sizes of 10 µm across the beam cross-section and 0.1 keV (for 1 to 1000 keV). The value of $K_{e,eff}$ obtained was 1.27 throughout, and K_s varied from 1.02 [for 0.5 mA and V = 2.00 kV (1.00 for 0.001 mA)] to 31.8 [for 200 mA and V = 0.20 kV (*cf.* 3.87 for V = 2.00 kV)]. A further indication of the severity of the recombination effects is that, even for V = 2.00 kV, K_s < 1.4 (see above) is not satisfied until the ring current is below 10 mA. When the recombination effects are large (as at small values of V; and especially when the ring current is also large), we have (as pointed out above) $K_s \propto \xi$, and the ADC IC current should be directly proportional to V. On the other hand, if the recombination effects are negligible (as at suitably large values of V; and especially when the concomitant ring current is small), the ADC IC current should be independent of (*i.e.* constant with) V. The latter condition is synonymous with the plateau region in which we normally strive to operate. The shape of the experimental and calculated curves in Fig. 17 (and, in fact, Fig. 16) represent, in general, some portion of a smooth transition from one functional dependence to the other. Further detailed discussion of the results shown in Fig. 17 will be provided in the following section (§5).

Finally, as mentioned previously (see §3.3), a common means of quantifying kilovoltage X-ray beam quality is *via* HVL values. Fig. 18, by way of demonstration, shows experimental and theoretical data from which such HVL values could be derived. The experimental conditions are essentially the same as those above for Fig. 16. The synchrotron was in top-up mode, with ring currents between 200.0 and 200.6 mA; ADC IC currents were recorded (V = 2.00 kV) and scaled to a ring-current value of 200.3 mA. *The results presented in Fig. 18 do not involve any parameters with undetermined values and so no fitting is involved*, although the fact that we use ratios of ADC IC currents in this particular case does, in certain respects, lessen the stringency of the test. The agreement between theory and experiment for this case of *ex vacuo* Cu

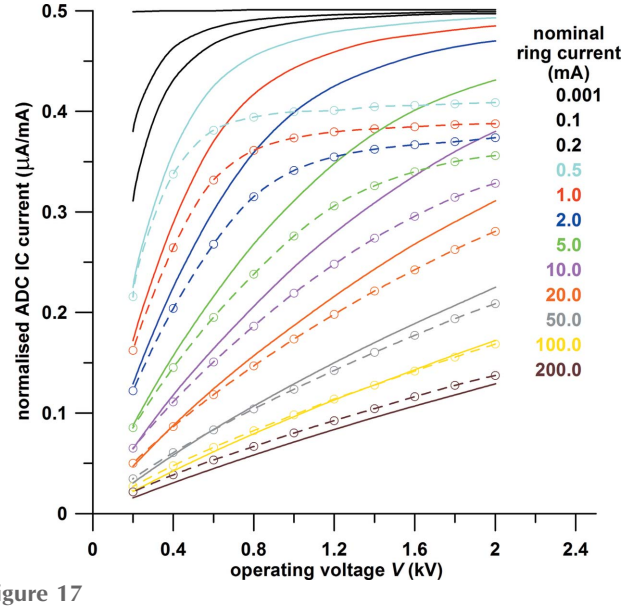

Figure 17
Plot of experimental ADC IC current values, normalized by the actual ring current, as a function of operating voltage V for various nominal ring currents (values as shown); the dashed lines are obtained by spline smoothing. The solid lines are corresponding full calculations, normalized by the nominal ring current, including K_e and K_s. The three black solid lines (nominal ring currents of 0.001, 0.1 and 0.2 mA) are included for completeness, but do not have associated experimental data. See text for further details.

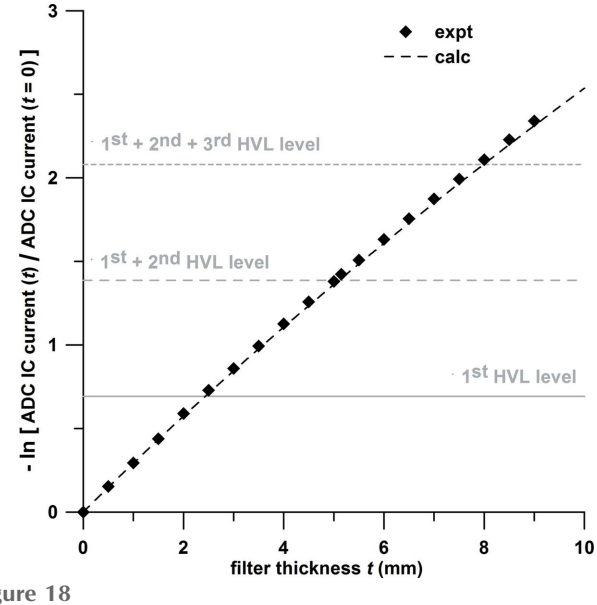

Figure 18
Graph showing experimental and theoretical values of the effective (*i.e.* polychromatic) 'μt' from the Beer–Lambert law (Bouguer, 1729; Lambert, 1760; Beer, 1852), in terms of ADC IC current, as a function of *ex vacuo* filter (Cu) thickness t. These Cu filters were from a Gammex 116 HVL attenuator set, and the *in vacuo* filter set F5 was used. The grey horizontal lines show the levels from which the first, second and third HVLs can be derived, *i.e.* ordinate values of −ln[1/2], −ln[1/4] and −ln[1/8]. See text for further details.

Table 8
Experimental and calculated HVL data for Cu, in terms of IC current, integrated flux and absorbed dose to air, corresponding to Fig. 18.

The first two rows are directly comparable. See text for further details.

	(First) HVL (mm)	Second HVL (mm)	HF	Third HVL (mm)
Experimental (IC current)	2.40 (0.01)	2.62 (0.01)	0.913 (0.007)	2.86 (0.01)
Calculated (IC current)	2.44	2.66	0.915	2.88
Calculated (integrated flux)	2.31	2.54	0.906	2.77
Calculated (absorbed dose)	2.51	2.76	0.907	3.01

filters (and *in vacuo* filter set F5) is excellent. As mentioned in §3.3, HVLs are more appropriately specified in terms of integrated flux or perhaps absorbed dose. Using IC currents for this purpose introduces an undesirable dependence on the exact technical specifications of the IC itself and its operation. In Table 8, therefore, the experimental and theoretical HVL values from Fig. 18 are supplemented by theoretical values based on integrated flux and absorbed dose. The values of first HVL and HF in Table 8 are slightly larger than the corresponding values provided in Table 5. The reason for this is that the Table 5 data pertained to hutch 1B whereas Table 8 relates to hutch 3B. Other sources of filtration (especially 2.7 mm *versus* 0.35 mm of Be in windows and the addition of the new FE 0.6 mm diamond filter) for the latter case, will result in a slightly harder X-ray beam and therefore increased first HVL. This will also serve to slightly narrow the flux distribution (*i.e.* make it slightly less polychromatic) and therefore result in a small increase of HF. Another factor which will contribute to these trends, in the same manner, is that the X-ray beam for Table 5 data was square with a 1 mm × 1 mm cross section at a distance of 22.3 m from the source, whereas for Table 8 data the cross section was circular and of 5 mm diameter at 137.6 m. The latter subtends a somewhat smaller solid angle (1.04 *versus* 2.01 nsr), resulting in reduced roll-off effects and therefore a harder X-ray beam on average.

5. Discussion and conclusions

In §4.2, several direct comparisons of calculated and measured absorbed-dose rates, on an absolute scale, revealed that, whilst our model is an extremely versatile, flexible and powerful tool, the theoretical predictions tended to be 20 to 30% larger than the experimental values. It is a testament to the difficulties associated with such absolute comparisons that we were only able to find one other study where a similar comparison was documented, that of Tanaka *et al.* (2000). As we pointed out in §4.2, these authors found a discrepancy of similar magnitude and sense, between theory and experiment. It may then appear that our expectations are confounded by the IC-current results shown in Fig. 15, inasmuch as the full-calculation curve (including both K_e and K_s) is actually lower than the experimental results. However, this can be understood when one appreciates that the calculated curve obtained with K_e alone is indeed higher than the linear fit to the lowest ring-current values, these both corresponding to saturation-current (recombination-free) values (see also the results presented in Table 7, where the recombination effects are generally insignificant). This in turn means that, whilst the formalism developed in §4.4.1 for calculating K_s is quite rigorous, the values of K_s obtained do tend to overestimate the ion-recombination effects, particularly when they are severe. This overestimation is exacerbated by the fact that the calculated value of the required input parameter q [see (7)] would be overestimated; hence both ξ and K_s would be (further) overestimated. In this way the overestimation of dose rates in §4.2 *and* the trends seen in Fig. 15 are both understandable and consistent.

Further evidence of this understanding is provided by the extensive absolute results presented in Fig. 17. We can see that the shapes of the curves associated with calculated and experimental results are generally in reasonable accord. It is quite apparent from the low ring-current data that the calculations have again overestimated the IC currents by ∼25%. For example, focusing on the results for V = 2.00 kV, the discrepancies are 20.6, 25.1, 25.8 and 21.1% for nominal ring currents of 0.5, 1, 2 and 5 mA, respectively. The associated curves are characterized by the fact that some semblance of a plateau (see §4.4) can be seen, or at least anticipated at larger values of V. However, as the nominal ring current increases further, the ion-recombination effects are overwhelming, with predicted K_s-values (at V = 2.00 kV) of 1.32, 1.61, 2.23, 2.92 and 3.87 for nominal ring currents of 10, 20, 50, 100 and 200 mA, respectively. In these cases, extremely large values of V, or more precisely E_{fs}, would be required to achieve any form of plateau region. Nariyama (2004), for example, reports on a miniature FAC developed for use with a SPring-8 undulator beam. The minimum plate separation of D = 4.2 mm and maximum operating voltage (magnitude) of V = 5 kV yields E_{fs} = 12 kV cm^{-1}, comparable with the electric field strength at which gas-amplification effects are generally expected to start becoming significant, *i.e.* the FAC would start to behave more as a proportional counter than an ionization chamber (see §4.4.1). Knoll (2000) states that for the secondary ionization associated with gas amplification: '*In typical gases, at atmospheric pressure, the threshold field is of the order of 10^6 V m^{-1}.*', *i.e.* 10 kV cm^{-1} [42].

Thus as the nominal ring current increases toward 200 mA in Fig. 17, the overestimation of the calculated (saturation) IC current begins being compensated for by the overestimation of the calculated K_s-value. At 100 mA the two effects almost cancel and so the corresponding curves in Fig. 17 show excellent, but fortuitous, agreement. Finally, at 200 mA, the calculated curve becomes lower than the experimental curve, as was the case in Fig. 15.

[42] This number is essentially the field strength at which the first Townsend ionization coefficient (Townsend, 1903, 1910) can be considered to be insignificant. A value of 10^6 V m^{-1} (≡ 13 V cm^{-1} Torr^{-1} at atmospheric pressure) is quite consistent with the data presented in Fig. 1 of Stout & Dawson (1978).

In this paper we have provided ample demonstration of the benefits of having a comprehensive model for quantitative characterization of the X-ray beam employed at a beamline such as the Australian Synchrotron's IMBL. We have discussed the limitations and deficiencies of such a model, implemented and embodied here in the computer program *spec.exe*. The model can be used both for furthering our understanding of existing experimental results and in a predictive capacity, such as is required when designing certain experiments. We have focused on certain key attributes or properties of the X-ray beam of significance for the conduct of state-of-the-art imaging, tomography and radiotherapy studies at IMBL. These include flux (and flux density, integrated flux, and so on), beam quality, power and dose (or dose rate). Emphasis has also been placed on important and practical measured quantities such as IC current. This necessarily requires detailed consideration of inherent limitations of such devices, when used with high-flux kilovoltage X-ray beams such as those produced at IMBL, *e.g.* electron-loss and ion-recombination effects.

Acknowledgements

We acknowledge the many staff members at the Australian Synchrotron who have contributed to the design, construction, commissioning and continuing development of IMBL as a world-class research facility. In particular we thank: our IMBL colleagues Robert Acres, Iwan Cornelius, Anton Maksimenko and James Pearson for helpful discussions and support; Engineering staff including Luke Adamson, Bryce Karnaghan, Paul Martin, Jonathan McKinlay and Adam Walsh for a range of innovative solutions to IMBL challenges; Accelerator Operators Mark Atkinson, Madeleine Chalmers, Robbie Clarken, Simon Cunningham, Jonathan de Booy, Louise Hearder, Peter Jones, Rodney King, Mike Lafky, Keara Marshall, Stephen Martin, Don McGilvery, Nicholas Rae, Cameron Rodda and Joel Trewhella for providing countless hours of reliable synchrotron operation, including many special commissioning shifts and unusual beam requests; Accelerator Scientists Mark Boland, Rohan Dowd, Greg LeBlanc, Eugene Tan, Kent Wootton for many stimulating and informative exchanges; Mechanical Technicians, especially Trent Smith, for all their skill and expertise. We thank Peter Lynch (Deakin University), Helen Brand and Justin Kimpton (both Australian Synchrotron) for their invaluable assistance with characterization of the graphite-filter materials. The expert advice provided by Pekka Suortti (University of Helsinki) in connection with aspects of the bent-crystal calculations, and Takashi Tanaka (SPring-8) regarding results from *SPECTRA*, is gratefully acknowledged. We acknowledge the generous financial support of NHMRC to key aspects of IMBL, including infrastructure and staff (such as AWS) salaries. Finally, we thank Rob Lewis (Monash University/University of Saskatchewan) and the late Steve Wilkins (CSIRO/Monash University) for their vision and special contributions to the early development of IMBL.

References

Adamovics, J. & Maryanski, M. J. (2006). *Radiat. Prot. Dosim.* **120**, 107–112.
Aglincev, K. K. (1957). *Dosimetry of Ionising Radiation.* Moscow: Gotsheizdat. (In Russian.)
Almond, P. R. (1981). *Med. Phys.* **8**, 901–904.
Andersson, J. (2013). Thesis, Umeå Universitet, Sweden.
Andersson, J., Kaiser, F.-J., Gómez, F., Jäkel, O., Pardo-Montero, J. & Tölli, H. (2012). *Phys. Med. Biol.* **57**, 7161–7175.
Andrews, C. L. (1938). *Phys. Rev.* **54**, 994–999.
Armstrong, W. & Tate, P. A. (1965). *Phys. Med. Biol.* **10**, 229–241.
Asaoka, S., Maezawa, H., Kamiya, Y. & Yanagihara, M. (1992). *Rev. Sci. Instrum.* **63**, 473–476.
Attix, F. H. (1986). *Introduction to Radiological Physics and Radiation Dosimetry.* New York: Wiley.
Attix, F. H. & DeLaVergne, L. (1954). *J. Res. Natl Bur. Stan.* **53**, 393–402.
Bartzsch, S., Lerch, M., Petasecca, M., Bräuer-Krisch, E. & Oelfke, U. (2014). *Med. Phys.* **41**, 041703.
Beer, A. (1852). *Ann. Phys. Chem.* **162**, 78–88.
Bencokova, Z., Balosso, J. & Foray, N. (2008). *J. Synchrotron Rad.* **15**, 74–85.
Berger, R. T. (1961). *Radiat. Res.* **15**, 1–29.
Biscoe, J. & Warren, B. E. (1942). *J. Appl. Phys.* **13**, 364–371.
Boag, J. W. (1969). *Int. J. Radiat. Phys. Chem.* **1**, 267–285.
Boag, J. W. (1987). *Ionization chambers* in *The Dosimetry of Ionizing Radiation*, Vol. II, edited by K. R. Kase, B. E. Bjärngard and F. H. Attix. New York: Academic.
Boag, J. W. & Wilson, T. (1952). *Br. J. Appl. Phys.* **3**, 222–229.
Böhm, J. (1976). *Phys. Med. Biol.* **21**, 754–759.
Boldeman, J. W. & Einfeld, D. (2004). *Nucl. Instrum. Methods Phys. Res. A*, **521**, 306–317.
Bouchet, A., Bräuer-Krisch, E., Prezado, Y., El Atifi, M., Rogalev, L., Le Clec'h, C., Laissue, J. A., Pelletier, L. & Le Duc, G. (2016). *Int. J. Radiat. Oncol. Biol. Phys.* **95**, 1485–1494.
Bouguer, P. (1729). *Essai d'Optique sur la Gradation de la Lumière.* Paris: Claude Jombert.
Boutillon, M. (1998). *Phys. Med. Biol.* **43**, 2061–2072.
Bradbury, N. E. (1932). *Phys. Rev.* **40**, 508–523.
Bradbury, N. E. (1940). *J. Appl. Phys.* **11**, 267–273.
Bräuer-Krisch, E., Adam, J.-F., Alagoz, E., Bartzsch, S., Crosbie, J., DeWagter, C., Dipuglia, A., Donzelli, M., Doran, S., Fournier, P., Kalef-Ezra, J., Kock, A., Lerch, M., McErlean, C., Oelfke, U., Olko, P., Petasecca, M., Povoli, M., Rosenfeld, A., Siegbahn, E. A., Sporea, D. & Stugu, B. (2015). *Phys. Med.* **31**, 568–583.
Bruggmoser, G., Saum, R., Schmachtenberg, A., Schmid, F. & Schüle, E. (2007). *Phys. Med. Biol.* **52**, N35–N50.
Buhr, H., Büermann, L., Gerlach, M., Krumrey, M. & Rabus, H. (2012). *Phys. Med. Biol.* **57**, 8231–8247.
Burns, D. T. & Büermann, L. (2009). *Metrologia*, **46**, S9–S23.
Burns, J. E. & Burns, D. T. (1993). *Phys. Med. Biol.* **38**, 1986–1988.
Burns, J. E. & Rosser, K. E. (1990). *Phys. Med. Biol.* **35**, 687–693.
Butler, D. J., Stevenson, A. W., Wright, T. E., Harty, P. D., Lehmann, J., Livingstone, J. & Crosbie, J. C. (2015). *Phys. Med. Biol.* **60**, 8625–8641.
Cember, H. (1983). *Introduction to Health Physics*, 2nd ed. New York: Pergamon Press.
Chantler, C. T., Olsen, K., Dragoset, R. A., Chang, J., Kishore, A. R., Kotochigova, S. A. & Zucker, D. S. (2005). *X-ray Form Factor, Attenuation and Scattering Tables.* Version 2.1. National Institute of Standards and Technology, Bethesda, MD, USA.
Chasman, R., Green, G. K. & Rowe, E. M. (1975). *IEEE Trans. Nucl. Sci.* **22**, 1765–1767.
Chipman, D. R. (1955). *J. Appl. Phys.* **26**, 1387.
Compton, A. H. & Allison, S. K. (1955). *X-rays in Theory and Experiment.* New York: Van Nostrand.

Cornelius, I., Guatelli, S., Fournier, P., Crosbie, J. C., Sanchez del Rio, M., Bräuer-Krisch, E., Rosenfeld, A. & Lerch, M. (2014). *J. Synchrotron Rad.* **21**, 518–528.

Crosbie, J. C., Fournier, P., Bartzsch, S., Donzelli, M., Cornelius, I., Stevenson, A. W., Requardt, H. & Bräuer-Krisch, E. (2015). *J. Synchrotron Rad.* **22**, 1035–1041.

Crosbie, J. C., Rogers, P. A. W., Stevenson, A. W., Hall, C. J., Lye, J. E., Nordström, T., Midgley, S. M. & Lewis, R. A. (2013). *Med. Phys.* **40**, 062103.

Crosbie, J. C., Svalbe, I., Midgley, S. M., Yagi, N., Rogers, P. A. W. & Lewis, R. A. (2008). *Phys. Med. Biol.* **53**, 6861–6877.

Cunningham, I. A. (1998). *Proc. SPIE*, **3336**, 220–230.

DeMarco, J. J. & Suortti, P. (1971). *Phys. Rev. B*, **4**, 1028–1033.

Donzelli, M., Bräuer-Krisch, E., Nemoz, C., Brochard, T. & Oelfke, U. (2016). *Med. Phys.* **43**, 3157–3167.

Dowd, R., LeBlanc, G. & Zingre, K. (2008). *Nucl. Instrum. Methods Phys. Res. A*, **592**, 224–229.

Doyle, P. A. & Turner, P. S. (1968). *Acta Cryst.* A**24**, 390–397.

Dutreix, J., Dutreix, A. & Tubiana, M. (1965). *Phys. Med. Biol.* **10**, 177–190.

Erola, E., Eteläniemi, V., Suortti, P., Pattison, P. & Thomlinson, W. (1990). *J. Appl. Cryst.* **23**, 35–42.

Failla, G. (1929). *Am. J. Roent.* **21**, 47–63.

Farmer, F. T. (1955). *Br. J. Radiol.* **28**, 304–306.

Fournier, P., Crosbie, J. C., Cornelius, I., Berkvens, P., Donzelli, M., Clavel, A. H., Rosenfeld, A. B., Petasecca, M., Lerch, M. L. F. & Bräuer-Krisch, E. (2016). *Phys. Med. Biol.* **61**, N349–N361.

Gagliardi, F. M., Cornelius, I., Blencowe, A., Franich, R. D. & Geso, M. (2015). *Med. Phys.* **42**, 6973–6986.

Garderen, E. D. van, Bambery, K. R., Clift, M., LeBlanc, G. S., Martin, D. E., Puskar, L., Starritt, A., Tobin, M. J., Wang, D. & Zhu, D. (2013). *J. Phys. Conf. Ser.* **425**, 042015.

Gorjiara, T., Hill, R., Kuncic, Z., Bosi, S., Davies, J. B. & Baldock, C. (2011). *Phys. Med. Biol.* **56**, 4685–4699.

Greening, J. R. (1964). *Phys. Med. Biol.* **9**, 143–154.

Greening, J. R. (1965). *Phys. Med. Biol.* **10**, 566.

Greening, J. R. (1985). *Fundamentals of Radiation Dosimetry*, 2nd ed. New York: Taylor and Francis.

Grimbergen, T. W. M., van Dijk, E. & de Vries, W. (1998). *Phys. Med. Biol.* **43**, 3207–3224.

Grosswendt, B. (1990). *Phys. Med. Biol.* **35**, 1233–1245.

Hall, C., Hausermann, D., Maksimenko, A., Astolfo, A., Siu, K., Pearson, J. & Stevenson, A. (2013). *J. Instrum.* **8**, C06011.

Hall, J. J. (1967). *Phys. Rev.* **161**, 756–761.

Harper, W. R. (1933). *Math. Proc. Camb. Philos. Soc.* **29**, 149–155.

Harty, P. D., Lye, J. E., Ramanathan, G., Butler, D. J., Hall, C. J., Stevenson, A. W. & Johnston, P. N. (2014). *Med. Phys.* **41**, 052101.

Hearmon, R. F. S. (1961). *An Introduction to Applied Anisotropic Elasticity*. London: Oxford University Press.

Hill, R. (1952). *Proc. Phys. Soc. A*, **65**, 349–354.

Hill, R., Healy, B., Holloway, L., Kuncic, Z., Thwaites, D. & Baldock, C. (2014). *Phys. Med. Biol.* **59**, R183–R231.

Hill, R., Holloway, L. & Baldock, C. (2005). *Phys. Med. Biol.* **50**, N331–N344.

Hill, R., Mo, Z., Haque, M. & Baldock, C. (2009). *Med. Phys.* **36**, 3971–3981.

Honkimäki, V. & Suortti, P. (1992). *J. Appl. Cryst.* **25**, 97–104.

Howells, M. R., Beetz, T., Chapman, H. N., Cui, C., Holton, J. M., Jacobsen, C. J., Kirz, J., Lima, E., Marchesini, S., Miao, H., Sayre, D., Shapiro, D. A., Spence, J. C. H. & Starodub, D. (2009). *J. Electron Spectrosc. Relat. Phenom.* **170**, 4–12.

Hubbell, J. H. (1999). *Phys. Med. Biol.* **44**, R1–R22.

Hubbell, J. H. (2006). *Phys. Med. Biol.* **51**, R245–R262.

Hubbell, J. H. & Seltzer, S. M. (1995). NIST Technical Report 5632. National Institute of Standards and Technology, Bethesda, MD, USA.

Hugtenburg, R. P., Adegunloye, A. S. & Bradley, D. A. (2010). *Nucl. Instrum. Methods Phys. Res. A*, **619**, 221–224.

IAEA (2000). IAEA Technical Report Series No. 398. International Atomic Energy Agency, Vienna, Austria.

IAEA (2007). IAEA Technical Report Series No. 457. International Atomic Energy Agency, Vienna, Austria.

Ibahim, M. J., Crosbie, J. C., Yang, Y., Zaitseva, M., Stevenson, A. W., Rogers, P. A. W. & Paiva, P. (2014). *PLoS One*, **9**, e100547.

ICRU (1976). ICRU Report No. 24. International Commission on Radiation Units and Measurements, Bethesda, MD, USA.

ICRU (1980). ICRU Report No. 33. International Commission on Radiation Units and Measurements, Bethesda, MD, USA.

ICRU (1989). ICRU Report No. 44. International Commission on Radiation Units and Measurements, Bethesda, MD, USA.

Internationale Tabellen zur Bestimmung von Kristallstrukturen (1935). Vol. II. Berlin: Borntrager.

International Tables for X-ray Crystallography (1962). Vol. III. Birmingham: Kynoch Press.

Jaffé, G. (1913). *Ann. Phys.* **347**, 303–344.

Jaffé, G. (1940). *Phys. Rev.* **58**, 968–976.

Kara-Michailova, E. & Lea, D. E. (1940). *Math. Proc. Camb. Philos. Soc.* **36**, 101–126.

Katoh, K. & Greening, J. R. (1965). *Phys. Med. Biol.* **10**, 565–566.

Kemp, L. A. W. & Hall, S. M. (1954). *Br. J. Radiol.* **27**, 219–227.

Kim, K.-J. (1989). *AIP Conf. Proc.* **184**, 565–632.

Kim, K.-J. (2001). *Characteristics of Synchrotron Radiation* in *X-ray Data Booklet.* 2nd ed., Section 2.1, compiled and edited by A. C. Thompson and D. Vaughan. Lawrence Berkeley National Laboratory, Berkeley, CA, USA.

Klevenhagen, S. C., Aukett, R. J., Harrison, R. M., Moretti, C., Nahum, A. E. & Rosser, K. E. (1996). *Phys. Med. Biol.* **41**, 2605–2625.

Knoll, G. F. (2000). *Radiation Detection and Measurement*, 3rd ed. New York: Wiley.

Krauss, A., Büermann, L., Kramer, H.-M. & Selbach, H.-J. (2012). *Phys. Med. Biol.* **57**, 6245–6268.

Kron, T., Duggan, L., Smith, T., Rosenfeld, A., Butson, M., Kaplan, G., Howlett, S. & Hyodo, K. (1998). *Phys. Med. Biol.* **43**, 3235–3259.

Kurosawa, T. & Takata, N. (2005). *J. Nucl. Sci. Technol.* **42**, 1077–1080.

Lai, B., Khounsary, A. & Gluskin, E. (1993). Argonne National Laboratory/Advanced Photon Source Technical Bulletin. ANL/APS/TB-11. Argonne National Laboratory, Argonne, IL, USA.

Laissue, J. A., Blattmann, H., Di Michiel, M., Slatkin, D. N., Lyubimova, N., Guzman, R., Zimmermann, W., Birrer, S., Bley, T., Kircher, P., Stettler, R., Fatzer, R., Jaggy, A., Smilowitz, H., Brauer, E., Bravin, A., Le Duc, G., Nemoz, C., Renier, M., Thomlinson, W. C., Stepanek, J. & Wagner, H.-P. (2001). *Proc. SPIE*, **4508**, 65–73.

Laissue, J. A., Geiser, G., Spanne, P. O., Dilmanian, F. A., Gebbers, J.-O., Geiser, M., Wu, X.-Y., Makar, M. S., Micca, P. L., Nawrocky, M. M., Joel, D. D. & Slatkin, D. N. (1998). *Int. J. Cancer*, **78**, 654–660.

Lambert, J. H. (1760). *Photometria sive de Mensura et Gradibus Luminis, Colorum et Umbrae.* Germany: Augsburg.

Langevin, P. (1913). *Radium (Paris)*, **10**, 113–118.

La Russa, D. J., McEwen, M. & Rogers, D. W. O. (2007). *Med. Phys.* **34**, 4690–4699.

LeBlanc, G., Boland, M. & Tan, E. (2004). *ASP Storage Ring Beam Sizes at the Beamline Source Points.* Internal Report, 9 January, 2004. Australian Synchrotron, Clayton, Victoria, Australia.

Liebmann, M., Poppe, B. & von Boetticher, H. (2015). *J. Appl. Clin. Med. Phys.* **16**, 396–407.

Lin, U.-T. & Chu, C.-H. (2006). *Appl. Radiat. Isot.* **64**, 608–614.

Llopart, X., Campbell, M., Dinapoli, R., San Segundo, D. & Pernigotti, E. (2002). *IEEE Trans. Nucl. Sci.* **49**, 2279–2283.

Lobachevsky, P., Ivashkevich, A., Forrester, H. B., Stevenson, A. W., Hall, C. J., Sprung, C. N. & Martin, O. A. (2015). *Radiat. Res.* **184**, 650–659.

Lye, J. E., Butler, D. J. & Webb, D. V. (2010). *Metrologia*, **47**, 11–20.

Lye, J. E., Harty, P. D., Butler, D. J., Crosbie, J. C., Livingstone, J., Poole, C. M., Ramanathan, G., Wright, T. & Stevenson, A. W. (2016). *Phys. Med. Biol.* **61**, 4201–4222.

Ma, C.-M., Coffey, C. W., DeWerd, L. A., Liu, C., Nath, R., Seltzer, S. M. & Seuntjens, J. P. (2001). *Med. Phys.* **28**, 868–893.

Maezawa, H., Asaoka, S., Yanagihara, M. & Kamiya, Y. (1993). *Proc. SPIE*, **1739**, 254–265.

Martínez-Rovira, I., Sempau, J. & Prezado, Y. (2012). *Med. Phys.* **39**, 2829–2838.

Mason, E. A. & Vanderslice, J. T. (1959). *Phys. Rev.* **114**, 497–502.

Mathieson, A. McL. & Stevenson, A. W. (1985). *Acta Cryst.* A**41**, 290–296.

Maxwell, J. C. (1865). *Philos. Trans. R. Soc. London*, **155**, 459–512.

McGowan, S. (1965). *Phys. Med. Biol.* **10**, 25–40.

McMaster, W. H., Del Grande, N. K., Mallett, J. H. & Hubbell, J. H. (1970). LLNL Report No. UCRL-50174. Lawrence Livermore National Laboratory, Livermore, CA, USA.

Mie, G. (1904). *Ann. Phys.* **318**, 857–889.

Nariyama, N. (2004). *Rev. Sci. Instrum.* **75**, 2860–2862.

Nariyama, N. (2006). *Phys. Med. Biol.* **51**, 5199–5209.

Nariyama, N. (2007). *IEEE Nucl. Sci. Symp. Conf. Rec.* **1**, 574–578.

Nariyama, N., Kishi, N. & Ohnishi, S. (2004). *Nucl. Instrum. Methods Phys. Res. A*, **524**, 324–331.

Nariyama, N., Umetani, K., Shinohara, K., Kondoh, T., Kurihara, A. & Fukumoto, M. (2011). *Prog. Nucl. Sci. Tech.* **2**, 312–317.

National Bureau of Standards (1976). Monograph 25, Sect. 13, p. 35. National Bureau of Standards, Washington, DC, USA.

Novković, D., Tomašević, M. & Subotić, K. (1998). *Phys. Med. Biol.* **43**, 559–575.

Ohmasa, Y., Shimomura, S. & Chiba, A. (2016). *J. Appl. Cryst.* **49**, 835–844.

Onsager, L. (1938). *Phys. Rev.* **54**, 554–557.

Panopoulos, H. P., Wootton, K. P., Boland, M. J. & Rassool, R. P. (2011). *Proceedings of the Second International Particle Accelerator Conference (IPAC'11)*, San Sebastian, Spain, TUPC062, pp. 1138–1140.

Penning, P. & Polder, D. (1961). *Philips Res. Rep.* **16**, 419–440.

Petasecca, M., Cullen, A., Fuduli, I., Espinoza, A., Porumb, C., Stanton, C., Aldosari, A. H., Bräuer-Krisch, E., Requardt, H., Bravin, A., Perevertaylo, V., Rosenfeld, A. B. & Lerch, M. L. F. (2012). *J. Instrum.* **7**, P07022.

Podgorsak, E. B. (2005). Editor. *Radiation Oncology Physics: A Handbook for Teachers and Students.* Vienna: IAEA.

Polder, D. & Penning, P. (1964). *Acta Cryst.* **17**, 950–955.

Prager, P. R. (1971). PhD thesis, University of Melbourne, Australia.

Prezado, Y., Vautrin, M., Martínez-Rovira, I., Bravin, A., Estève, F., Elleaume, H., Berkvens, P. & Adam, J. F. (2011). *Med. Phys.* **38**, 1709–1717.

Renier, M., Brochard, T., Nemoz, C. & Thomlinson, W. (2002). *Nucl. Instrum. Methods Phys. Res. A*, **479**, 656–660.

Reuss, A. (1929). *Z. Angew. Math. Mech.* **9**, 49–58.

Ritz, V. H. & Attix, F. H. (1962). *Radiat. Res.* **16**, 401–415.

Roesch, W. C. (1958). *Radiat. Res.* **9**, 399–410.

Rogers, D. W. O., Faddegon, B. A., Ding, G. X., Ma, C.-M., We, J. & Mackie, T. R. (1995). *Med. Phys.* **22**, 503–524.

Roos, M. (1993). *The state of the art in plane-parallel chamber hardware with emphasis on the new Roos and Attix chambers.* (Unpublished; available from PTB-Braunschweig, Germany.)

Ryan, C. G., Kirkham, R., Hough, R. M., Moorhead, G., Siddons, D. P., de Jonge, M. D., Paterson, D. J., De Geronimo, G., Howard, D. L. & Cleverley, J. S. (2010). *Nucl. Instrum. Methods Phys. Res. A*, **619**, 37–43.

Sánchez del Río, M. & Dejus, R. J. (2011). *Proc. SPIE*, **8141**, 814115.

Sanchez del Rio, M., Perez-Bocanegra, N., Shi, X., Honkimäki, V. & Zhang, L. (2015). *J. Appl. Cryst.* **48**, 477–491.

Schreiner, L. J. (2004). *J. Phys. Conf. Ser.* **3**, 9–21.

Schulze, C. & Chapman, D. (1995). *Rev. Sci. Instrum.* **66**, 2220–2223.

Schulze, C., Lienert, U., Hanfland, M., Lorenzen, M. & Zontone, F. (1998). *J. Synchrotron Rad.* **5**, 77–81.

Scott, P. B. & Greening, J. R. (1961). *Br. J. Radiol.* **34**, 791–800.

Seemann, H. (1912). *Ann. Phys.* **343**, 781–829.

Seltzer, S. M. (1993). *Radiat. Res.* **136**, 147–170.

Siegbahn, E. A., Bräuer-Krisch, E., Bravin, A., Nettelbeck, H., Lerch, M. L. F. & Rosenfeld, A. B. (2009). *Med. Phys.* **36**, 1128–1137.

Siegbahn, E. A., Stepanek, J., Bräuer-Krisch, E. & Bravin, A. (2006). *Med. Phys.* **33**, 3248–3259.

Slatkin, D. N., Spanne, P., Dilmanian, F. A. & Sandborg, M. (1992). *Med. Phys.* **19**, 1395–1400.

Stevenson, A. W., Hall, C. J., Mayo, S. C., Häusermann, D., Maksimenko, A., Gureyev, T. E., Nesterets, Y. I., Wilkins, S. W. & Lewis, R. A. (2012). *J. Synchrotron Rad.* **19**, 728–750.

Stevenson, A. W., Mayo, S. C., Häusermann, D., Maksimenko, A., Garrett, R. F., Hall, C. J., Wilkins, S. W., Lewis, R. A. & Myers, D. E. (2010). *J. Synchrotron Rad.* **17**, 75–80.

Stout, R. R. & Dawson, G. A. (1978). *Pure and Applied Geophysics PAGEOPH*, **116**, 159–166.

Suortti, P., Fiedler, S., Bravin, A., Brochard, T., Mattenet, M., Renier, M., Spanne, P., Thomlinson, W., Charvet, A. M., Elleaume, H., Schulze-Briese, C. & Thompson, A. C. (2000). *J. Synchrotron Rad.* **7**, 340–347.

Suortti, P. & Schulze, C. (1995). *J. Synchrotron Rad.* **2**, 6–12.

Takagi, S. (1962). *Acta Cryst.* **15**, 1311–1312.

Takagi, S. (1969). *J. Phys. Soc. Jpn*, **26**, 1239–1253.

Tanaka, T. (2014). *Phys. Rev. ST Accel. Beams*, **17**, 060702.

Tanaka, T., Kato, M., Saito, N., Tono, K., Yabashi, M. & Ishikawa, T. (2015). *Rev. Sci. Instrum.* **86**, 093104.

Tanaka, T. & Kitamura, H. (2001). *J. Synchrotron Rad.* **8**, 1221–1228.

Tanaka, T. & Kitamura, H. (2004). *AIP Conf. Proc.* **705**, 41–44.

Tanaka, T. & Kitamura, H. (2007). *AIP Conf. Proc.* **879**, 355–358.

Tanaka, T., Oura, M., Ohashi, H., Goto, S., Suzuki, Y. & Kitamura, H. (2000). *J. Appl. Phys.* **88**, 2101–2107.

Taupin, D. (1964). *Bull. Soc. Fr. Minér. Crist.* **87**, 469–511.

Thomson, J. J. (1899). *Philos. Mag. Ser. 5*, **47**, 253–268.

Thomson, J. J. & Rutherford, E. (1896). *Philos. Mag. Ser. 5*, **42**, 392–407.

Thomson, J. J. & Thomson, G. P. (1928). *Conduction of Electricity through Gases*, Volume I, 3rd ed. London: Cambridge University Press.

Townsend, J. S. (1903). *Electrician*, **50**, 971.

Townsend, J. S. (1910). *The Theory of Ionization of Gases by Collision.* London: Constable.

Trinajstic, K., Boisvert, C., Long, J., Maksimenko, A. & Johanson, Z. (2015). *Biol. Rev. Camb Philos Soc.* **90**, 467–501.

Trout, E. D., Kelley, J. P. & Lucas, A. C. (1960). *Am. J. Roent.* **84**, 729–740.

Ubrich, F., Wulff, J., Kranzer, R. & Zink, K. (2008). *Phys. Med. Biol.* **53**, 4893–4906.

Voigt, W. (1928). *Lehrbuch der Kristallphysik (mit Ausschluss der Kristalloptik)*. 2nd ed. Leipzig: B. G. Teubner.

Warren, B. E. (1949). *J. Appl. Phys.* **20**, 96–97.

Wigner, E. (1932). *Phys. Rev.* **40**, 749–759.

Wootton, K. P., Boland, M. J., Corbett, W. J., Huang, X., LeBlanc, G. S., Lundin, M., Panopoulos, H. P., Safranek, J. A., Tan, Y.-R. E., Taylor, G. N., Tian, K. & Rassool, R. P. (2013). *Phys. Rev. ST Accel. Beams*, **16**, 074001.

Wortman, J. J. & Evans, R. A. (1965). *J. Appl. Phys.* **36**, 153–156.

Yang, Y., Crosbie, J. C., Paiva, P., Ibahim, M., Stevenson, A. & Rogers, P. A. W. (2014). *Radiat. Res.* **182**, 626–639.

Zeinali-Rafsanjani, B., Mosleh-Shirazi, M. A., Faghihi, R., Karbasi, S. & Mosalaei, A. (2015). *J. Med. Phys.* **40**, 74–79.

Zeman, W., Curtis, H. J. & Baker, C. P. (1961). *Radiat. Res.* **15**, 496–514.

Zhang, L., Barrett, R., Cloetens, P., Detlefs, C. & Sanchez del Rio, M. (2014). *J. Synchrotron Rad.* **21**, 507–517.

Zschornack, G. (2007). *Handbook of X-ray Data.* Berlin: Springer.